Aberration Correction in Digital Holography

by

Abbie E. Tippie

Submitted in Partial Fulfillment

of the

Requirements for the Degree

Doctor of Philosophy

Supervised by

Professor James R. Fienup

The Institute of Optics
Arts, Sciences and Engineering
Edmund A. Hajim School of Engineering and Applied Sciences

University of Rochester
Rochester, New York

2012

Curriculum Vitae

The author was born in McAllen, TX on January 10, 1984. She attended Colorado State University from 2002 to 2006 and graduated with honors with a Bachelor of Science degree in Electrical Engineering with an Optoelectronics concentration and a minor in Physics. Abbie entered the Institute of Optics at the University of Rochester in the Fall of 2006. She pursued research in digital holography under the direction of Professor James R. Fienup. She received the Master of Science degree in Optics from the University of Rochester in 2010. Abbie was recipient of the Monfort Scholarship from 2002-2006. Abbie was awarded a National Science Foundation Graduate Research Fellowship from 2006-2009 and a Harvey Fellowship from 2010-2012.

Curriculum Vitae

Peer-Reviewed Journal Publications

1. A. E. Tippie, A. Kumar, and J. R. Fienup, "High-resolution Synthetic-Aperture Digital Holography with Digital Phase and Pupil Correction," Opt. Express **19**, 12027-12038 (2011).
2. A. E. Tippie and J. R. Fienup, "Multiple-Plane Anisoplanatic Phase Correction in a Laboratory Digital Holography Experiment," Opt. Lett. **35**, 3291-3293 (2010).
3. A. E. Tippie and J. R. Fienup, "Phase-error Correction for Multiple Planes using a Sharpness Metric," Opt Lett. **34**, 701-703 (2009).

Published Conference Proceedings

1. A. E. Tippie and J. R. Fienup, "Weak-Object Image Reconstructions with Single-Shot Digital Holography," in *Digital Holography and Three-Dimensional Imaging,* OSA Technical Digest (CD) (Optical Society of America, 2012), paper DMC5.
2. A. E. Tippie and J. R. Fienup, "Region-of-Interest Sharpness Correction," in *Frontiers in Optics,* OSA Technical Digest (CD) (Optical Society of America, 2011), paper FTuF2.

3. J. R. Fienup and A. E. Tippie, "Gigapixel Synthetic-Aperture Digital Holography," Proc. SPIE **8122**, Tribute to Joseph W. Goodman (San Diego, CA, August 2011).

4. A. E. Tippie and J. R. Fienup, "Gigapixel Synthetic-Aperture Digital Holography: Sampling and Resolution Considerations," in *Computational Optical Sensing and Imaging,* OSA Technical Digest (CD) (Optical Society of America, 2011), paper CWB1.

5. A. E. Tippie and J. R. Fienup, "Sub-Aperture Techniques Applied to Phase-Error Correction in Digital Holography," in *Digital Holography and Three-Dimensional Imaging*, OSA Technical Digest (CD) (Optical Society of America, 2011), paper DMA4.

6. A. E. Tippie, S. A. Shroff, and J. R. Fienup, "Improved Aperture Synthesis for Digital Holography," in *Frontiers in Optics*, OSA Technical Digest (CD) (Optical Society of America, 2010), paper FThK2.

7. A. E. Tippie and J. R. Fienup, "Laboratory Demonstration of Sharpness Metric Approach to Correct Multiple-Plane Phase Errors," in *Signal Recovery and Synthesis*, OSA Technical Digest (CD), Optical Society of America (2009), paper STuC6.

8. A. E. Tippie and J. R. Fienup, "Digital Holography with Multiple-Plane Phase Error Correction," in *Advances in Imaging*, OSA Technical Digest (CD), Optical Society of America (2009), paper JTuA5.

9. A. E. Tippie and J. R. Fienup, “Phase Error Correction for Multiple Planes using Sharpness Metrics,” Proc. SPIE **7094**, Unconventional Imaging IV (San Diego, CA, August 2008) pp. 709404-1-6.

Acknowledgements

The journey of a doctoral dissertation is not accomplished without the unwaveringly support of many individuals along the way. I am eternally grateful to those who have come alongside me in this endeavor.

First and foremost, I want to gratefully acknowledge the impact and support I have received from Professor James R. Fienup. Early in my undergraduate career as a National Science Foundation Research Experience for Undergraduate (REU) student, Professor Fienup helped me discover the excitement and boundless opportunities in the world of research. I am extremely appreciative for the high standards that were set in this research group in terms of research expectations, quality of work and professionalism. I am thankful for the significant group and personal time invested to encourage myself and my fellow students to become better technical writers and presenters. I am grateful for an advisor who involved us in the entire research process, willingly allowing us to provide feedback and brainstorming ideas for research proposals. Professor Fienup always set a positive example in his involvement in professional societies, and I am very appreciative for his encouragement to attend conferences, volunteer, interact and collaborate with other colleagues. I am thankful for the freedom and flexibility that I had in my research to search out answers, come to my own conclusions, and take ownership of my work. I appreciated how he recognized, encouraged, and affirmed my own leadership and mentorship abilities. I am grateful to have observed how he recognized that there is

not a one-size-fits-all approach to mentorship, as he carefully guides each student differently to truly bring out their greatest potential.

I also want to thank the National Science Foundation (NSF) and the Mustard Seed Foundation for their financial support. These two organizations invested in my work, seeing potential in my current academic endeavors and future professional career. The vote of confidence in terms of intellectual merit, broader impact, technical abilities, leadership pursuits and vocational goals has helped propel me though the doctoral process. The freedom and flexibility afforded from these fellowships has allowed me the opportunity to address interesting and significant research questions that I may not have been able to pursue otherwise.

I would like to acknowledge support from Dr. Mark Neifeld and the DARPA Seedling Grant for funding related to my synthetic aperture work. In addition, a word of thanks is extended to the Duke Imaging and Spectroscopy Program under the direction of Dr. David Brady. The interactions with this research group provided for insightful discussion and increased motivation toward our desired research goals.

I am grateful for my dissertation committee, Dr. Jannick Rolland, Dr. David Williams and Dr. Robert Clark for pushing me to answer tough questions and making me a stronger scientist and engineer.

Thanks to all my group members, past and present: Sam Thurman, Greg Brady, Matt Bolcar, Nathan Clark, Sapna Shroff, Tom Zielinski, Manuel Guizar-Sicairos, Alden Jurling, Abhishek Kumar, Dustin Moore, Zack DeSantis and Matt

Bergkoetter. A call out to each group member might be a dissertation in itself! These individuals provided insights and suggestions when I was stuck on a research problem, troubleshooted all my various computer maladies along the way and were genuinely a fun group of peers to work with on a day-to-day basis. A note of appreciation must be extended to Sam Thurman, whose research and Matlab code was a foundational starting point for much of the work described in this thesis. A special thanks to my officemate, Manuel Guizar-Sicairos. Manuel inspired me both in terms of his academic abilities and research prowess (it's incredibly stimulating to work alongside someone so motivated and driven to research excellence!), but also his humbleness, unselfishness, and willingness to teach and help others along the way.

I would like to add a note of thanks to Ricky Marron and Krista Lombardo for allowing me the opportunity to provide a mentorship role during their summer in our research group and laboratory. Their excitement and enthusiasm for jumping into new topics and exploring new areas with me was highly rewarding.

A well-deserved thanks is extended to The Institute of Optics at-large for providing a welcoming sense of community and an environment for engaging intellectual exchange. Thank you to the administrative staff for your countless interactions: Betsy Benedict, Maria Schnitzler, Lori Russell, Per Adamson, Lissa Cotter, Gayle Thompson, Gina Kern, Marie Banach and Noelene Votens. Betsy deserves credit for getting me to The Institute of Optics in the first place by

personally calling me and inviting me to spend the summer of 2004 participating in NSF REU program (and the rest is history from there!). I absolutely loved working with Maria on the Institute's prospective visit weekend when I was Junior Graduate Representative to the department, and I didn't stop dropping by her office after that. Lori was instrumental with her assistance in communications with Facilities and Services when I was setting specifications and requirements for new laboratory space in the Goergen Biomedical Engineering and Optics building.

I would be amiss to not acknowledge the countless friendships I have formed throughout my time at the Institute. I cannot even begin to describe how all my classmates have widened my global perspective and increased my love of other cultures. I will always remember sharing together in extended homework sessions, as well as relaxing meals and holiday celebrations. A special thanks to Prashant Baveja for alerting me and encouraging me to apply to the NSF National Nanotechnology Infrastructure Network Winter School in Mumbai, India.

I special note of gratitude to all those who have helped create a sense of real community for me here in Rochester, demonstrated wholeheartedly what friendship and faith is all about, and made Rochester a home for me over the past six years.

My utmost love goes out to Aaron Watnik for coming alongside me in the midst of this serious undertaking. I am thankful for the many ways that he provided me balance and perspective so that I didn't get burned out, encouragement to do my best, and motivation to finish strong.

None of this dissertation would be possible without the support and encouragement of my family, from an early age and continuing on today. Sources of strength and inspiration for me through my graduate studies have been their prayers in times of discouragement, as well as their joy and excitement in times of celebration. I am very appreciative that my family has demonstrated trust in my decisions and confidence in my abilities. I am thankful that they have allowed me to seek adventure, take risks, and dream big. My family has modeled a healthy work ethic, focused determination and the optimism to pursue opportunities to their full potential, and for that am I very grateful.

Abstract

Phase aberrations due to atmospheric turbulence, experimental conditions or the imaging system itself can severely limit the resolution of an image. Phase aberrations can be spatially dependent, meaning that a linear, space-invariant transfer function cannot fully correct for all the phase errors across the field-of-view. One can use digital holography to access the complex-valued optical field from a laser-illuminated object after detecting the intensity interference between object and reference beams. Then one can digitally apply phase corrections to the field and propagate that field to the object plane to form an image. In this work, we developed image sharpening approaches to the correction of phase aberrations in digital holography. Image sharpening algorithms employ a nonlinear optimization routine to sense and compensate the phase aberrations to form a fine-resolution reconstructed image. In this thesis, we examined phase correction for two specific applications: imaging through multiple phase screens and synthetic-aperture digital holography. In both cases, our work concentrated on numerical simulation, algorithm development, and implementation of laboratory experiments.

For imaging through phase screens, we developed a modified sharpness metric which preserves the space-bandwidth product upon propagation to prevent oversharpening the image. We successfully demonstrated successful image reconstructions through multiple phase screens in numerical simulation for two and

three phase screens and in a laboratory experiment for two phase screens, simulating space-variant aberrating media such as volume atmospheric turbulence.

Synthetic aperture digital holography (SADH) takes a collection of individual translated holographic frames and mosaics them to form a larger aperture. This increased aperture size results in greatly increased resolution (if not degraded by phase aberrations). We developed multiple approaches to aberration correction in SADH. We demonstrated the use of slope measurements between hologram sub-apertures with a non-iterative modal reconstructor to correct lower-order phase errors. Using an angular spectrum propagation technique with an image sharpening approach, we have demonstrated higher-order aberration correction and diffraction-limited resolution for a 12,000 by 18,000 pixel synthetic aperture. Finally, using an approximate Fresnel-like propagator in combination with an image sharpening algorithm, we demonstrated high-resolution, nonparaxial imaging over a region-of-interest for a 32,768 by 32,768 pixel (full gigapixel) synthetic aperture.

Table of Contents

List of Tables

List of Figures

List of Acronyms

AO	Adaptive optics
Ar+	Argon-ion
AS	Angular spectrum
B/S	Beamsplitter
CC	Cross-correlation
CD	Compact disk
CCD	Charge-coupled device
CG	Conjugate gradient
CMOS	Complementary metal-oxide-semiconductor
DFT	Discrete Fourier transform
DN	Digital number
DOF	Depth-of-focus
FOV	Field-of-view
FT or FFT	Fast Fourier Transform
GPUs	Graphics processing units
MCAO	Multi-conjugate adaptive optics
ND	Neutral density
OD	Optical density
PSF	Point spread function
PSNR	Peak signal-to-noise
RMS	Root-mean-square
ROI	Region-of-interest
SADH	Synthetic aperture digital holography
SAR	Synthetic aperture radar
SH	Shack-Hartmann
SNR	Signal-to-noise
UAV	Unmanned aerial vehicle
USAF	United States Air Force

List of Symbols

α	Scaling constant
a	$\frac{k}{2}\frac{z_r - z}{z_r z}$
$\mathcal{A}\left[z; g(x,y)\right]$	Angular spectrum propagator of an arbitrary field $g(x,y)$
b,c	Shifting coordinates in detector plane
β	Power for sharpness metric
c_j	Expansion coefficient
$\delta(f_x, f_y)$	2-D Dirac delta function
D	Detector width
E^2	Absolute squared error metric
f_c	Spatial frequency component of the object field
Δf	Sample spacing in spatial frequency domain
$f_k(\xi,\eta)$	k^{th} speckle realization of the image field
$\tilde{F}_k(f_\xi, f_\eta)$	Fourier transform of the k^{th} speckle realization of the field in the image plane
$F(x,y)$	Object field in detector plane
$\tilde{F}(f_x, f_y)$	Fourier transform of $F(x,y)$
$\mathcal{F}_r\left[z_1; f_k(\xi,\eta)\right]$	Fresnel transform
FT	Fast Fourier transform
$G(x,y)$	Complex field in detector plane, $F(x,y)R^*(x,y)$
$G_f(x,y)$	Filtered field in the detector plane
$G_i(x,y)$	Ideal complex field in the detector plane
$G_{ROI}(x,y)$	Field in the detector plane after applying a ROI mask in the image plane

g_c	Compression gain
G_n	A/D gain factor
$H(x,y)$	Hologram intensity
$\tilde{H}(f_x,f_y)$	FFT of $H(x,y)$
$H_n(x,y)$	Holographic intensity in detector plane with noise
$I(\xi,\eta)$	Intensity of the image
$I_{inc}(\xi,\eta)$	Incoherent intensity in the object plane
$I_{ideal}(\xi,\eta)$	Intensity of the ideal image
K	Number of speckle realizations
k	Wavenumber, $2\pi/\lambda$, or speckle realization index
κ	Upsampling factor
k_x, k_y	Transverse components of the reference wavevector
L	Width of isoplanatic patch
m	Number of elements
M	Number of sub-arrays
$M_n(\xi,\eta)$	Mask in the image plane
N	Array size (in pixels)
n	Number of bars
$N_{01,k}(x,y)$	k^{th} realization of real-valued, zero-mean, unit-variance Gaussian random numbers
OD	Optical density
P	Number of phase screens
p	Phase screen index
ρ	Spatial resolution
$\mathcal{P}_{0\to p-}\left[f_k(\xi,\eta)\right]$	Forward propagator
$\mathcal{P}^{\dagger}_{P+1\to p-}\left[G_k(u,v)\right]$	Inverse propagator

$R(x, y)$	Reference field in detector plane
$\tilde{R}(f_x, f_y)$	FFT of $R(x, y)$
$r(x, y)$	Reference source location applied at the detector plane, $\sqrt{(x-\xi_r)^2+(y-\eta_r)^2+{z_r}^2}$
$R_0(x, y)$	Amplitude of the reference beam
r_0	Fried's parameter
S	Modified sharpness metric
S_1	$\sum_{\xi,\eta} I^{\beta}(\xi,\eta)$, Sharpness metric
S_2	$\alpha \sum_{k=1}^{K} \sum_{f_\xi, f_\eta} M(f_\xi, f_\eta) \left\|F_k(f_\xi, f_\eta)\right\|^2$, Regularization term
$s_{x,m}$, $s_{y,m}$	Wavefront slope
$SNR(x, y)$	SNR in detector plane
T	Transmittance of optical density filter
$t_{x,m}$, $t_{y,m}$	Translations (pixels)
w	Object width
$W_k(f_\xi, f_\eta)$	Weighting function defined by the spatial frequency content
Δx	Detector pixel pitch
z	Distance between object and detector
z_p	Distance from the $(p-1)^{th}$ phase plane to the p^{th} phase plane
σ_r	RMS read noise
λ	Wavelength
θ_D	Angular extent of the detector
$\theta_{\max}$	Maximum angle of a ray from the object collected by the detector array

θ_w	Angular extent of the object
$\phi_r(x,y)$	Phase correction due to the reference source location, $kr(x,y)$
$\phi_p(x_p,y_p)$	Phase error in the p^{th} plane
$\phi(x,y)$	Wavefront aberration
$\varphi_{SV}(x,y,\xi_0,\eta_0)$	Space-variant phase error
$\Delta\varphi$	Maximum phase difference between the estimated phase error and the actual phase error
$\psi_j(x,y)$	Basis function of $\phi_p(x,y)$
(ξ,η)	Image/object coordinates
(ξ_r,η_r,z_r)	Position of the reference point source
(x,y)	Detector plane coordinates

Foreword

The author performed all work described in this thesis unless specified below:

Chapter 2, Section 2: Prof. James Fienup derived the theory portion of the weak-signal case and is included here in order for the work presented in this chapter to be self-contained.

Chapter 4, Section 1: Ricky Marron produced the phase screens used in this experiment.

Chapter 7, Section 3: The gradients and the Matlab code for the optimization of the reference location were done by Abhishek Kumar.

1. Introduction

1.1. Motivation

Phase aberrations can be a limiting factor for determining resolution in turbulent media conditions, with applications both in ground and airborne imaging scenarios as well as medical imaging. In the case of ground-to-ground, or horizontal path imaging, phase aberrations are the result of extended volume atmospheric turbulence. In that case, light scattering from two spatially separated points can pass through different portions of the atmosphere, introducing an undesirable anisoplanatic (space-variant blurring) imaging effect. An imaging system is anisoplanatic when the image of a point source object is position-dependent throughout the field-of-view and cannot be compensated for by a linear, space-invariant transfer function.

For the airborne imaging case, an optical design goal may be to put high-resolution, wide field-of-view imaging systems on a small unmanned aerial vehicle (UAV). A challenge with such a system is countering off-axis geometric ray aberrations to maintain a large field-of-view (FOV) with an increase in aperture area and resolution. Enhancing image quality and resolution for ground and airborne imaging applications by correction of phase aberrations is the motivation of my research in coherent digital holography.

1.2. Introduction to Digital Holography

Holography is a process by which the interference between a light beam reflected from a coherently illuminated object and a coherent reference wave are recorded.

Light from a laser source is spilt into two beam paths, the difference between which is within the coherence length of the laser. One of these light fields creates a reference wavefront, typically a plane wave. The other light is directed to the object. Objects can be transmissive or reflective in nature; the light passing through, or reflecting from the object creates an interference pattern with the plane reference wavefront on a detector.

Digital holography, more specifically, denotes that this interference is recorded on a digital detector array, such as a CMOS or CCD device. Despite the fact that the detector records only the intensity, both the amplitude and phase of the complex field can be extracted due to the interference between the beams. By recording this information digitally, the field from the object can be extracted in a computer and an image may be reconstructed by numerically propagating to the plane of the image.

An example set-up for recording a digital hologram is shown in Figure 1-1. The interference between the reference and the object fields can be written as

$$H(x,y) = \left|R(x,y) + F(x,y)\right|^2, \tag{1.1}$$

where $R(x,y)$ is the reference field and $F(x,y)$ is the object field. This interference intensity can be expanded as

$$H(x,y) = \left|R(x,y)\right|^2 + \left|F(x,y)\right|^2 + R(x,y)F^*(x,y) + R^*(x,y)F(x,y). \tag{1.2}$$

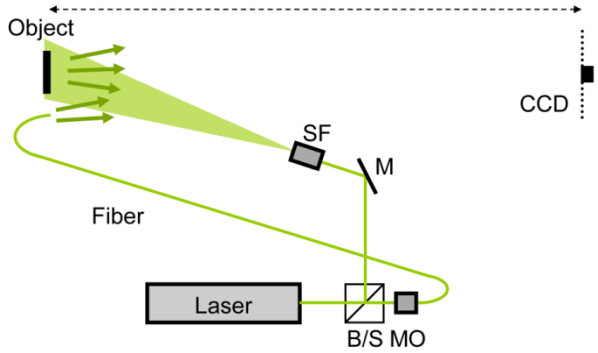

Figure 1-1. Experimental setup for off-axis, lensless Fourier transform DH synthetic aperture arrangement. B/S, beamsplitter; M, mirror; SF, microscope objective plus pinhole spatial filter; and MO, microscope objective.

To extract the object field from the collected data, the recorded intensity, $H(x,y)$, is first Fourier transformed, giving

$$\begin{aligned}\tilde{H}(f_x,f_y) &= \iint H(x,y)\,e^{-i2\pi(f_x x+f_y y)}\,dxdy \\ &= \tilde{R}(f_x,f_y)*\tilde{R}^*(-f_x,-f_y)+\tilde{F}(f_x,f_y)*\tilde{F}^*(-f_x,-f_y) \\ &\quad +\tilde{F}^*(-f_x,-f_y)*\tilde{R}(f_x,f_y)+\tilde{F}(f_x,f_y)*\tilde{R}^*(-f_x,-f_y).\end{aligned} \tag{1.3}$$

where $\tilde{R}(f_x,f_y)$ and $\tilde{F}(f_x,f_y)$ are the Fourier transforms of the functions $R(x,y)$ and $F(x,y)$, respectively, and $*$ (in-line asterix) denotes convolution defined by $q(\xi,\eta)*h(\xi,\eta)=\int_{-\infty}^{\infty}\int q(\xi,\eta)\,h(x-\xi,y-\eta)\,d\xi d\eta$, * (superscript asterix) denotes complex conjugation, and $\tilde{R}(f_x,f_y)*\tilde{R}^*(-f_x,-f_y)$ and $\tilde{F}(f_x,f_y)*\tilde{F}^*(-f_x,-f_y)$ are autocorrelation terms, $\tilde{F}(f_x,f_y)*\tilde{R}^*(-f_x,-f_y)$ is the object term and

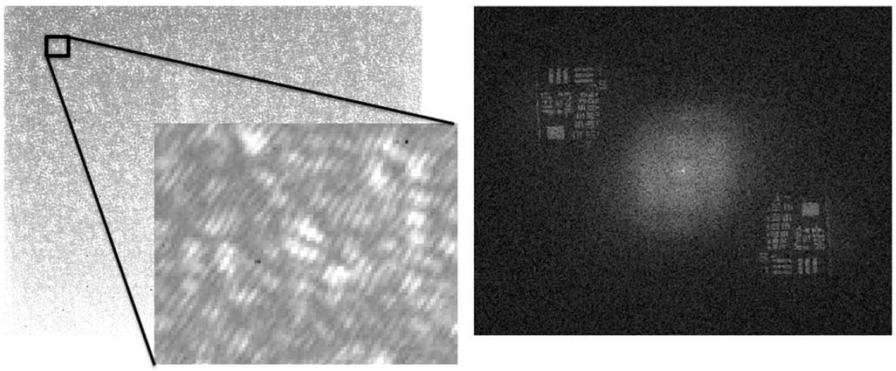

Figure 1-2. (a) Detected hologram frame, inset shows interference fringes. (b) Fourier transform of detected hologram reveals image, twin image and autocorrelation terms of the hologram.

$\tilde{F}^*(-f_x,-f_y)*\tilde{R}(f_x,f_y)$ is the twin-image term. Figure 1-2 depicts the hologram detection process.

Several different geometries exist for the position of the object and the reference source. The first hologram geometry, proposed by Gabor, used a transmissive object which was co-linear in position with the source illumination for an in-line geometry [1]. Although appropriate in some situations, a major limitation for this type of hologram is the overlap of the image and twin image (the coordinate-reversed, complex conjugate of the image field). An alternative geometry, originally proposed by Leith and Upatnieks [2], uses an offset angle for the reference wavefront. The advantage of this approach is that, with proper selection of an offset angle, the various wave components can be separated such that the desired term, the term containing the field of the image, $\tilde{F}(f_x,f_y)*\tilde{R}^*(-f_x,-f_y)$ can be isolated from the other three terms. The complex field from the object, $F(x,y)$, with both amplitude

and phase information in the plane of the detector, can be recovered by first applying an inverse Fourier transform to give $R^*(x,y)F(x,y)$ and then dividing by $R^*(x,y)$. The resulting image is found by numerically propagating the field (with either a Fresnel or angular spectrum propagator) the distance to the object plane.

This early work from Gabor in 1948 and Leith and Upatnieks in 1962 has been applied to a variety of science and engineering problems as well as to art and display. In 1967, Goodman and Lawrence [3] published the first experiment showing the digital formation of images from electronically detected holograms. Previous to this, the most common form of holography was recording a hologram on a photographic plate and reconstructing the hologram optically. Both the detection and image formation techniques were analog rather than digital. Enloe et al. [4] performed a hybrid experiment, in which a vidicon was used as a detector, but the reconstruction of the image was obtained optically by photographing the output of a TV monitor. By both detecting the hologram and reconstructing the image digitally, Goodman and Lawrence were able to streamline the holographic process. Digital holography has found use in applications for biomedical microscopy [5, 6], x-ray optics/imaging [7], metrology for surfaces [8], optical communications [9], data storage [10] and remote sensing [11]. Our work primarily focuses on the application area of long-range imaging, although it can be applied to these other areas as well.

1.3. Advantages of Digital Holography

Digital holography, as an active, coherent, phase-measuring imaging modality, has several advantages over conventional imaging. One advantage of digital holography is the ability to eliminate the use of imaging optics. Instead of the need for optics to relay the image to the focal plane, a detector, in combination with an optical element (such as a beamsplitter) to provide the local oscillator or reference illumination, can record data in the pupil plane. This reduces the system's weight and bulkiness (specifically its longitudinal depth), and can also make possible the elimination of the aberrations imparted from off-axis aberrations present in imaging systems consisting of lenses and mirrors. Since an active imaging system, such as digital holography, provides its own illumination source, it can operate in both day and nighttime conditions, not being dependent on solar illumination. Digital holography, unlike passive imaging systems, allow for access to not only the amplitude information, but also the phase of the field. Access to the phase allows post-detection refocusing for imaging deep objects, multidimensional (3-D) imaging [12], and coherent change detection [13]. One drawback inherent in coherent imaging is the presence of speckle noise. However, different techniques such as averaging multiple speckle realizations can be performed to lower the speckle noise in the image.

1.4. Sharpness Metrics

Image sharpening algorithms employ sharpness metrics that rate the image quality quantitatively to minimize the phase aberrations in the reconstructed images. Image sharpness is a metric which ideally has a maximum value only for an unblurred

image. Muller and Buffington [14] presented a set of different sharpness metrics that were proved to reach their maximum value without aberrations for incoherent imaging. They also showed that amplitude aberrations are unimportant to image sharpness, while phase aberrations will reduce the central maximum of a point spread function (PSF), increase the sidelobes of the PSF and increase the width of the main lobe. Muller and Buffington's work in sharpness metrics was motivated by the application of correcting atmospherically degraded images within the isoplanatic patch with an adjustable phase shifter with incoherent light from a telescope.

Paxman and Marron [15] first applied sharpness metrics to coherent, speckled imagery from synthetic-aperture radar having 1-D phase errors. This work used iterative methods to correct for low-order phase errors (introducing a phase correction and calculating the resulting sharpness value). Fienup [16] showed that nonlinear optimization algorithms can improve the computational efficiency of maximizing the sharpness, as well as correct for arbitrarily high-order phase errors. The nonlinear optimization approach employed analytic gradients of the sharpness with respect to the phase error.

Fienup and Miller [17] examined sharpness metrics from the perspective of the second derivative of the metric. The larger the second derivative of the sharpness metric is, the greater the stretch in the histogram of intensity values, resulting in an increased contrast and standard deviation of the value of the intensities from the mean. Bright pixels become brighter, and vice versa, dark pixels become darker.

Fienup and Miller presented "designer" sharpness metrics, recognizing that the choice of sharpness metric is dependent upon the image content. For example, using the sharpness metric

$$S_1 = \sum_{\xi,\eta} I^{\beta}(\xi,\eta), \tag{1.4}$$

where $I(\xi,\eta)$ is the intensity of the image and β is the power to which the intensity is raised, images of point-like objects sharpened best with large values of β, while images with dark regions sharpen best with powers of β near 1 [17, 18]. Thurman [18] applied sharpness metrics to 2-D phase errors, while previous work in synthetic aperture radar (SAR) was for 1-D phase errors, and performed an extensive parameter study including number of speckle realizations, power of sharpness metric, and noise. Sharpness metrics have been applied to a variety of problems including adaptive optics for turbulence correction [19, 20], imaging of aircraft [21], medical ultrasound [22], synthetic aperture radar (SAR) [16, 23] and optical trapping [24]. In this work, I draw upon the results presented in the sharpness metric literature when considering a suitable sharpness metric for each specific image scene.

1.5. Atmospheric Turbulence, Horizontal Path Imaging and a Thin Phase Screen Model

Imaging through atmospheric turbulence provides a rich context and motivation for the research presented in this thesis. Atmospheric turbulence refers to fluctuations in index of refraction of the atmosphere as a result of temperature, pressure, velocity or moisture changes. These fluctuations or inhomogeneities in the refractive index of

the air introduce aberrations into the path of any propagating wavefront. Significant contributions to the classical theory of turbulence were developed in the 1940s by Kolmogorov [25, 26] and subsequently expanded by Tatarski in the 1960s [27]. Building upon the work of propagation through turbulence, Fried examined the effects of turbulence on the resolution of imaging systems [28, 29]. In this work, he derived a parameter r_0, referred to as the atmospheric coherence diameter or Fried's parameter. Fried's parameter can appropriately be interpreted as the maximum useful aperture size in the presence of turbulence in terms of resolution (i.e. further increasing the aperture size will not further increase resolution).

In addition to the significant body of work devoted to the understanding of the statistical nature of turbulence, several authors have investigated modeling propagation through atmospheric turbulence by reducing an extended volume of turbulence to a collection of thin random phase screens [30-33]. Phase screens used to model the atmosphere are phase-only functions, $\exp\left[i\phi\left(x,y\right)\right]$. As opposed to actual turbulence conditions where there are phase perturbations throughout the entire medium, the random phase screen simulation only has phase perturbations at discrete distances within the propagation media. A phase screen approach can still accurately model the statistics and anisoplanatic conditions of the turbulence, while at the same time allowing for a simplified approach for digital propagation.

1.6. Introduction to Anisoplantic Imaging through Phase Screens

We build upon previous work using sharpness metrics in digital holography to correct for isoplanatic and anisoplanatic phase errors. Thurman and Fienup showed isoplanatic correction [18] and anisoplanatic (realized by a single aberrating phase screen separated in z from the entrance pupil) image correction [34]. Marron *et. al.* [35] demonstrated image correction over a small region of the entire field of view in the presence of anisoplanatic phase errors, also by applying a phase correction in one plane. These previous methods do not take into account the effect of multiple phase screens and, as a result, can only correct for one plane of phase errors. Consequently, these methods can only correct over a limited field of view in the presence of multiple phase screens or volume turbulence conditions. Our approach addresses both of these issues, as we have derived the necessary mathematical framework to account for the multiple phase planes in our nonlinear optimization gradient calculations while allowing for correction of multiple planes, thereby correcting the image over the entire field of view, not limited to an isoplanatic imaging patch. Wenski and Mason [36] demonstrated anisoplanatic correction results with an array of point sources. Using a sharpening algorithm to correct the imagery, point-like objects are easier to work with compared to extended objects without any prominent point scatterers. We have shown in our work the ability to provide phase correction in multiple planes for extended objects as well as point-source objects.

1.7. Comparison with Adaptive Optics

It is advisable to compare existing technologies and scientific techniques that may be seen as a direct or indirect competitor to the new methods being proposed. An alternative approach to aberration correction is adaptive optics (AO). For AO technology, a wavefront sensor measures distortions of the atmosphere and a deformable mirror corrects the light going to the science camera in order for the image to appear sharp. AO is a form of passive imaging as opposed to digital holography which is active imaging. The coherence requirement of digital holography limits the technique to objects near the earth (thousands of kilometers), not astronomical objects. In most existing AO systems, the deformable mirror, however, corrects for aberrations near the pupil plane which is equivalent to the detector plane in digital holography. Therefore, the correction is limited to the size of the isoplanatic patch, and requires a beacon/reference source to be present within the isoplanatic patch of the science object (for astronomical conditions with excellent observing conditions, this is typically a few tens of microradians) [37]. To overcome the isoplanatic patch limitation with classical astronomical AO, multi-conjugate adaptive optics (MCAO) uses more than one deformable mirror in different planes in combination with multiple guide stars to correct for phase effects in multiple planes.

Although similar with regards to correction in multiple planes, our methods using sharpness maximization have several advantages compared to AO with respect to the location and number of reference sources. MCAO requires multiple guide stars in order to achieve anisoplanatic correction [38] while sharpness correction relies on a

single local oscillator (the reference beam). For digital holography the object itself acts like the multiple guide stars found in astronomical AO.

One metric of comparison is system cost; sharpness optimization correction requires a single laser and high performance computing capabilities. An MCAO system not only requires computing resources for real-time wavefront sensing and computing mirror actuation commands, but also the added hardware costs of the wavefront sensor, multiple deformable mirrors and one or more laser sources. Additionally, since a sharpness-based approach is purely digital, this eliminates the need for mechanical components and moving parts associated with deformable mirror actuation.

One strength (or drawback, depending on the circumstances) of AO is the necessity to calculate and perform correction in real time. Digital holography, on the other hand, can collect data and form an image off-line. The current computational processing required using digital holography to estimate multiple phase screens is on the order of tens of minutes for a 1200 x 1600 pixel image, not milliseconds, as would be considered real-time for the time scales of changing turbulence. We believe that with efficient programming and dedicated hardware such as graphics processing units (GPUs), it may be possible to significantly reduce the computation time needed to estimate these phase errors. Depending on the factors (cost, size, weight, reliability, quality of images, etc.) that are used to determine the best technologies, we

believe that digital holography using sharpness correction shows good promise for scientific, military, homeland security, and biological imaging.

1.8. Introduction to Synthetic-Aperture Digital Holography

In synthetic-aperture digital holography, a collection of individual digital holography frames can be acquired by laterally and/or vertically translating a modest-sized detector over a larger spatial area. The detected frames are mosaicked together to form a combined, larger aperture. A synthetic aperture allows for an increased numerical aperture, resulting in the collection of higher spatial frequencies and improved image resolution. The total space-bandwidth product of the system is increased proportionally. The advantage of high-resolution imaging over a wide field-of-view has motivated several groups to pursue this area of research. Issues such as registering overlapping portions of adjacent frames [39] or handling experimental higher-order phase aberrations [40] have been addressed. As a result of working through some of these practical experimental considerations, the size of the synthetic apertures continues to increase from early work with synthetic apertures of 1.3 Mpix [39] to our current work in synthetic apertures that are gigapixel in size [41].

Aperture synthesis with digital holography has been performed by creating a mosaic of individual frames to form a larger, monolithic aperture [39, 42-44]. Cross-correlation techniques are commonly used to align and register frames together [39, 40, 42, 45, 46]. As the synthetic aperture becomes larger, the system tolerance

requirements become more demanding. For example, the depth of field is reduced with larger apertures, scaling by the inverse of the aperture width squared, i.e., $DOF = \lambda (z/D)^2$.

To correct for the axial position of the plane of the object and for objects whose depth exceeds the depth of field, dynamic focusing must be performed. To avoid aberrations due to a drift in the reference beam (local oscillator) phase relative to the object beam, phase-error correction algorithms are needed. Massig [39] addressed piston phase differences between frames by averaging phase differences in overlap regions and then subtracting offsets from individual frames. Binet *et al.* [44] showed that optical aberrations such as defocus and astigmatism were present after forming a synthetic aperture. Compensation for aberrations in [44] were found *a posteriori* through means of manual user optimization.

Sharpness metric phase-error approaches have also been applied to distributed apertures [47, 48]. These apertures consist of a small number of telescopes. The sharpness correction applied in Ref. [47, 48] was a two-step procedure: first, images from individual sub-apertures were sharpened, and then the sub-apertures were combined into a single large array and the aberrations were corrected over the larger effective aperture. Phase corrections were made using Zernike polynomials centered on each individual sub-aperture being corrected (no global phase error correction). Although these authors used sparse apertures, and our work focused on a monolithic aperture, similar processing routines may be used for both scenarios.

1.9. Overview of Work

In this thesis, I implemented new algorithms and strategies to compensate for phase aberrations in multiple phase screen and in synthetic aperture imaging. I utilized numerical simulation and laboratory experiments to understand and mitigate atmospheric turbulence-like effects in multiple phase screen imaging. I also addressed critical design challenges of a lensless imaging system composed of a synthetic aperture to yield high-resolution, wide-field images. My research concentrates on two prevalent challenges present in ground and airborne imaging: correcting turbulent atmosphere and maintaining high resolution over a wide field-of-view. The methodology of my research has included significant modeling and numerical simulation, algorithm development, design and implementation of laboratory experiments, and quantitative evaluation of reconstructed images.

Chapter 2 examines the conditions that exist for the weak-signal regime of a digital holography experiment. This photon-limited scenario allows for reduced requirements on the laser power for holography applications and holds relevance both for horizontal-path and airborne applications.

Chapters 3 and 4 detail my contributions to imaging through multiple phase screens in a digital holography experiment and reconstructing fine-resolution images by estimating for the aberrations and correcting them. Chapter 3 examines this approach in computer simulation, which was the first ever reported two- and three-

plane phase correction in the literature, while Chapter 4 describes laboratory experiments that prove this technique.

Work in synthetic-aperture imaging for digital holography is described in Chapter 5, 6 and 7. Chapter 5 describes the laboratory experiment to acquire large synthetic-aperture holograms and the process to mosaic the collection of individual frames to form a single large aperture and form images, including the largest digital holography synthetic aperture ever.

Chapter 6 describes three methods used to increase the quality and resolution of the reconstructed images. The first method, speckle averaging, is used as a benchmark approach to demonstrate the improvement in resolution by decreasing the speckle noise in the images. The remaining two techniques estimate system aberrations in one of two ways: a non-iterative modal reconstruction using sub-aperture slope measurements and a sharpness maximization approach. Results are provided for all these image reconstruction techniques.

Chapter 7 addresses some additional challenges encountered when reconstructing images from extremely large apertures (gigapixel in size), including sampling issues and ghosting encountered in image formation by non-paraxial, wide-field propagation. An approach to recover high-resolution images has been developed which involves propagating and correcting for aberrations over a limited instantaneous field-of-view of the image. I provide a detailed description of the theory and approach used as well as image reconstruction results.

1.10. References

1. D. Gabor, "A new microscope principle," Nature **161**, 777-778 (1948).

2. E. N. Leith and J. Upatnieks, "Wavefront reconstruction and communication theory," J. Opt. Soc. Am. **52**, 1123-1130 (1962).

3. J. W. Goodman and R. W. Lawrence, "Digital Image Formation From Electronically Detected Holograms," Appl. Phys. Lett. **11**, 77-79 (1967).

4. L. H. Enloe, J. A. Murphy, and C. B. Rubinstein, Bell System Tech. J. **45**, 335 (1966).

5. N. T. Shaked, T. M. Newpher, M. D. Ehlers, and A. Wax, "Parallel on-axis holographic phase microscopy of biological cells and unicellular microorganism dynamics," Appl. Opt. **49**, 2872-2878 (2010).

6. A. Khmaladze, M. Kim, and C. M. Lo, "Phase imaging of cells by simultaneous dual-wavelength reflection digital holography," Opt. Express **16**, 10900-10911 (2008).

7. E. Guehrs, C. M. Gunther, B. Pfau, T. Rander, S. Schaffert, W. F. Schlotter, and S. Eisebitt, "Wavefield back-propagation in high-resolution x-ray holography with a movable field of view," Opt. Express **18**, 18922-18931 (2010).

8. Y. Kikuchi, D. Barada, T. Kiire, and T. Yatagai, "Doppler phase-shifting digital holography and its application to surface shape measurement," Opt. Lett. **35**, 1548-1550 (2010).

9. H. H. Wahba and T. Kreis, "Characterization of graded index optical fibers by digital holographic interferometry," Appl. Opt. **48**, 1573-1582 (2009).

10. J. F. Heanue, M. C. Bashaw, A. J. Daiber, R. Snyder, and L. Hesselink, "Digital holographic storage system incorporating thermal fixing in lithium niobate," Opt. Lett. **21**, 1615-1617 (1996).

11. J. W. Stafford, B. D. Duncan, and M. P. Dierking, "Experimental demonstration of a stripmap holographic aperture ladar system," Appl. Opt. **49**, 2262-2270 (2010).

12. J. C. Marron and K. S. Schroeder, "3-Dimensional Lensless Imaging Using Laser Frequency Diversity," Appl. Opt. **31**, 255-262 (1992).

13. T.-C. Poon, *Digital holography and three-dimensional display : principles and applications,* (Springer, New York, 2006).

14. R. A. Muller and A. Buffington, "Real-time correction of atmospherically degraded telescope images through image sharpening," J. Opt. Soc. Am. **64**, 1200-1210 (1974).

15. R. G. Paxman and J. C. Marron, "Aberration correction of speckled imagery with an image-sharpness criterion," Proc. SPIE **976**, 37-47 (1988).

16. J. R. Fienup, "Synthetic-aperture radar autofocus by maximizing sharpness," Opt. Lett. **25**, 221-223 (2000).

17. J. R. Fienup and J. J. Miller, "Aberration correction by maximizing generalized sharpness metrics," J. Opt. Soc. Am. A **20**, 609-620 (2003).

18. S. T. Thurman and J. R. Fienup, "Phase-error correction in digital holography," J. Opt. Soc. Am. A **25**, 983-994 (2008).

19. A. Buffington, F. S. Crawford, S. M. Pollaine, C. D. Orth, and R. A. Muller, "Sharpening stellar images," Science **200**, 489-494 (1978).

20. M. A. Vorontsov, G. W. Carhart, D. V. Pruidze, J. C. Ricklin, and D. G. Voelz, "Adaptive imaging system for phase-distorted extended source and multiple-distance objects," Appl. Opt. **36**, 3319-3328 (1997).

21. B. D. Steinberg, "Microwave imaging of aircraft," Proc. IEEE **76**, 1578-1592 (1988).

22. L. Nock, G. E. Trahey, and S. W. Smith, "Phase aberration correction in medical ultrasound using speckle brightness as a quality factor," J. Acoust. Soc. Am. **85**, 1819-1833 (1989).

23. T. J. Schulz, "Optimal sharpness function for SAR autofocus," IEEE Sig. Proc. Lett. **14**, 27-30 (2007).

24. K. D. Wulff, D. G. Cole, R. L. Clark, R. DiLeonardo, J. Leach, J. Cooper, G. Gibson, and M. J. Padgett, "Aberration correction in holographic optical tweezers," Opt. Express **14**, 4169-4174 (2006).

25. U. Frisch and A. N. Kolmogorov, *Turbulence : the legacy of A.N. Kolmogorov,* (Cambridge University Press, Cambridge, Eng. ; New York, 1995).

26. M. C. Roggemann and B. Welsh, *Imaging through turbulence,* (CRC Press, Boca Raton, 1996).

27. V. I. Tatarskii, *Wave propagation in a turbulent medium,* (Dover Publications, 1967).

28. D. L. Fried, "Statistics of a Geometric Representation of Wavefront Distortion," J. Opt. Soc. Am. **55**, 1427-1431 (1965).

29. D. L. Fried, "Optical Resolution Through a Randomly Inhomogeneous Medium for Very Long and Very Short Exposures," J. Opt. Soc. Am. **56**, 1372-1379 (1966).

30. R. G. Paxman, B. J. Thelen, and J. J. Miller, "Optimal simulation of volume turbulence with phase screens," Proc. SPIE **3763**, (1999).

31. H. G. Booker, J. A. Ferguson, and H. O. Vats, "Comparison between the extended-medium and the phase-screen scintillation theories," J. Atmos. Ter. Phys. **47**, 381-399 (1985).

32. L. C. Andrews and R. L. Phillips, *Laser beam propagation through random media,* 2nd (SPIE Press, Bellingham, Wash., 2005).

33. J. M. Martin and S. M. Flatte, "Intensity Images and Statistics from Numerical-Simulation of Wave-Propagation in 3-D Random-Media," Applied Optics **27**, 2111-2126 (1988).

34. S. T. Thurman and J. R. Fienup, "Correction of anisoplanatic phase errors in digital holography," J. Opt. Soc. Am. A **25**, 995-999 (2008).

35. J. C. Marron, R. L. Kendrick, N. Seldomridge, T. D. Grow, and T. A. Hoft, "Atmospheric turbulence correction using digital holographic detection: experimental results," Opt. Express **17**, 11638-11651 (2009).

36. T. E. Wenski and J. E. Mason, "Multiple screen image correction for digital holography," in *Coherent Laser Radar Conference* (2009), 217-220.

37. R. R. Parenti, "Adaptive Optics for Astronomy," Lincoln Lab. **5**, 93-114 (1992).

38. E. A. Laag, S. M. Ammons, D. T. Gavel, and R. Kupke, "Multiconjugate adaptive optics results from the laboratory for adaptive optics MCAO/MOAO testbed," J. Opt. Soc. Am. A **25**, 2114-2121 (2008).

39. J. H. Massig, "Digital off-axis holography with a synthetic aperture," Opt. Lett. **27**, 2179-2181 (2002).

40. A. E. Tippie, A. Kumar, and J. R. Fienup, "High-resolution synthetic-aperture digital holography with digital phase and pupil correction," Opt. Express **19**, 12027-12038 (2011).

41. A. E. Tippie and J. R. Fienup, "Gigapixel synthetic-aperture digital holography: sampling and resolution considerations," in *Computational Optical Sensing and Imaging* OSA Technical Digest (CD) (Optical Society of America, 2011), paper CWB1.

42. D. Claus, "High resolution digital holographic synthetic aperture applied to deformation measurement and extended depth of field method," Appl. Opt. **49**, 3187-3198 (2010).

43. F. Le Clerc, M. Gross, and L. Collot, "Synthetic-aperture experiment in the visible with on-axis digital heterodyne holography," Opt. Lett. **26**, 1550-1552 (2001).

44. R. Binet, J. Colineau, and J. C. Lehureau, "Short-range synthetic aperture imaging at 633 nm by digital holography," Appl. Opt. **41**, 4775-4782 (2002).

45. J. L. Di, J. L. Zhao, H. Z. Jiang, P. Zhang, Q. Fan, and W. W. Sun, "High resolution digital holographic microscopy with a wide field of view based on a synthetic aperture technique and use of linear CCD scanning," Appl. Opt. **47**, 5654-5659 (2008).

46. S. Lim, K. Choi, J. Hahn, D. L. Marks, and D. J. Brady, "Image-based registration for synthetic aperture holography," Opt. Express **19**, 11716-11731 (2011).

47. J. C. Marron and R. L. Kendrick, "Distributed aperture active imaging," Proc. SPIE **6550**, (2007).

48. D. Rabb, D. Jameson, A. Stokes, and J. Stafford, "Distributed aperture synthesis," Opt. Express **18**, 10334-10342 (2010).

2. Low Light Holography

2.1. Introduction

It is often desirable to recover signals that are very weak and beneath the noise floor of collected data. In digital holography, the laser light reflected from an object that reaches the detector array may be very weak due to the reflectivity of the object, the distance from the object, or operational constraints (power, eye safety, cost, etc.) on the laser used. Object detection can be highly critical in surveillance missions and other scenarios where the accurate identification of objects is necessary, even in environments of low signal-to-noise ratio (SNR).

Previous work by Gross and Atlan [1] in low-light digital holography concentrated on combining off-axis holography with phase-shifting holography. They suggested that the use of phase shifting was needed to remove the zero-order image and noise of the reference in order to recover a low object signal. We show that, for the case of a weak object and a strong reference, the image SNR depends only on the number of photons from the object and is independent of the strength of the reference as well as all other typical noise sources (photon noise from the reference, read noise, quantization noise). Our results show that only off-axis holography is necessary to achieve successful low-light image reconstructions, thus allowing for a single frame detection versus the collection of multiple (12) holographic frames used in the phase-shifting experiment [1]. We describe the theory

for low-light holography and demonstrate it with image reconstruction results both in simulation and a laboratory experiment.

2.2. Theoretical Development of SNR for the Weak-Signal Case

The signal from a single frame detected in the hologram plane with noise, in units of photoelectrons (e^-), can be modeled as

$$H_n(x,y) = Poisson\left[\left|R(x,y)+F(x,y)\right|^2\right] + \sigma_r N_{01,1}(x,y) \tag{2.1}$$

where *Poisson* represents the Poisson noise operator, $R(x,y)$ is a pure-phase reference beam, $F(x,y)$ is the field reflected from a coherently illuminated object, σ_r is the rms read noise, $N_{01,k}(u,v)$ is the k^{th} realization of real-valued, zero-mean, unit-variance Gaussian random numbers. When the mean number of photoelectrons is large (greater than 30, say), then to a very good approximation, the signal can be represented as

$$H_n(x,y) = \left|R(x,y)+F(x,y)\right|^2 + \sqrt{\left|R(x,y)+F(x,y)\right|^2}\,N_{01,2}(x,y) + \sigma_r N_{01,1}(x,y) \tag{2.2}$$

where we have used the fact that Poisson noise has a variance equal to the mean number of photoelectrons.

Next, consider the effect of quantization noise occurring during analog-to-digital conversion. A digital number (DN) coming from the camera can be modeled as

$$DN(x,y) = \frac{H_n(x,y)}{G_n} + \frac{1}{\sqrt{12}} N_{01,3}(x,y) \tag{2.3}$$

where G_n is the A/D gain factor and the second term is the quantization error [2], where the $\sqrt{12}$ factor comes from the rounding off of a real value to the nearest integer. Taking the square root of the sum of the squares of the standard deviations of the noise terms, we have

$$DN(x,y) = \frac{\left|R(x,y) + F(x,y)\right|^2}{G_n} + \sqrt{\frac{\left|R(x,y) + F(x,y)\right|^2 + \sigma_r^2}{G_n^2} + \frac{1}{12}} N_{01,4}(x,y). \tag{2.4}$$

Under some other circumstances additional noise terms might be required, such as for haze and dark current, but are outside the scope of this analysis.

For most digital holography scenarios, it is easy to have a strong reference beam, since it does not undergo the 1/distance^2 drop-off suffered by the beam at the detector array reflected by the object. We might have, for example, a well depth of 40,000 e^- and let the reference beam have an intensity of 80% of that (to keep within the linear range of the detector array), namely, $\left|R(x,y)\right|^2$ = 32,000 e^-. As other analysis shows [3], if one is concerned with recovering an incoherent image of the

object, then one does not benefit much by a stronger object beam once $\left|F\left(x,y\right)\right|^2$ exceeds a few photons per speckle. In order to not waste laser power, due to the fact that the laser power requirements is one of the more difficult aspects of digital holography for imaging remote objects, we can usually expect to have $\left|R\left(x,y\right)\right|^2 \gg \left|F\left(x,y\right)\right|^2$. Hence within the square root above we can approximate $\left|R\left(x,y\right)+F\left(x,y\right)\right|^2$ with $\left|R\left(x,y\right)\right|^2$. Furthermore, a reasonable detector having, say, 50 photoelectrons RMS of read noise will have σ_r^2 = 2,500 << $\left|R\left(x,y\right)\right|^2$ = 32,000, allowing us to ignore the read noise. In addition, unless G_n is an unusually large number, we will have $\left|R\left(x,y\right)\right|^2 \Big/ G_n^2 >> 1/12$. For these reasons, for digital holography or heterodyne sensing, the expression above can be well approximated by

$$DN\left(x,y\right) \approx \frac{\left|R\left(x,y\right)+F\left(x,y\right)\right|^2}{G_n} + \frac{\left|R\left(x,y\right)\right|}{G_n} N_{01,4}\left(x,y\right). \tag{2.5}$$

Note that when computing a SNR, the G_n in the expression above will cancel. Hence we can ignore that factor and think in terms of the measured intensity in units of photoelectrons, without the A/D gain factor,

$$\begin{aligned} H_n\left(x,y\right) &= \left|R\left(x,y\right)+F\left(x,y\right)\right|^2 + \left|R\left(x,y\right)\right| N_{01,4}\left(x,y\right) \\ &= \left|R\left(x,y\right)\right|^2 + \left|F\left(x,y\right)\right|^2 + R^*\left(x,y\right)F\left(x,y\right) \\ &\quad + R\left(x,y\right)F^*\left(x,y\right) + \left|R\left(x,y\right)\right| N_{01,4}\left(x,y\right) \end{aligned} \quad . \tag{2.6}$$

In this expression, the desired term is the third term, $R^*(x,y)F(x,y)$, which gives us the complex field $F(x,y)$ from the object after dividing by $R^*(x,y)$. With an offset reference beam, that desired term can be obtained by (1) Fourier transforming the detected intensity, (2) using a window function that selects the third term (which would be an image of the object if the image plane were in the far field with respect to the detector plane) and zeroing out the first, second, and fourth undesired terms, and then (3) inverse Fourier transforming to arrive at the filtered field in the detector plane, $G_f(x,y)$, a noisy version of $R^*(x,y)F(x,y)$.

The Fourier transform of the noise term, $N_{01,4}(x,y)$, is uniformly distributed across the entire digital array, whereas the Fourier transform of the desired term, being an image or image-like, is concentrated in a smaller area of the array. If g_c is the ratio of the area of the entire digital array to the smaller extracted area, then the total noise power will be reduced by a factor of g_c, whereas the signal is not reduced because the window function is chosen to include the entire signal term. By Parseval's theorem, the total noise power in the filtered data plane is equal to $1/g_c$ times the original noise power; hence the variance of the noise term is reduced by that same factor of g_c, and that factor is the compression gain of the system (the signal is compressed in area by that factor when performing the first Fourier transform, but the noise was not compressed). Hence the filtered signal is

$$G_f(x,y) = R^*(x,y)F(x,y) + \left(\frac{|R(x,y)|}{\sqrt{2g_c}}\right) N_{c01,1}(x,y) \ . \tag{2.7}$$

where $N_{c01,1}(u,v)$ is zero-mean, uniformly distributed circular complex Gaussian noise, which has unity variance for both its real and imaginary parts (which accounts for the $\sqrt{2}$ factor in the denominator). This arises because the original, real-valued noise in the measured data is band-pass filtered making it complex valued. In the special case of a Fourier transform hologram, the desired term in the Fourier transform of the hologram is an image. Then the filtering step is not needed *per se* if we merely observe the field over the support of the object. Then without any explicit filtering we get the same noise reduction benefit because the signal is contained within the support of the object while the noise is spread uniformly over the entire array.

The SNR of the filtered data is

$$SNR(x,y) = \frac{\left|R^*(x,y)F(x,y)\right|}{\sqrt{\mathrm{Var}\left[\left(\frac{|R(x,y)|}{\sqrt{2g_c}}\right) N_{c01,1}(x,y)\right]}} = \sqrt{g_c}\,|F(x,y)|. \tag{2.8}$$

where $|F(x,y)|^2$ is the number of photons from the object striking the detector. The $\sqrt{2}$ factor drops out because the variance of $N_{c01,1}$ is 2.

The important conclusion from Eq. (2.8) for the bright reference case is that the SNR depends only on the number of photons from the object and on the compression gain and is independent of all the other noise sources (photons noise in the reference, read noise, quantization noise, etc.) and independent of the strength of the bright reference. This is the well-known heterodyne noise advantage [4]. Also, in the weak-signal case, even though $\left|F\left(x,y\right)\right|^2$ may be very small — less than 1 e^-/pix on average, if the compression gain is large enough, then the image can still have a useful SNR. The effect of the compression gain on the SNR of digital holography can be very significant. For the off-axis holography scenario where the entire object signal covers half of the Fourier plane, the minimum compression gain is $g_C = 2$. The maximum compression gain scenario occurs when a uniformly distributed object field in the detector plane is concentrated to a single point spread function in the image plane. In this case, the compression gain is given by

$$g_C = \frac{\left[\left(\lambda z\right)/\Delta x\right]^2}{\left[\left(\lambda z\right)/D\right]^2} = \left(\frac{D}{\Delta x}\right)^2 \tag{2.9}$$

where the numerator in the middle expression is the area of the Fourier transform of the detected field while the denominator represents the area of the width of the main lobe a sinc function due to the finite dimensions of the detector with a width D and a pixel pitch of Δx. For example, if D = 1 cm and Δx = 7 μm, the maximum compression gain would be $g_C = 2\times10^6$.

2.3. Simulation: Weak-Signal Holographic Forward Model

We seek to simulate a weak-object digital holography experiment in the computer by taking into account as many of the effects found in a physical system as possible. Realistic parameters for the object intensity, read noise and quantization noise will be used to simulate a physical system. The reference field was a pure-phase, off-axis plane wave with an array size of 1024 x 1024 pixels. To simulate a rough object that would yield a speckled image, the field $f(\xi,\eta)$ at the object was created by multiplying the square root of a 412 x 412 pixel incoherent image intensity, $I_{inc}(\xi,\eta)$, by a circular-complex Gaussian random variable, $N_{c\mu,\sigma^2}$ having a mean μ and a variance σ^2, with

$$f(\xi,\eta) = N_{c0,0.5}\sqrt{I_{inc}(\xi,\eta)}. \tag{2.10}$$

The object was embedded in a 1024 x 1024 array. The combined signal of the reference and object beams was scaled to have a total of 80% of the full well depth, or 32,000 e^-. In Eq. (2.1), the measured intensity in the detector (hologram) plane was calculated as

$$H_n(x,y) = Poisson\left[\left|R(x,y)+F(x,y)\right|^2\right] + \sigma_r N_{0,1}(x,y) \tag{2.11}$$

where σ_r is the rms read noise, all in units of photo-electrons. We modeled our detector as a 12-bit camera. The detector conversion gain factor was calculated as $40,000\ e^- / \left(2^{12}\ \text{DN}\right) = 40,000\ e^- / (4096\ \text{DN}) = 9.76\ e^- / \text{DN}$ where DN stands for

digital number. The digital numbers were rounded to the nearest integer, that is, quantized to 12 bits (0 to 4095) to simulate quantization noise of a physical detector. In what follows, however, we will quote the output of the camera in units of photoelectrons.

In this work, we chose to vary the object signal strength in order to evaluate the effect of a weak object on image reconstruction. The average total signal was $\langle H(x,y)\rangle = \left\langle \left| R(x,y) + F(x,y) \right|^2 \right\rangle = 32{,}000\, e^-$ where $\langle \cdot \rangle$ represents the mean over all the pixels, with a read noise having σ_r = 16 e^-, which is typical for a medium-quality scientific camera. As we varied the object signal, the reference signal was also adjusted to maintain an 80% well-depth of the camera. We conducted thirteen different trials, with the mean object intensity, $|F|^2$ set at 0.01, 0.02, 0.05, 0.1, 0.2, 0.5, 1, 2, 5, 10, 20, 50 and 100 e^-/pixel.

2.4. Simulation: Weak-Signal Holographic Image Reconstruction

To reconstruct an object signal, the detected holographic data of Eq. (2.1) is Fourier transformed, to reveal a spatially separated image term, twin image term, and the autocorrelations of the reference and object terms. Since we had an extremely strong reference signal compared with the object signal, the autocorrelation of the object term was highly suppressed. A mask of 412 x 412 pixels with a raised-cosine edge was applied to the image term to isolate this component from the additional holography on-axis reference beam term. For this simulation, the compression gain

was g_c = 6.2, found by calculating the ratio of the area of the Fourier transform of the detector field (412 x 412 pixels) to the total area of the detector (1024 x 1024 pixels). This reduces the noise power by this factor, relative to the signal power, for the recovered image. We Fourier transformed the object field to obtain $R^*(x,y)F(x,y)$ and divided by $R^*(x,y)$ to obtain the field, $F(x,y)$, in the plane of the detector.

To objectively and quantitatively monitor the quality of the reconstructed image as the object signal is reduced, we used an absolute error metric [5]

$$E^2 = \min_{\alpha,\xi_0,\eta_0} \left\{ \frac{\sum_{\xi,\eta} \left| \alpha I(\xi-\xi_0,\eta-\eta_0) - I_{ideal}(\xi,\eta) \right|^2}{\sum_{\xi,\eta} \left| I_{ideal}(\xi,\eta) \right|^2} \right\} \tag{2.12}$$

where $I(\xi,\eta)$ is intensity of the reconstructed image, $I_{ideal}(\xi,\eta)$ is the intensity of the ideal, noise-free image, α is a possibly unknown multiplicative constant and ξ_0 and η_0 adjust for any image translations. The calculation of the error metric includes minimization over the three unknown parameters α, ξ_0 and η_0. A smaller E^2 value signifies a lower image error, and hence a better agreement with the ideal image. This metric is valid under the condition that the reconstructed image is an estimate of the ideal image. In addition, we also calculated the power signal-to-noise ratio of the recovered image,

$$SNR_I = \frac{\left\langle I_{ideal}(\xi,\eta)\right\rangle}{\left\langle \left[I_{ideal}(\xi,\eta) - I(\xi,\eta)\right]^2 \right\rangle^{1/2}}. \tag{2.13}$$

where $\langle\cdot\rangle$ represents the mean over all the pixels. A larger value of SNR_I indicates a higher quality image.

2.5. Simulation: Weak-Signal Holography Results

Table 2-1 summarizes the quantitative measurements of the forward model and image reconstruction as the object signal in the detector plane, $\left|F(x,y)\right|^2$, is reduced to well below one e^-/pixel. Figure 2-1 shows the reconstructed images in the presence of noise. Although the absolute error metric increased as the signal was reduced, the image is visually recognizable for object intensities down to 0.05 e^-/pix. The object used in the simulation had high contrast; the image quality would be less for a low-contrast object. These results show that single-shot off-axis digital holography can be used to successfully recover recognizable images of extended objects with extremely weak object signals, down to 0.05 e^-/pix at the detector.

2.6. Laboratory Experiment: Calibration and Experimental Setup

In addition to simulation work, we performed a laboratory digital holography experiment which demonstrates the ability to recover images for a very weak average signal from the object. Careful calibration of our Retiga 2000R Q-Imaging CCD detector (1200 x 1600 pixels, pixel pitch of 7.4 μm) was performed to ensure accurate measurements. Specifically, to convert the digital output of the 12-bit (0… 4095

Table 2-1. Image signal-to-noise ratio and absolute error metric of the reconstructed image for varying object signal levels.

Object Signal [e^-/pix]	**SNR$_I$**	***E***
100	523.6	0.03
50	274.9	0.05
20	110.0	0.08
10	55.0	0.12
5	27.5	0.17
2	11.0	0.26
1	5.50	0.35
0.5	2.75	0.46
0.2	1.10	0.62
0.1	0.55	0.72
0.05	0.28	0.79
0.02	0.11	0.85
0.01	0.06	0.87

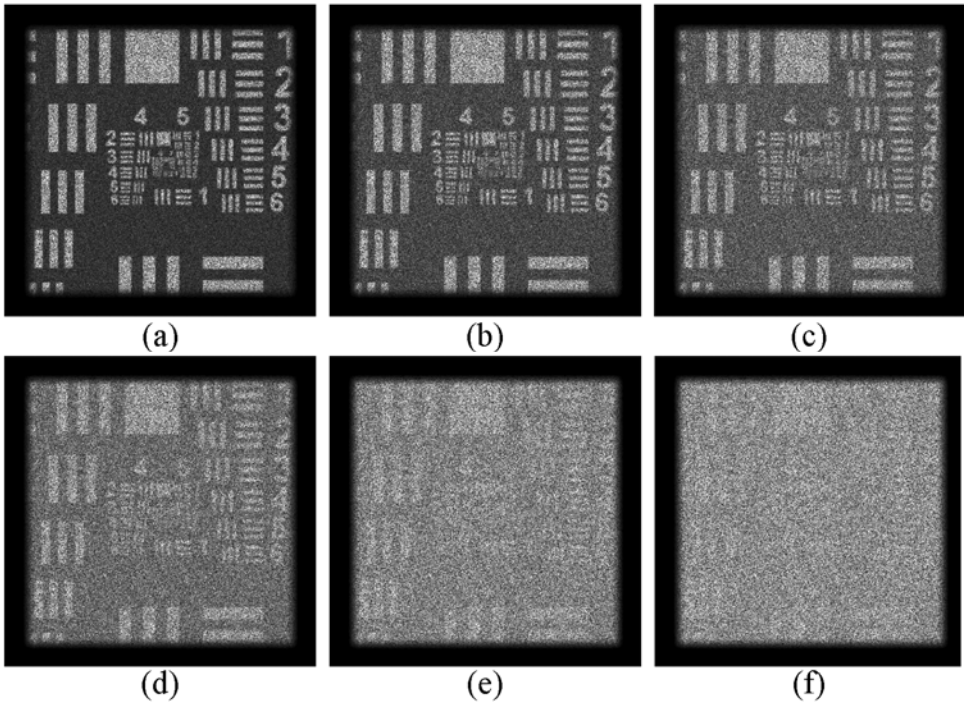

Figure 2-1. Amplitude image reconstructions for weak objects in the presence of noise; images are thresholded to 60% of maximum. Object beam mean photoelectrons per pixel of (a) 0.5 e^-, (b) 0.2 e^-, (c) 0.1 e^-, (d) 0.05 e^- (e) 0.02 e^-, and (f) 0.01 e^-. SNR and absolute error metric for each image are shown in Table 2-1.

digital numbers) camera to photoelectrons, the camera gain factor was found by calculating the slope of the variance of the total noise with respect to the average signal intensity [6] for a uniform field. Fixed-pattern noise was removed by subtracting two successively detected similar images from each other at each signal level (effectively removing the pixel-to-pixel variation in the sensitivity of the CCD) prior to calculating the variance, giving a linear slope for the gain. The gain was found to be 9.1 e^-/count. This compares reasonably well with the theoretical gain of 9.7 e^-/count based on the nominal full well of 40,000 e^- and 12-bit quantization. To determine the read noise of our camera, we acquired eighty dark frames and computed their statistics. The read noise was calculated from the collection of these frames by 1) averaging all eighty frames together on a pixel-to-pixel basis to compute the average dark frame and then 2) finding the spatial mean and standard deviation of the average dark frame. This method resulted in a mean of 14.95 e^- and a standard deviation of 0.26 e^- for the dark frame. The mean of 14.95 e^- agreed well with the camera specifications for read noise of 16 e^- rms.

A low-light experiment was conducted using the setup shown in Figure 2-2. An Ar+ laser operating at 514 nm was used as an illumination source. Mechanical shutters were placed in both beam paths such that three frames — reference-only, object-only and hologram frames — could easily be acquired in succession. The object consisted of nine 7.9 mm diameter ball bearings mounted on a black, low–reflectance felt cloth. The camera was located 2.09 m from the object. A neutral density (ND) filter wheel was placed in the object arm of the beam path, such that the illumination of the object could be adjusted in discrete

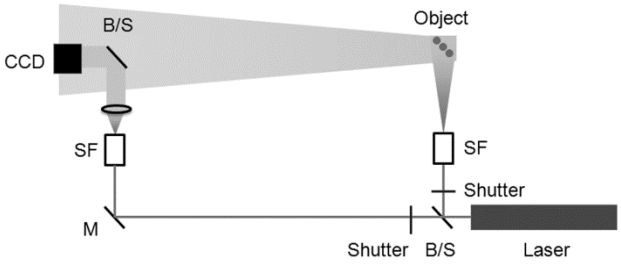

Figure 2-2. Experimental setup used for a low-light digital holography experiment.

increments. The exposure time for the hologram frames was set at 650 μs, to allow for an exposure that was approximately 80% of the full well depth (40,000 e^-) for an optical density (OD) of zero.

The detection of object-only frames allows one to calculate the average number of photoelectrons per pixel. A total of 10 object-only frames for each ND filter wheel setting were acquired (to allow for statistical averaging to better determine the signal level); the exposure time was the same as that of the hologram frames. The object-only photoelectrons per pixel were calculated by 1) subtracting the average dark frame from each individual frame, 2) averaging over all the pixels in the frame, and 3) calculating the average e^-/pix among the 10 frame ensemble. For an OD of 0, the average photoelectrons per pixel was 5.13; corresponding values at higher optical densities can be derived from the expected intensity transmittance, $T = 10^{-OD}$, through each ND filter. As the signal strength decreases, measurements below 0.26 e^- fall within the standard deviation of the noise floor of the system and are therefore less accurate by direct measurement.

2.7. Laboratory Experiment: Results

The ability to obtain a recognizable SNR image despite a very low signal level can be seen by the fidelity of the image reconstructions. A single frame was used to recover an image from the detected holographic data. We excluded the first 400 pixels in the vertical detector in order to allow for square arrays 1200 x 1200 pixels in size. Images were extracted from the detected frames using a standard holographic procedure. The detected interference frame was first Fourier transformed. In the spatial frequency domain, a flat-top function 150 pixels in width with a raised-cosine edge of 24 pixels allowed for the spatial frequency content of the image term to be isolated from the additional holographic terms and extracted. The desired term was then inverse Fourier transformed back to the spatial domain of the detector plane. The recovered extracted holographic term, $F(x,y)R^{*}(x,y)$ was then divided by $|R(x,y)|$ (a constant), the reference-only magnitude, to scale the field appropriately. To avoid digital wrap-around problems when propagating, the resulting data was zero–padded in an array four times larger. The complex object field was then propagated to the image plane using angular spectrum propagation.

Figure 2-3 shows the image reconstructions from the holograms of the nine ball bearings for six different object signals strengths in a 2608 x 2371 pixel subset of the entire image. Figure 2-4 is a zoom–in (500 x 500 pixels) of the middle ball bearing in the 3 x 3 array of ball bearings. As clearly seen in Figure 2-4(a), not only is the tight focus of the ball bearing point source recovered, but we also see clear evidence of

sinc sidelobes resulting from the square detector aperture. As the OD of the neutral density filter is increased, the weak sidelobes of the sinc function become buried in the noise, although the main lobe is maintained. The signal is finally overcome by the noise for OD = 3.2. Since OD = 0 corresponded to 5.13 e^-/pix from the object at the detector, OD = 3.1, for which the ball bearing peak was just barely visible, corresponds to only 4×10^{-3} e^-/pix. Due to a difference in compression gain factors between our results in simulation and experiment (increased compression gain in the experimental case), we were able to observe images with a 10X reduction in average photoelectron/pixel as compared with the digital simulations.

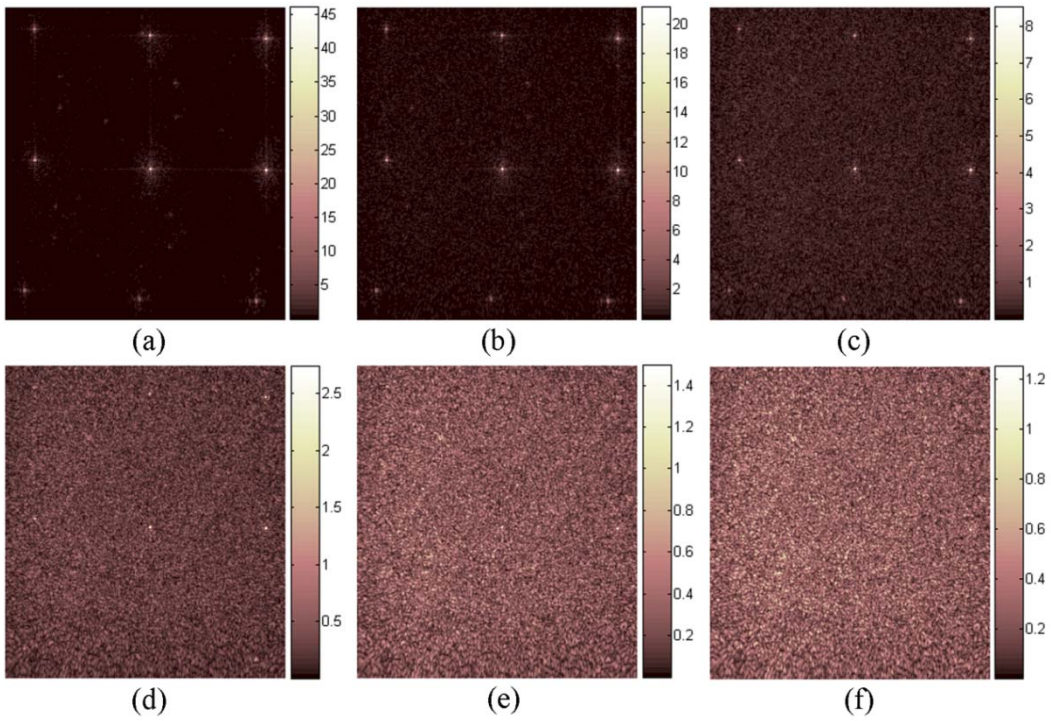

Figure 2-3. Image reconstructions for nine ball bearings with ND filter equal to (a) 0.0 OD, (b) 0.8 OD, (c) 1.6 OD, (d) 2.4 OD, (e) 3.1 OD, and (f) 3.2 OD. Scale is in photoelectrons.

These experimental results demonstrate the ability to recover recognizable images, even within a very weak-signal detection regime, using only one holographic frame. The average photoelectron/pixel calculations, in combination with the recovered imagery, support the theoretical heterodyne advantage that the SNR for a weak-object signal depends solely on magnitude of the object signal and the compression gain of the image. Images with highly concentrated signals will be more easily recoverable under the weak-signal conditions.

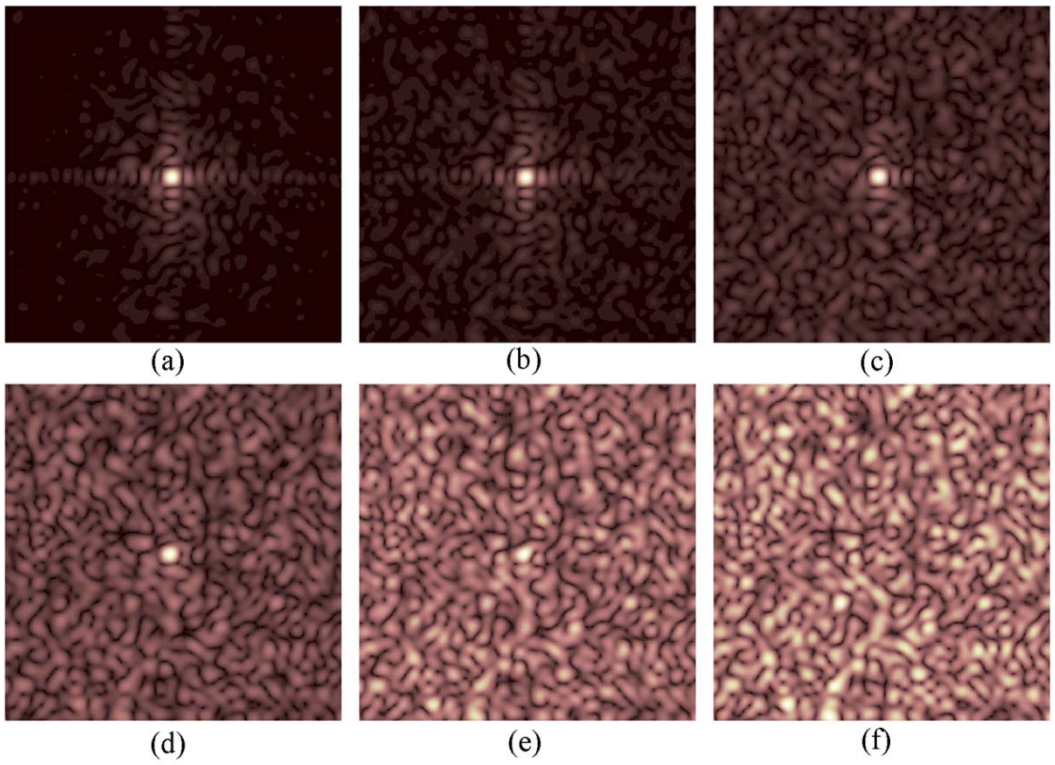

Figure 2-4. Zoom-in of central ball bearing for (a) 0.0 OD, (b) 0.8 OD, (c) 1.6 OD, (d) 2.4 OD, (e) 3.1 OD, and (f) 3.2 OD.

2.8. References

1. M. Gross and M. Atlan, "Digital holography with ultimate sensitivity," Optics Letters **32**, 909-911 (2007).

2. A. V. Oppenheim and R. W. Schafer, *Discrete-time signal processing,* (Prentice Hall, Englewood Cliffs, N.J., 1989).

3. P. S. Idell, "Resolution limits for high-resolution imaging lidar," Proc. SPIE **1416**, 250-259 (1991).

4. T. Takenaka, K. Tanaka, and O. Fukumitsu, "Signal-to-Noise Ratio in Optical Heterodyne-Detection for Gaussian Fields," Applied Optics **17**, 3466-3471 (1978).

5. J. R. Fienup, "Invariant error metrics for image reconstruction," Appl. Opt. **36**, 8352-8357 (1997).

6. J. R. Janesick, *Scientific charge-coupled devices,* (SPIE Press, Bellingham, Wash., 2001).

3. Imaging through Phase Screens: Simulation

3.1. Introduction

Imaging through multiple planes of optical aberrations occurs in a variety of scenarios such as atmospheric turbulence (particularly for horizontal paths) [1], biological tissue [2], other random media and space-variant optical systems. In this chapter we describe the use of sharpness metrics for correcting aberrations occurring in multiple planes. Sharpness metrics were first used for incoherent imaging through atmospheric turbulence using telescopes [3]. Following that work, several others have applied sharpness metrics to synthetic aperture radar problems [4-6]. Recent research has explored various sharpness metrics and their performance in digital holography [7]. In all these previous cases, the turbulence could be approximated by phase errors in one plane near the aperture of the telescope or detection plane, and the aberrations were space-invariant. Thurman and Fienup [8] demonstrated the correction of space-variant phase errors (the anisoplanatic case) caused by a single phase screen a distance from the aperture. We extend that work to incorporate correction of aberrations in multiple planes.

3.2. Forward model

3.2.1. Holography

For the process of simulating a digital hologram with discrete, thin phase screens, we followed the method outlined in [7, 8], and extend their work to a multiple screen scenario. A description on the aberrations modeled will be discussion in Section

3.2.3. In summary, a hologram is formed by recording the interference of two beams, the reference and object beams, $R(x,y)$ and $F(x,y)$, respectively, in the plane of the detector. First consider the ideal case without aberrations, and let the reference beam be a plane wave

$$R(x,y) = R_0(x,y)\exp[i(k_x x + k_y y)] \tag{3.1}$$

where $R_0(x,y)$ is the amplitude of the reference wave, k_x and k_y are the transverse components of the reference wavevector, and in the paraxial regime of interest in this chapter,

$$\begin{aligned} F(x,y) = \frac{1}{i\lambda z}\exp(ikz)\exp\left[\frac{i\pi}{\lambda z}\left(x^2+y^2\right)\right] \\ \times\int_{-\infty}^{\infty}\int_{-\infty}^{\infty} f(\xi,\eta)\exp\left[\frac{i\pi}{\lambda z}\left(\xi^2+\eta^2\right)\right]\exp\left[\frac{-i2\pi}{\lambda z}\left(x\xi+y\eta\right)\right]d\xi d\eta \end{aligned} \tag{3.2}$$

where λ is the wavelength of light, z is the longitudinal distance between the detector array and the object plane, and $f(\xi,\eta)$ is the optical field scattered by the object in the nominal object plane. The hologram intensity $H(x,y)$ at the detector plane can be written as

$$H(x,y) = \left|R(x,y) + F(x,y)\right|^2. \tag{3.3}$$

The 2-D spatial Fourier transform (FT) of Eq. (3.3) is given by

$$\begin{aligned} \tilde{H}(f_x,f_y) = \left|R_0\right|^2\delta(f_x,f_y) + \tilde{F}(f_x,f_y)\otimes\tilde{F}(f_x,f_y) \\ + R_0^*\tilde{F}\left(\frac{k_x}{2\pi}+f_x,\frac{k_y}{2\pi}+f_y\right) + R_0\tilde{F}^*\left(\frac{k_x}{2\pi}-f_x,\frac{k_y}{2\pi}-f_y\right) \end{aligned} \tag{3.4}$$

where $\tilde{H}(f_x, f_y)$ and $\tilde{F}(f_x, f_y)$ are the 2-D spatial Fourier transforms of $H(x, y)$ and $F(x, y)$, respectively, (f_x, f_y) are spatial frequency coordinates, $\delta(f_x, f_y)$ is a 2-D Dirac delta function and the second term is an autocorrelation denoted by $\otimes$. This is a special case of the general holography equation, originally described in Eq. (1.3). We will work in the regime such that $\left(k_x{}^2 + k_y{}^2\right)^{1/2}$ is sufficiently large that the third and fourth terms of Eq. (3.4) do not overlap the autocorrelation term. By windowing and inverse transforming the third term in Eq. (3.4), $F(x, y)$ can be determined to within a multiplicative constant and a translation. Alternatively, one may record three or more on-axis holograms with different constant phases associated with the reference beam, and reconstruct $F(x, y)$ by standard phase-shifting techniques. By inverting Eq. (3.2) we can compute an image of $f(\xi, \eta)$.

In this chapter, we simulate different speckle realizations of the fields, assuming an optically rough object. This can be implemented in a laboratory experiment by slightly rotating or translating the object between exposures such that the entire data collection time is short enough that the aberrations are fixed. In the computer, individual speckle realizations can be simulated by multiplying the square root of the object intensity by independent, zero-mean, circular complex Gaussian-distributed random numbers followed by low-pass filtering by the finite size of the detector array (the effective aperture). The speckle-reduced image intensity is then the average of the magnitude-squared image fields,

$$I(\xi,\eta) = \frac{1}{K}\sum_{k=1}^{K}\left|f_k(\xi,\eta)\right|^2 \tag{3.5}$$

where f_k is the k^{th} speckle realization of the image field and K is the number of speckle realizations.

3.2.2. Simulations with Finite Arrays

Aliasing may be present when propagating numerical fields in simulation due to the sampling and the finite array size. Appropriate measures must be taken to avoid non-physical energy resulting from wrap-around effects due to aliasing. Some authors choose to use intermediate absorption boundaries to address this problem [9]. We approach the issue by instead limiting the angular extent of the field reflected from the object. Light reflecting from a diffuse object scatters light over 2π steradians, but only a limited cone of the light reflected from the object hits the detector. As illustrated in Figure 3-1, the paraxial regime, the maximum angle of a ray from the object collected by the detector array can be approximated as:

$$\theta_{\max} \approx \tan\theta_{\max} = (D+w)/2z = \lambda f_c \tag{3.6}$$

where w is the object width, D is the detector width, z is the propagation distance, and f_c is the corresponding spatial frequency component of the object field sensed by the detector. To reduce the cone angle of the simulated scattered light, we choose to apply a mask in the Fourier domain to limit the spatial frequencies above f_c based on the maximum cone angle. However, for an off-axis point in the object, the speckle propagation will be symmetric, as shown in Figure 3-1 by the outermost rays $\pm\theta_{\max}$.

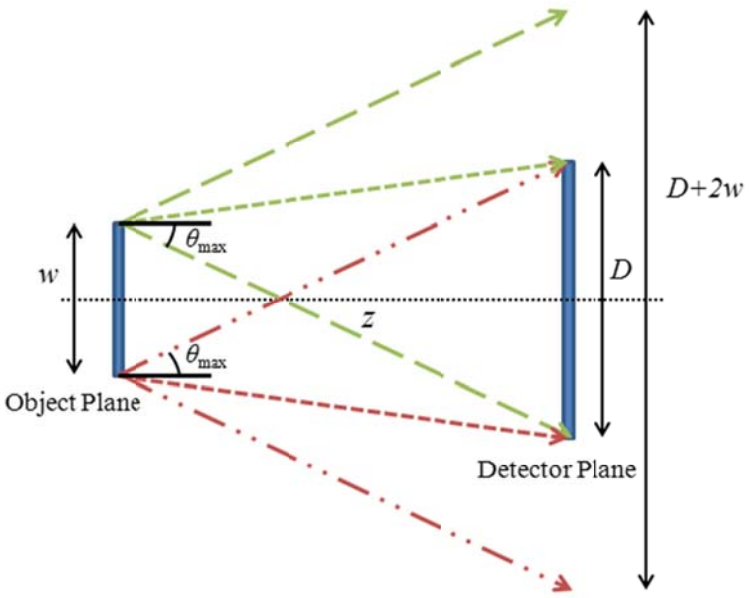

Figure 3-1. Finite array scattering angle geometry for propagating from the object plane to the detector plane.

Therefore, in order to avoid wrap-around effects of the cone of angles $[-\theta_{\max}, \theta_{\max}]$ across the extended object, we maintained a total array size $N\Delta x$ = (D+$2w$), during both forward propagation (object to detector plane) and back propagation (detector plane to image). By allowing for a numerical array with these specified dimensions, all points of the extended object had contributions to the speckle pattern throughout the detector plane. In order to implement this digitally, we started with an N x N array in the object plane, Fourier transformed it, and multiplied the Fourier transform by a windowing function to zero out spatial frequencies significantly above f_c. A raised-cosine-tapered weighting function was used to minimize ringing effects. Finally, we Fourier transformed the data back to the spatial domain; we consider this

bandlimited version of the object to be our ideal object. This method of simulating an object with light from it propagating over a limited angular extent proved to be a valid approach to overcome problems of aliasing often seen in digital simulations.

3.2.3. Phase Screens

We consider a holography case for which there is a volume of phase errors between the object and the hologram plane. The holography setup and optical propagation paths are depicted in Figure 3-2. We model the volume of phase errors using discrete phase screens, which has been shown to be approximately statistically equivalent to true volume turbulence [1, 10]. The modeled phase errors were created using polynomial approximations to the appropriate Kolmogorov atmospheric statistics [11]; further specifics of the model will be discussed in Section 3.3.1. For the present discussion, we examine the case in which the phase errors are located solely in the object beam path, and the reference beam is ideal. We ignored aberrations in the beam illuminating the object since the object will impose a random phase on the illuminating beam. For the simulations shown here, we first propagated the object field to the first phase screen using Fresnel propagation. With minor modifications, this approach can accommodate turbulence over the entire path of the object. We assumed that the additional planes of phase errors and the detector are relatively close to one another, and we wished the transverse sample spacing to remain the same (after the first propagation), so we implemented the propagation between phase screens using angular spectrum propagation, given in the paraxial regime as

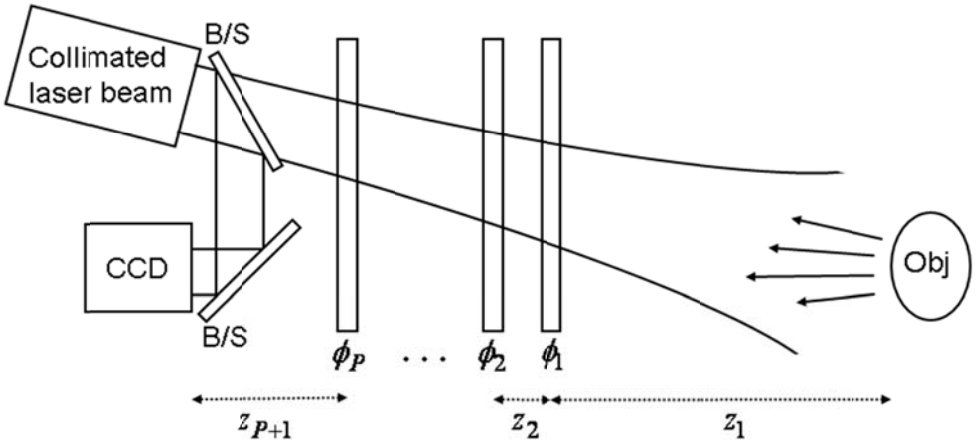

Figure 3-2. Layout for recording a digital hologram with multiple planes of phase error present.

$$\mathcal{A}\left[z; g(x,y)\right] = FT^{-1}\left\{FT\left[g(x,y)\right]\exp\left[-i\pi\lambda z\left(f_x^2 + f_y^2\right)\right]\right\} \tag{3.7}$$

for an arbitrary field $g(x,y)$ that is propagated a distance z, where we have ignored inconsequential constants and *FT* represent a Fourier transform.

The distance from the object plane to the first plane of phase errors is denoted by z_1, z_p is the distance from the $(p-1)^{th}$ phase plane to the p^{th} phase plane, ϕ_p is the phase error for the p^{th} plane, *P* is the number of phase screens and $G_k(x,y)$ is the aberrated field in the hologram plane for the k^{th} speckle realization of the object. To simplify later notation, we define a forward propagator

$$\begin{aligned}\mathcal{P}_{0\to p^-}\left[f_k(\xi,\eta)\right] = \mathcal{A}\Big\{z_p; \exp\left(i\phi_{p-1}\right)\cdots \\ \mathcal{A}\Big[z_3; \exp\left(i\phi_2\right)\mathcal{A}\left\{z_2; \exp\left(i\phi_1\right)\mathcal{F}_r\left[z_1; f_k(\xi,\eta)\right]\right\}\Big]\Big\}\end{aligned} \tag{3.8}$$

where $\mathcal{F}_r\left[z_1; f_k(\xi,\eta)\right]$ is a Fresnel transform of the object field propagated a distance z_1 to the first phase screen. The inverse propagator from the hologram plane in the direction of the object plane can be written in a similar fashion:

$$\begin{aligned}\mathcal{P}^{\dagger}_{P+1\to p^+}\left[G_k(x,y)\right] = \exp\left(-i\phi_p\right)\mathcal{A}\Big\{-z_{p+1};\exp\left(-i\phi_{p+1}\right)\cdots\exp\left(-i\phi_{P-1}\right)\\ \times\mathcal{A}\left[-z_P;\exp\left(-i\phi_P\right)\mathcal{A}\left\{-z_{P+1};G_k(x,y)\right\}\right]\Big\}\end{aligned} \tag{3.9}$$

where the z_p are considered to be positive numbers for propagations in both directions.

Using the above definitions, the aberrated field in the hologram plane can be written in terms of the object field as

$$G_k(x,y) = \mathcal{P}_{0\to P+1}\left[f_k(\xi,\eta)\right]. \tag{3.10}$$

Likewise, using the inverse propagator, the input field is

$$f_k(\xi,\eta) = \mathcal{P}^{\dagger}_{P+1\to 0}\left[G_k(x,y)\right], \tag{3.11}$$

where for simplicity of notation we are ignoring the finite extent of the recorded hologram in the equation above.

3.3. Aberration Correction

To estimate and correct for the phase errors present in the object-beam propagation path, we maximize the sharpness metric

$$S = \sum_{\xi,\eta} I^{\beta}(\xi,\eta) - \alpha\sum_{k=1}^{K}\sum_{f_\xi,f_\eta} W(f_\xi,f_\eta)\left|\tilde{F}_k(f_\xi,f_\eta)\right|^2 \tag{3.12}$$

as a function of phase estimates, where α is a constant, K is the number of speckle images, $\tilde{F}_k(f_\xi, f_\eta)$ is the Fourier transform of the k^{th} speckle realization of the field in the image plane, and $W(f_\xi, f_\eta)$ is a weighting function that defines the spatial frequency content of the object fields that are sensed over the area of the digital hologram. The first term is a standard sharpness metric, as originally introduced in Eq. (1.4). If $\beta > 1$, we seek to maximize the value of the sharpness metric, or conversely, if $\beta < 1$, we seek to minimize the value of the sharpness metric (which maximizes the sharpness of the image). The second term penalizes frequency content of the image field that could not have come from the digital hologram through reasonable atmospheric turbulence; it mitigates against the creation of such non-physical phase screens. We chose to constrain the Fourier domain, since the frequency content of the object will remain approximately constant throughout the propagation distance, even in the presence of reasonably large turbulence.

We used a conjugate-gradient routine to maximize the sharpness metric as a function of estimates of the values of phase screens. The partial derivative of S with respect to the value of phase screen p at location (x_0, y_0) is given by

$$\frac{\partial S}{\partial \phi_p(x_0, y_0)} = \frac{\partial}{\partial \phi_p(x_0, y_0)} \left[\sum_{\xi,\eta} I^\beta(\xi,\eta) - \alpha \sum_{k=1}^{K} \sum_{f_\xi, f_\eta} W(f_\xi, f_\eta) \left| \tilde{F}_k(f_\xi, f_\eta) \right|^2 \right]. \quad (3.13)$$

In a fashion similar to [[12], Eq. (41)], this can be written in terms of the object and hologram fields in the following form:

$$\frac{\partial S}{\partial \phi_p(x_0,y_0)} = \frac{2\beta}{K}\sum_{k=1}^{K}\mathrm{Im}\left[\mathcal{P}^{\dagger}_{P+1\to p^+}\left[G_k(x,y)\right]\left\{\mathcal{P}_{0\to p^-}\left[I^{\beta-1}(\xi,\eta)f_k(\xi,\eta)\right]\right\}^*\right]$$
$$+2\alpha\sum_{k=1}^{K}\mathrm{Im}\left[\mathcal{P}^{\dagger}_{P+1\to p^+}\left[G_k(x,y)\right]\mathcal{P}_{0\to p^-}\left\{FT^{-1}\left[W(f_\xi,f_\eta)\tilde{F}_k(f_\xi,f_\eta)\right]\right\}^*\right]. \quad (3.14)$$

This allows efficient calculation of the entire gradient of the sharpness metric. The derivations for these expressions are given in Appendix A in Section 3.6.

We chose to model the atmospheric phase using polynomial phase estimates,

$$\phi_p(x_p,y_p) = \sum_j c_{p,j}\psi_j(x_p,y_p) \quad (3.15)$$

where j is the index for the basis function, $c_{p,j}$ are the expansion coefficients and $\psi_j(x_p,y_p)$ is the basis function. We optimized over the coefficients $c_{p,j}$ for which the partial derivatives are

$$\frac{dS}{dc_{p,j}} = \sum_{x_p,y_p}\frac{\partial\phi_p(x_p,y_p)}{\partial c_{p,j}}\frac{dS}{d\phi_p(x_p,y_p)} = \sum_{x,y}\psi_j(x_p,y_p)\frac{\partial S}{\partial\phi_p(x_p,y_p)} \quad (3.16)$$

from which we see that the gradients with respect to the polynomial coefficient $c_{p,j}$ can be found by taking the inner product of Eq. (3.14) with the basis function. The basis functions used in this work were Zernike-like polynomial functions orthonormalized over a rectangular pupil. Our starting guess for each coefficient was zero. We then performed five conjugate gradient (CG) iterations of the 3rd order polynomials terms, five more iterations adding 4th order terms and repeated five more

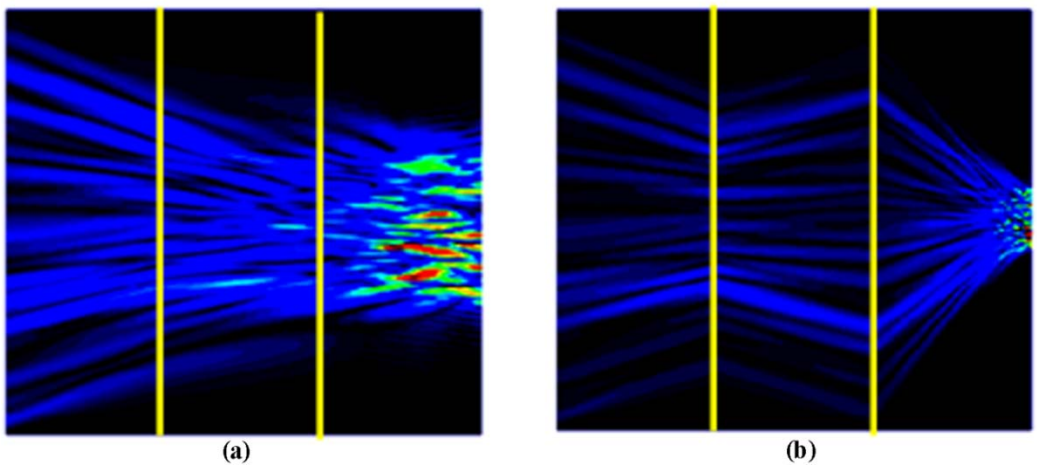

Figure 3-3. Speckle propagation as seen from horizontal slice of field magnitude versus *z*-axis from the detector plane (left-hand side) to image plane (right-hand side). (a) ideal propagation, and (b) propagation with phase screens oversharpening by forming an effective telescope. Yellow bars are the locations of the phase screens.

CG iterations for each additional higher order term up to the 15th order polynomial terms, similar to what was done in [7].

We illustrate the importance of including the second term in Eq. (3.12) to mitigate against oversharpening effects in Figure 3-3 which shows an *x*-*z* slice of the propagation path; speckles are elongated in the *z*-direction while following a propagation path between the detector plane and image plane, as shown in Figure 3-3. However, when reconstructing for estimates of two or more phase screens using a basic $I^{\beta}(\xi,\eta)$ sharpness metric, where β is a constant, we encountered a new form of oversharpening. The reconstructed phase screens developed large quadratic (focusing) terms, such that each phase screen acts like a lens, as shown in Figure 3-3(b). In the two phase screen case, the phase screen closest to the detector ϕ_2 acts like a negative lens, and the screen closest to the object ϕ_1 acts like a positive lens.

The combined phases of the phase screens become an effective demagnifying telescope. This demagnified version of the image had a larger computed sharpness value than the true image, as would be expected since the image is concentrated in a smaller area and the intensities within that area are increased.

The mask function $W(f_\xi, f_\eta)$ was created by first thresholding the amplitude of the Fourier transform of the field in the detector plane in the area where the majority of the energy was concentrated (for this example, we empirically chose 0.25 times the maximum amplitude as the threshold level); the side lobe energy was truncated. We then found the smallest square that contained the entire thresholded amplitude. $W(f_\xi, f_\eta)$ was set to unity outside the square and zero inside the square, except for a gradual transition between these two regions with the use of a raised cosine function. By multiplying this mask function by the squared-magnitude of the Fourier transform of the field in the image plane, the metric effectively penalizes the solution if the computed bandwidth of the fields increases. We tried several values for α and chose the one that worked best; this value will change with the parameters of the scenario. Speckle propagation results with this approach are shown in Section 3.4.2.

3.3.1. Simulation Parameters

To avoid aliasing and warp-around effect in our digital simulation, we limited the angular extent of the field propagated from the object by cropping out higher spatial frequencies but left the angular extent wide enough to illuminate an area larger than

the detector as described earlier. The spatial frequency content of the image is determined by considering the pixel pitch of the detector Δx, the total array size N, distance of propagation z, and the laser illumination wavelength λ, as described in Section 3.2.2. We employed $K = 24$ speckle realizations.

The aberrations were assumed to be constant during the collection of all the speckle realizations. The phase screens used in the simulation were 15^{th}-order polynomial approximations for Kolmogorov atmospheric phase screens [11]. The effective D/r_0 [13] of the phase screens was 10. The phase screens were spaced equidistant through the propagation distance.

We performed two sets of noiseless simulations and image reconstructions with different images and slight variations in parameters values. In Ref. [7], the sharpness metric of Eq. (3.12) with β = 1.01 was shown to have favorable performance for the simulated object, the aerial photograph of the Presidio used here and in the previous study. In Case 1, a speckled version of the Presidio shown in Figure 3-4(a) was imaged with the simulation parameters $N = 256$, $D = N\Delta x = 16$ cm, $\lambda = 514$ nm, and the total distance was $z = 100$ m. We used $\alpha = 0$ in the sharpening algorithm. We examined both two-screen and three-screen simulations. For the two-screen simulation (Case 1A), $z_1 = z_2 = 50$ m while for the three-screen simulation (Case 1B) $z_1 = z_2 = z_3 = 33.3$ m. For Case 2, the image was the model of a car and the system parameters were the same; $N = 256$, $D = N\Delta x = 16$ cm, $\lambda = 514$ nm, but the total distance was $z = 500$ m. For the two-screen simulation, $z_1 = z_2 = 250$ m

while for the three-screen simulation $z_1 = z_2 = z_3 = 166.7$ m. By testing a few different values for the scaling constant α, $\alpha = 5\text{x}10^{-8}$ was chosen for the sharpness metric in Case 2. By picking $\alpha = 5\text{x}10^{-8}$, enough weight was added to the metric to avoid demagnifying the image but simultaneously did not overpower the I^{β} term which would cause stagnation of the optimization.

3.4. Results

3.4.1. Case 1

The ability to successfully reconstruct images by using our sharpness algorithm technique for multiple planes for Case 1 is shown in Figure 3-4 and Figure 3-5. Figure 3-4(b) and Figure 3-5(b) show the image when the phase screens are present in the system without correction. For both the two- and three-screen cases, the aberrated image is a poor visual representation of the ideal image shown in Figure 3-4(a) and Figure 3-5(b). However, once we have estimated the phase screens using the procedure described in Section 3.3 and used the phase estimates to reconstruct an image, we obtained images having a dramatic improvement in quality for both the two- and three-screen cases, shown in Figure 3-4(c) and Figure 3-5(c), respectively, although the image quality in the case of three phase screens is less than ideal.

To quantify the results of our phase-error correction, we computed the absolute error, *E*, of the reconstructed image with respect to the ideal image, given by [14, 15]

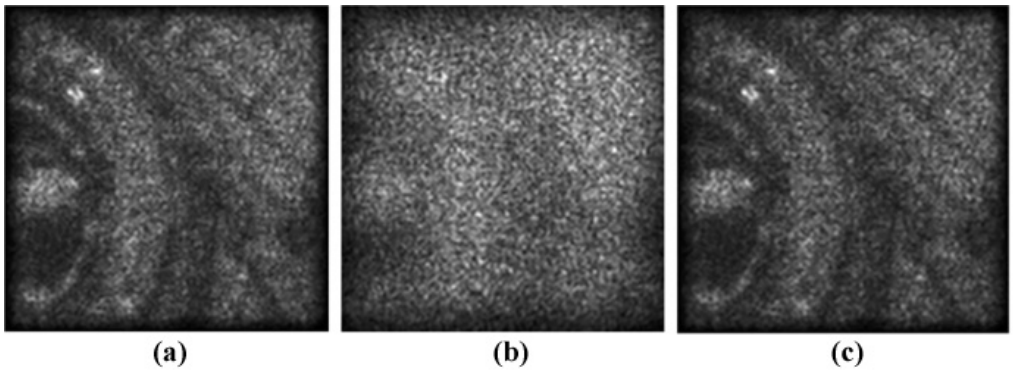

Figure 3-4. Results for the two-screen simulation (Case 1A). (a) The ideal image, (b) the image when there is no aberration correction, (c) the image when the phase was estimated and used in the reconstruction.

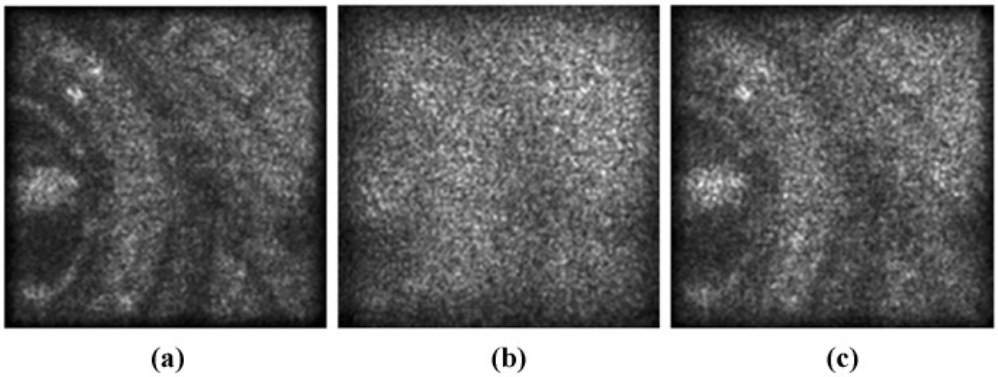

Figure 3-5. Results for the three-screen case (Case 1B). (a) The ideal image, (b) the aberrated image and (c) the image reconstructed with phase estimates.

$$E^2 = \min_{\xi_0,\eta_0} \left\{ \frac{\sum_{\xi,\eta} \left| I(\xi - \xi_0, \eta - \eta_0) - I_{ideal}(\xi,\eta) \right|^2}{\sum_{\xi,\eta} \left| I_{ideal}(\xi,\eta) \right|^2} \right\} \tag{3.17}$$

where $I(\xi,\eta)$ is the intensity of the reconstructed image and $I_{ideal}(\xi,\eta)$ is the intensity of the ideal image, the image computed from the field at the aperture without phase errors. This error metric gives us an indication of the quality of a reconstructed image with a lower number corresponding to better image quality. For

the uncorrected, aberrated images, the absolute error was 0.3264 for the two-screen case and 0.3311 for the three-screen case. Upon reconstruction, the absolute error improved to 0.0813 and 0.0946 for cases of two and three screens, respectively. In general, the value of the absolute error metric depends on multiple parameters including number of speckle realizations, type and contrast of the object, distances between phase screens, locations of phase screens with respect to the object location and aperture location, magnitude of the aberrating phase, and signal-to-noise ratio. Figure 3-6(c) and (d) and Figure 3-7(d) – (f) show the corresponding phase estimates found through this nonlinear conjugate gradient sharpness maximization technique. The agreement is very good for the case of two phase screens and reasonably good for the case of three phase screens. Comparison of an individual phase screen

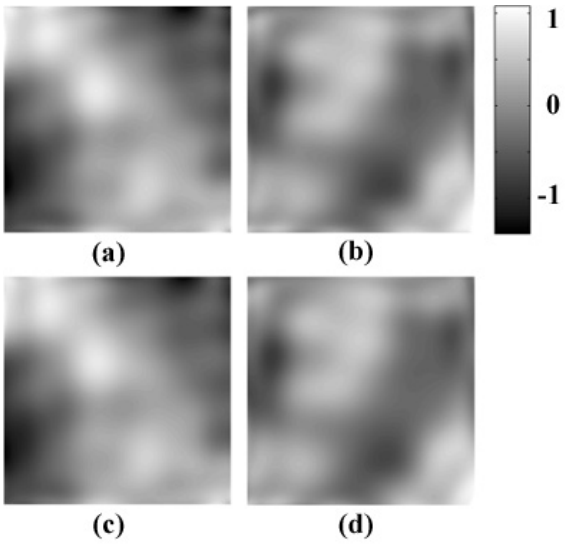

Figure 3-6. Phases for the two-screen simulation. Simulated true phase for (a) plane 1 and (b) plane 2. 15th order polynomial phase estimates found through image sharpening technique for (c) plane 1 and (d) plane 2. The scale is given in units of waves.

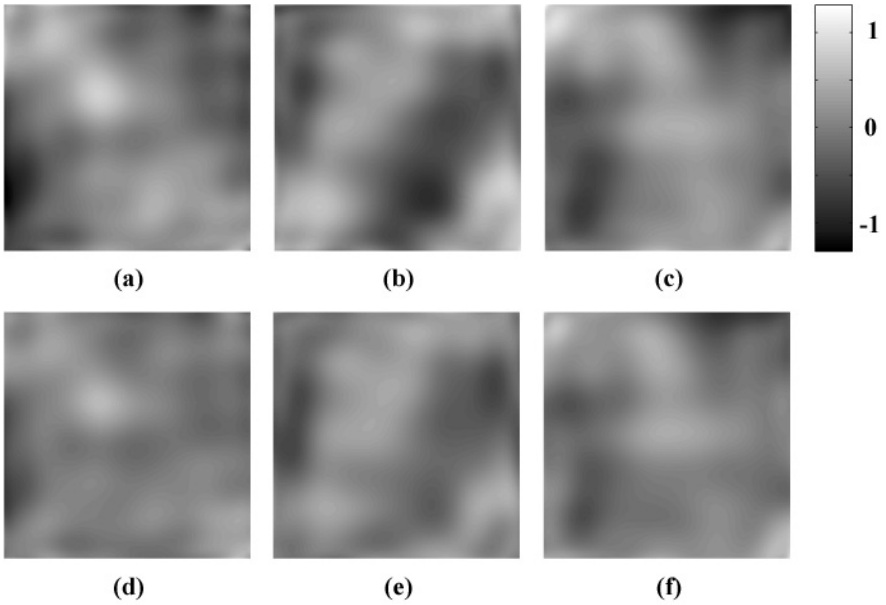

Figure 3-7. Phases for the three-screen simulation. (a – c) The simulated true aberrations. (d – f) The corresponding reconstructed phases. The scale is given in units of waves.

estimate to the true phase screen is not the best indication of success since one phase screen, to a degree, can correct the phase in a neighboring phase screen if the screens are close to one another.

The algorithm's ability to reconstruct phase maps that match the true phase screens strongly depends on the propagation distance from one screen to the next. We found that when the distance between phase screens was relatively small (compared to the total distance of 100 m) the reconstructed phase maps did not agree with the true phase. However, in these instances, the sum of two phase maps agreed well with the sum of the two true phase maps. This is to be expected since phase screens very close to one another act like a single phase screen with phase equal to the sum of the two phases. This also confirms the notion that a single phase screen is

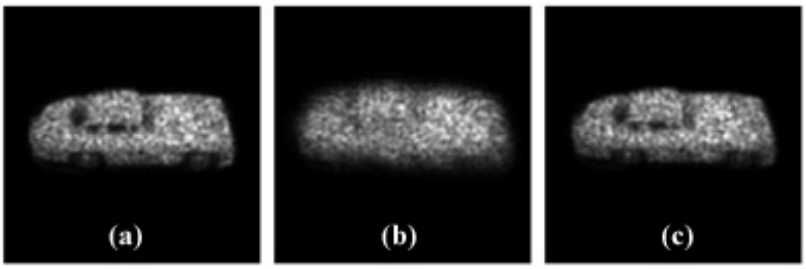

Figure 3-8. Results for the two-screen simulation (Case 2). (a) The ideal image, (b) the image when there is no aberration correction, (c) the image when the phase estimates have been used in the reconstruction.

capable of adequately representing a range of volume phase errors over a finite axial depth.

3.4.2. Case 2

Using a different object, we are able to demonstrate that this approach is not object-dependent. Figure 3-8 shows a two-phase screen simulation and reconstruction. For the aberrated image in Figure 3-8(b), the absolute error was 0.3368. Upon reconstruction, the absolute error was improved to 0.1804. Figure 3-9 shows the magnitude of the field backpropagated to the image (on the left) from the detector (on the right). Figure 3-9(e) - Figure 3-9(h) show an enlarged portion of vertical and horizontal slices near the image. We have successfully avoided any "telescopic oversharpening" effect of multiple phase screens, as demonstrated in Figure 3-3(b) although we can see differences in the propagation of individual speckles, Figure 3-8 shows that we were able to reconstruct a reasonably good image with similar speckles.

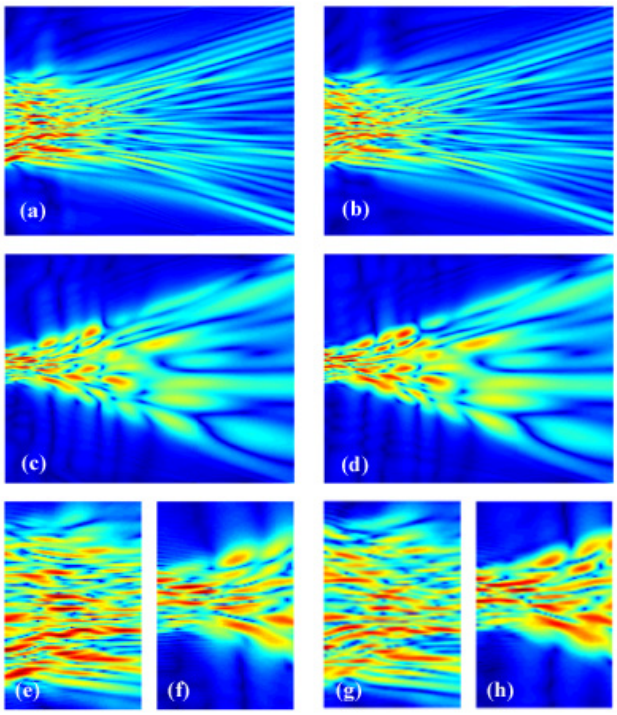

Figure 3-9. Field magnitude versus *z* from the image to the detector (left to right); each pair: truth (left) and reconstruction (right). (a), (b) Horizontal slice; (c), (d) vertical slice; and (e) – (h) magnified slices of (a), (b), (c), and (d) near the image.

3.5. Conclusion

We have successfully demonstrated, in simulation, the ability to estimate unknown phase errors and reconstruct images from digital holography data when multiple planes of aberrations are present causing anisoplanatic blurring. Image reconstruction has been shown for two and three planes of optical aberrations. Good reconstruction results with two and three phase screens under heavily anisoplanatic conditions is a significant advance. Future research should include optimizing of the two- and three-screen cases for increased robustness, extending it to a greater number of phase screens to more accurately model volume atmospheric turbulence, and developing an

understanding of performance as a function of the statistics of the object and imaging scenario.

3.6. Appendix: Derivation of Gradient Expressions for Phase Errors in Multiple Planes

The partial derivative of the sharpness metric S with respect to the phase $\phi_p(x_0, y_0)$ at a particular location in the p^{th} phase screen, by the chain rule of partial derivatives, is

$$\frac{\partial S}{\partial \phi_p(x_0, y_0)} = \sum_{\xi,\eta} \frac{\partial S}{\partial I(\xi,\eta)} \frac{\partial I(\xi,\eta)}{\partial \phi_p(x_0, y_0)} \tag{3.18}$$

The sharpness metric, S, originally given in Eq. (3.12) is defined as

$$S = S_1 + S_2 = \sum_{\xi,\eta} I^{\beta}(\xi,\eta) - \alpha \sum_{k=1}^{K} \sum_{f_\xi, f_\eta} W(f_\xi, f_\eta) \left| \tilde{F}_k(f_\xi, f_\eta) \right|^2 . \tag{3.19}$$

Here we break the metric into two terms and solve the gradient expressions independently. Therefore,

$$\frac{\partial S}{\partial \phi_p(x_0, y_0)} = \sum_{\xi,\eta} \frac{\partial S_1}{\partial I(\xi,\eta)} \frac{\partial I(\xi,\eta)}{\partial \phi_p(x_0, y_0)} + \sum_{f_\xi, f_\eta} \frac{\partial S_2}{\partial \left| \tilde{F}(f_\xi, f_\eta) \right|} \frac{\partial \left| \tilde{F}(f_\xi, f_\eta) \right|}{\partial \phi_p(x_0, y_0)} . \tag{3.20}$$

First, we will derive $\partial I(\xi,\eta)/\partial\phi_p(x_0,y_0)$ found in the partial derivative of S_1.

$$\frac{\partial I(\xi,\eta)}{\partial\phi_p(x_0,y_0)} = \frac{1}{K}\sum_{k=1}^{K}\left[f_k^*(\xi,\eta)\frac{\partial f_k(\xi,\eta)}{\partial\phi_p(x_0,y_0)} + \text{c.c.}\right] \tag{3.21}$$

where k is the specific speckle realization, K is the total number of speckle realizations and c.c. stands for the complex conjugate of the first term in the summation. Using the definition in Eq. (3.11) for $f_k(\xi,\eta)$,

$$\frac{\partial I(\xi,\eta)}{\partial\phi_p(x_0,y_0)} = \frac{1}{K}\sum_{k=1}^{K}\left\{ f_k^*(\xi,\eta)\frac{\partial}{\partial\phi_p(x_0,y_0)}\mathcal{P}_{P+1\to 0}^{\dagger}\left[G_k(x,y)\right] + \text{c.c.}\right\}. \tag{3.22}$$

We will expand the propagator to explicitly show terms containing $\phi_p(x_0,y_0)$:

$$\begin{aligned}\frac{\partial I(\xi,\eta)}{\partial\phi_p(x_0,y_0)} = \frac{1}{K}\sum_{k=1}^{K}\Bigg\{ & f_k^*(\xi,\eta)\frac{\partial}{\partial\phi_p(x_0,y_0)}\mathcal{F}_r\Big[-z_1;\exp(-i\phi_1)\,\mathcal{A}\big\{-z_2;\exp(-i\phi_2)\ \cdots \\ & \times\mathcal{A}\Big[-z_p;\exp\Big[-i\phi_p(x_p,y_p)\Big]\ \cdots\ \mathcal{A}\big\{-z_P;\exp(-i\phi_P)\,\mathcal{A}\big[-z_{P+1};G_k(x,y)\big]\big\}\Big]\big\}\Big] \ +\ \text{c.c.}\Bigg\}\end{aligned} \tag{3.23}$$

$$\frac{\partial I(\xi,\eta)}{\partial \phi_p(x_0,y_0)} = \frac{1}{K}\sum_{k=1}^{K}\left\{ f_k^*(\xi,\eta)\mathcal{F}_r\left[-z_1;\exp(-i\phi_1)\mathcal{A}\left\{ -z_2;\exp(-i\phi_2)\quad \cdots \right.\right.\right.$$
$$\left.\left.\left. \times\mathcal{A}\left[-z_p;\frac{\partial}{\partial\phi_p(x_0,y_0)}\exp\left[-i\phi_p(x_p,y_p)\right]\ \cdots\ \mathcal{A}\left\{-z_P;\exp(-i\phi_P)\mathcal{A}\left[-z_{P+1};G_k(x,y)\right]\right\}\right]\right\}\right] + \text{ c.c.}\right\} \tag{3.24}$$

Using the Kronecker delta function, $\phi_p(x_p,y_p)\delta_{x_0,x_p}\delta_{y_0,y_p} = \phi_p(x_0,y_0)\delta_{x_0,x_p}\delta_{y_0,y_p}$:

$$\frac{\partial I(\xi,\eta)}{\partial \phi_p(x_0,y_0)} = \frac{1}{K}\sum_{k=1}^{K}\left\{ f_k^*(\xi,\eta)\mathcal{F}_r\left[-z_1;\exp(-i\phi_1)\mathcal{A}\left\{ -z_2;\exp(-i\phi_2)\quad \cdots \right.\right.\right.$$
$$\left.\left.\left. \times\mathcal{A}\left[-z_p;-i\delta_{x_0,x_p}\delta_{y_0,y_p}\exp\left[-i\phi_p(x_0,y_0)\right]\ \cdots\ \mathcal{A}\left\{-z_P;\exp(-i\phi_P)\mathcal{A}\left[-z_{P+1};G_k(x,y)\right]\right\}\right]\right\}\right] + \text{ c.c.}\right\} \tag{3.25}$$

Using the definition from Eq. (3.9), the expression simplifies to

$$\frac{\partial I(\xi,\eta)}{\partial \phi_p(x_0,y_0)} = \frac{-i}{K}\sum_{k=1}^{K}\left[f_k^*(\xi,\eta)\mathcal{F}_r\left\{ -z_1;\exp(-i\phi_1)\mathcal{A}\left[-z_2;\exp(-i\phi_2)\ \cdots \right.\right.\right.$$
$$\left.\left.\left. \times\mathcal{A}\left\{ -z_p;\delta_{x_0,x_p}\delta_{y_0,y_p}\mathcal{P}^{\dagger}_{P+1\to p^+}\left[G_k(x,y)\right]\right\}+\text{c.c.}\right]\right\}\right] \tag{3.26}$$

$$\frac{\partial I(\xi,\eta)}{\partial \phi_p(x_0,y_0)} = \frac{2}{K}\sum_{k=1}^{K} \mathrm{Im}\Bigg[f_k^*(\xi,\eta)\mathcal{F}_r\Big\{-z_1;\exp(-i\phi_1)\mathcal{A}\Big[-z_2;\exp(-i\phi_2)\ \cdots \\ \times \mathcal{A}\Big\{-z_p;\delta_{x_0,x_p}\delta_{y_0,y_p}\mathcal{P}^{\dagger}_{P+1\to p^+}\left[G_k(x,y)\right]\Big\}\Big]\Big\}\Bigg] \tag{3.27}$$

using the definition $iZ+(iZ)^* = -2b = -2\,\mathrm{Im}(Z)$, where $Z = a+ib$. We next derive the partial derivative $\partial S_1/\partial I(\xi,\eta)$.

$$\frac{\partial S_1}{\partial I(\xi,\eta)} = \frac{\partial}{\partial I(\xi,\eta)}\left[\sum_{\xi',\eta'} I^{\beta}(\xi',\eta')\right] = \frac{\partial I^{\beta}(\xi,\eta)}{\partial I(\xi,\eta)} = \beta I^{\beta-1}(\xi,\eta). \tag{3.28}$$

Combining Eqs. (3.18), (3.26) and (3.28), we have

$$\frac{\partial S_1}{\partial \phi_p(x_0,y_0)} = \sum_{\xi,\eta}\frac{\partial S_1}{\partial I(\xi,\eta)}\frac{\partial I(\xi,\eta)}{\partial \phi_p(x_0,y_0)} \\ = \frac{2\beta}{K}\sum_{k=1}^{K}\sum_{\xi,\eta}\mathrm{Im}\Big\{I^{\beta-1}(\xi,\eta)f_k^*(\xi,\eta)\mathcal{F}_r\Big[-z_1;\exp(-i\phi_1)\mathcal{A}\Big\{-z_2;\exp(-i\phi_2)\ \cdots \\ \times\mathcal{A}\Big[-z_p;\delta_{x_0,x_p}\delta_{y_0,y_p}\mathcal{P}^{\dagger}_{P+1\to p^+}\left[G_k(x,y)\right]\Big]\Big\}\Big]\Big\}. \tag{3.29}$$

Here, we are explicit with the coordinates for each transformation where

$$\mathcal{F}_{r_{(x_1,y_1)\to(\xi,\eta)}}\left[z;g\left(x_1,y_1\right)\right]=\frac{e^{ikz}}{i\lambda z}\exp\left[\frac{i\pi}{\lambda z}\left(\xi^2+\eta^2\right)\right]\sum_{x_1,y_1}g\left(x_1,y_1\right)\exp\left[\frac{i\pi}{\lambda z}\left(x_1^2+y_1^2\right)\right]\exp\left[\frac{-i2\pi}{\lambda z}\left(x_1\xi+y_1\eta\right)\right] \tag{3.30}$$

$$\begin{aligned}\mathcal{A}_{\left(x_p,y_p\right)\to\left(x_{p-1},y_{p-1}\right)}\left[z;g\left(x_p,y_p\right)\right]=\sum_{f_{x_p},f_{y_p}}\Bigg[\sum_{x_p,y_p}\left\{g\left(x_p,y_p\right)\exp\left[-i2\pi\left(x_pf_{x_p}+y_pf_{y_p}\right)\right]\right\}\\ \times\exp\left[-i\pi\lambda z\left(f_{x_p}^2+f_{y_p}^2\right)\right]\exp\left[i2\pi\left(x_{p-1}f_{x_p}+y_{p-1}f_{y_p}\right)\right]\Bigg]\end{aligned} \tag{3.31}$$

$$\begin{aligned}\frac{\partial S_1}{\partial\phi_p\left(x_0,y_0\right)}=\frac{2\beta}{K}\sum_{k=1}^{K}\sum_{\xi,\eta}\mathrm{Im}\Big\{I^{\beta-1}\left(\xi,\eta\right)f_k^*\left(\xi,\eta\right)\mathcal{F}_{r_{(x_1,y_1)\to(\xi,\eta)}}\Big[-z_1;\exp\left[-i\phi_1\left(x_1,y_1\right)\right]\\ \times\mathcal{A}_{(x_2,y_2)\to(x_1,y_1)}\Big\{-z_2;\exp\left[-i\phi_2\left(x_2,y_2\right)\right]\ \cdots\\ \times\mathcal{A}_{\left(x_p,y_p\right)\to\left(x_{p-1},y_{p-1}\right)}\left[-z_p;\ \delta_{x_0,x_p}\delta_{y_0,y_p}\exp\left[-i\phi_p\left(x_0,y_0\right)\right]\right]\cdots\\ \times\mathcal{A}_{(x_P,y_P)\to(x_{P-1},y_{P-1})}\left\{-z_P;\exp\left(-i\phi_P\right)\mathcal{A}_{(x,y)\to(x_P,y_P)}\left[-z_{P+1};G_k\left(x,y\right)\right]\right\}\Big]\Big\}\Big]\Big\}\end{aligned} \tag{3.32}$$

We can exchange the order of the summations such that (ξ,η) are the innermost coordinates and (x_p, y_p) are the outermost coordinates. Afterward, $\partial S_1 / \partial \phi_p(x_0, y_0)$ can further be simplified to

$$\frac{\partial S_1}{\partial \phi_p(x_0,y_0)} = \frac{2\beta}{K}\sum_{k=1}^{K} \mathrm{Im}\left\{ \mathcal{P}^{\dagger}_{P+1\to p^+}\left[G_k(x,y)\right]\mathcal{P}_{0\to p^-}\left[I^{\beta-1}(\xi,\eta) f_k(\xi,\eta)\right]^*\right\}. \tag{3.33}$$

Similarly, for the second term in Eq. (3.19),

$$\begin{aligned}\frac{\partial S_2}{\partial \phi_p(x_0,y_0)} &= \frac{\partial}{\partial \phi_p(x_0,y_0)}\left[\alpha\sum_{k=1}^{K}\sum_{f_\xi,f_\eta} W(f_\xi,f_\eta)\left|\tilde{F}_k(f_\xi,f_\eta)\right|^2\right] \\ &= \alpha\sum_{k=1}^{K}\sum_{f_\xi,f_\eta} W(f_\xi,f_\eta)\left[\tilde{F}_k^*(f_\xi,f_\eta)\frac{\partial \tilde{F}_k(f_\xi,f_\eta)}{\partial \phi_p(x_0,y_0)} + \text{c.c.}\right]\end{aligned} \tag{3.34}$$

where

$$\frac{\partial \tilde{F}_k(f_\xi,f_\eta)}{\partial \phi_p(x_0,y_0)} = \frac{\partial}{\partial \phi_p(x_0,y_0)} FT\left[f_k(\xi,\eta)\right] \tag{3.35}$$

and $FT[\cdot]$ represents a Fourier transform. Again, we can expand $f_k(\xi,\eta)$ to explicitly reveal terms containing $\phi_p(x_0,y_0)$

$$\begin{aligned}\frac{\partial \tilde{F}_k\left(f_\xi, f_\eta\right)}{\partial \phi_p\left(x_0, y_0\right)} &= \frac{\partial}{\partial \phi_p\left(x_0, y_0\right)} FT\left\{\mathcal{F}_r\left[-z_1; \exp\left(-i\phi_1\right) \mathcal{A}\left\{-z_2; \exp\left(-i\phi_2\right) \cdots\right.\right.\right. \\ &\qquad \left.\left.\left. \times \mathcal{A}\left[-z_p; \exp\left[-i\phi_p\left(x_p, y_p\right)\right] \cdots \mathcal{A}\left\{-z_P; \exp\left(-i\phi_P\right) \mathcal{A}\left[-z_{P+1}; G_k\left(x, y\right)\right]\right\}\right]\right\}\right]\right\} \\ &= FT\left\{\mathcal{F}_r\left[-z_1; \exp\left(-i\phi_1\right) \mathcal{A}\left\{-z_2; \exp\left(-i\phi_2\right) \cdots\right.\right.\right. \\ &\qquad \left.\left.\left. \times \mathcal{A}\left[-z_p; \frac{\partial}{\partial \phi_p\left(x_0, y_0\right)} \exp\left[-i\phi_p\left(x_p, y_p\right)\right] \cdots \mathcal{A}\left\{-z_P; \exp\left(-i\phi_P\right) \mathcal{A}\left[-z_{P+1}; G_k\left(x, y\right)\right]\right\}\right]\right\}\right]\right\}\end{aligned} \tag{3.36}$$

$$\begin{aligned}\frac{\partial \tilde{F}_k\left(f_\xi, f_\eta\right)}{\partial \phi_p\left(x_0, y_0\right)} &= FT\left\{\mathcal{F}_r\left[-z_1; \exp\left(-i\phi_1\right) \mathcal{A}\left\{-z_2; \exp\left(-i\phi_2\right) \cdots\right.\right.\right. \\ &\qquad \left.\left.\left. \times \mathcal{A}\left[-z_p; -i\delta_{x_0, x_p} \delta_{y_0, y_p} \exp\left[-i\phi_p\left(x_p, y_p\right)\right] \mathcal{A}\left\{-z_P; \exp\left(-i\phi_P\right) \mathcal{A}\left[-z_{P+1}; G_k\left(x, y\right)\right]\right\}\right]\right\}\right]\right\} \\ &= -iFT\left\{\mathcal{F}_r\left[-z_1; \exp\left(-i\phi_1\right) \mathcal{A}\left\{-z_2; \exp\left(-i\phi_2\right) \cdots \mathcal{A}\left[-z_p; \delta_{x_0, x_p} \delta_{y_0, y_p} \mathcal{P}^\dagger_{P+1 \to p^+}\left[G_k\left(x, y\right)\right]\right]\right\}\right]\right\}\end{aligned} \tag{3.37}$$

Plugging Eq. (3.36) into Eq. (3.34), we find

$$\frac{\partial S_2}{\partial \phi_p\left(x_0,y_0\right)} = 2\alpha \sum_{k=1}^{K} \sum_{f_\xi, f_\eta} W(f_\xi, f_\eta)\,\mathrm{Im}\left\{ \tilde{F}_k^*(f_\xi, f_\eta) FT\left[\mathcal{F}_r\left\{ -z_1; \exp\left(-i\phi_1\right) \mathcal{A}\left[-z_2; \exp\left(-i\phi_2\right) \quad \cdots \right.\right.\right.\right.$$
$$\left.\left.\left.\left. \times \mathcal{A}\left\{ -z_p; \delta_{x_0,x_p}\delta_{y_0,y_p} \mathcal{P}^{\dagger}_{P+1\to p^+}\left[G_k\left(x,y\right)\right]\right\}\right]\right\}\right]\right\}. \tag{3.38}$$

At this point, we also choose to flip the signs and work with the complex conjugate of terms in Eq. (3.38) Similar to what was done in Eq. (3.32), we can exchange the order of the remaining integrals such that $\left(f_\xi, f_\eta\right)$ are the innermost coordinates and $\left(x_p, y_p\right)$ are the outermost coordinates.

$$\frac{\partial S_2}{\partial \phi_p\left(x_0,y_0\right)} = 2\alpha \sum_{k=1}^{K} \mathrm{Im}\left[\mathcal{P}^{\dagger}_{P+1\to p^+}\left[G_k\left(x,y\right)\right]\left\{ \mathcal{A}\left[z_p; \quad \cdots \right.\right.\right.$$
$$\left.\left.\left. \times \exp\left(i\phi_2\right) \mathcal{A}\left[z_2; \exp\left(i\phi_1\right) \mathcal{F}_r\left\{ z_1; FT^{-1}\left[W\left(f_\xi, f_\eta\right) \tilde{F}_k\left(f_\xi, f_\eta\right)\right]\right\}\right]\right\}^*\right]. \tag{3.39}$$

This can be further simplified to

$$\frac{\partial S_2}{\partial \phi_p\left(x_0,y_0\right)} = 2\alpha \sum_{k=1}^{K} \mathrm{Im}\left[\mathcal{P}^{\dagger}_{P+1\to p^+}\left[G_k\left(x,y\right)\right] \mathcal{P}_{0\to p^-}\left\{ FT^{-1}\left[W\left(f_\xi, f_\eta\right) \tilde{F}_k\left(f_\xi, f_\eta\right)\right]\right\}^*\right]. \tag{3.40}$$

The total partial derivative expression is

$$\frac{\partial S}{\partial \phi_p(x_0,y_0)} = \frac{2\beta}{K}\sum_{k=1}^{K}\mathrm{Im}\left\{\mathcal{P}^{\dagger}_{P+1\to p^+}\left[G_k(x,y)\right]\mathcal{P}_{0\to p^-}\left[I^{\beta-1}(\xi,\eta)f_k(\xi,\eta)\right]^*\right\} \\ +2\alpha\sum_{k=1}^{K}\mathrm{Im}\left[\mathcal{P}^{\dagger}_{P+1\to p^+}\left[G_k(x,y)\right]\mathcal{P}_{0\to p^-}\left\{FT^{-1}\left[W(f_\xi,f_\eta)\tilde{F}_k(f_\xi,f_\eta)\right]\right\}^*\right]. \tag{3.41}$$

3.7. References

1. L. C. Andrews and R. L. Phillips, *Laser beam propagation through random media,* 2nd (SPIE Press, Bellingham, Wash., 2005).

2. A. Ishimaru, *Wave propagation and scattering in random media,* (Academic Press, New York, 1978).

3. R. A. Muller and A. Buffington, "Real-time correction of atmospherically degraded telescope images through image sharpening," J. Opt. Soc. Am. **64**, 1200-1210 (1974).

4. R. G. Paxman and J. C. Marron, "Aberration correction of speckled imagery with an image-sharpness criterion," Proc. SPIE **976**, 37-47 (1988).

5. F. Berizzi and G. Corsini, "Autofocusing of inverse synthetic aperture radar images using contrast optimization," IEEE Transactions on Aerospace and Electronic Systems **32**, 1185-1191 (1996).

6. J. R. Fienup and J. J. Miller, "Aberration correction by maximizing generalized sharpness metrics," J. Opt. Soc. Am. A **20**, 609-620 (2003).

7. S. T. Thurman and J. R. Fienup, "Phase-error correction in digital holography," J. Opt. Soc. Am. A **25**, 983-994 (2008).

8. S. T. Thurman and J. R. Fienup, "Correction of anisoplanatic phase errors in digital holography," J. Opt. Soc. Am. A **25**, 995-999 (2008).

9. J. M. Martin and S. M. Flatte, "Simulation of point-source scintillation through 3-dimensional random-media," J. Opt. Soc. Am. A **7**, 838-847 (1990).

10. H. G. Booker, J. A. Ferguson, and H. O. Vats, "Comparison between the extended-medium and the phase-screen scintillation theories," J. Atmos. Ter. Phys. **47**, 381-399 (1985).

11. R. G. Lane, A. Glindemann, and J. C. Dainty, "Simulation of a Kolmogorov phase screen," Waves in Random Media **2**, 209-224 (1992).

12. J. R. Fienup, "Phase-retrieval algorithms for a complicated optical system," Appl. Opt. **32**, 1737-1746 (1993).

13. M. C. Roggemann and B. Welsh, *Imaging through turbulence,* (CRC Press, Boca Raton, 1996).

14. J. R. Fienup, "Invariant error metrics for image reconstruction," Appl. Opt. **36**, 8352-8357 (1997).

15. M. Guizar-Sicairos, S. T. Thurman, and J. R. Fienup, "Efficient subpixel image registration algorithms," Opt. Lett. **33**, 156-158 (2008).

4. Imaging through Phase Screens: Experiment

4.1. Experimental Setup

Our experiments with multiple phase screens were performed using the laboratory digital holography set-up illustrated in Figure 4-1**.** An argon-ion laser operating at a wavelength of 514 nm was used as the coherent illumination source. A beam splitter was used to divide the light between two paths, an off-axis reference beam and a beam to illuminate the object. The laser output power was 400 mW and the power in the reference arm of the experiment was reduced with a neutral density filter of optical density 5.5 such that the light from the reference beam was moderately brighter than from the diffuse scattering object. In this chapter, we present results for two different imaging cases. The first case is one with a 3.2 cm wide brass toy train and three 7.9 mm (5/16") ball bearings mounted on a black, low-reflectance felt cloth. In the second case, we removed the ball bearings and imaged the train only.

The object was mounted on a computer-controlled rotation stage and was rotated 2.09 milliradians between collection frames. We collected the holographic

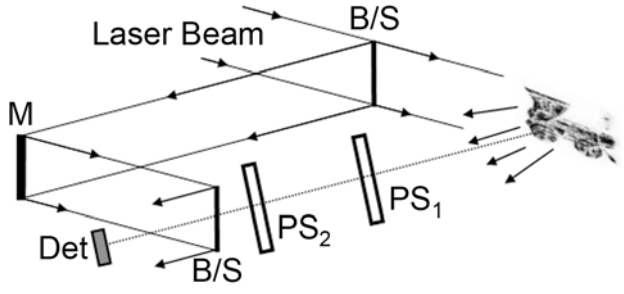

Figure 4-1. Layout of the digital holography experimental setup including phase screens. B/S, beamsplitter; M, mirror; Det, detector array, and PS, phase screen.

interference patterns for K = 9 speckle realizations using a complementary metal-oxide-semiconductor (CMOS) camera with a 6.7 μm pixel pitch. The camera collected 1024x1280 pixels, but we cropped the data to a 1024x1024 square. We digitally separated the object field by first Fourier transforming the collected intensity data, windowing out the object term and performing an inverse Fourier transform.

With access to the field from the object obtained through this holographic reconstruction, we can digitally propagate the field to any z plane. We used paraxial angular spectrum propagation where an arbitrary field $g(x, y)$ can be propagated a distance z by

$$\mathcal{A}\left[z; g\left(x, y\right)\right] = FT^{-1}\left\{FT\left[g\left(x, y\right)\right]\exp\left[-i\pi\lambda z\left(f_x^2 + f_y^2\right)\right]\right\} \qquad (4.1)$$

where FT denotes a Fourier transform. Angular spectrum propagation preserves the pixel sample spacing regardless of propagation distance. However, with the object being approximately five times larger than the detector, as was the case in this experimental arrangement, the initial 1024x1024 array recorded by the detector would need to be embedded into a much larger array to avoid aliasing artifacts when propagating to the object plane. Multiplying the field in the detector plane by an appropriate converging spherical wave allows for coordinate transformation to collimated space [1] that allows us to maintain a reasonable array size for large object/detector size ratios.

For static phase screens, we used plastic compact disk (CD) cases that were slightly warped by heat treating to increase the aberration. To cause anisoplanatism,

two phase screens were separated within the propagation path between the object and the detector. The total distance between the object and detector was 3.32 m. One screen (Screen A) was placed 22 cm from the detector and the other (Screen B) was placed 104.3 cm from the detector. The uncorrected images (corrected just for focusing) when blurred by Screen A are shown in Figure 4-2(a) and Figure 4-2(b), by Screen B are shown in Figure 4-2(c) and Figure 4-2(d), and by both screens are shown in Figure 4-2(e) and Figure 4-2(f). The anisoplanatism introduced by these

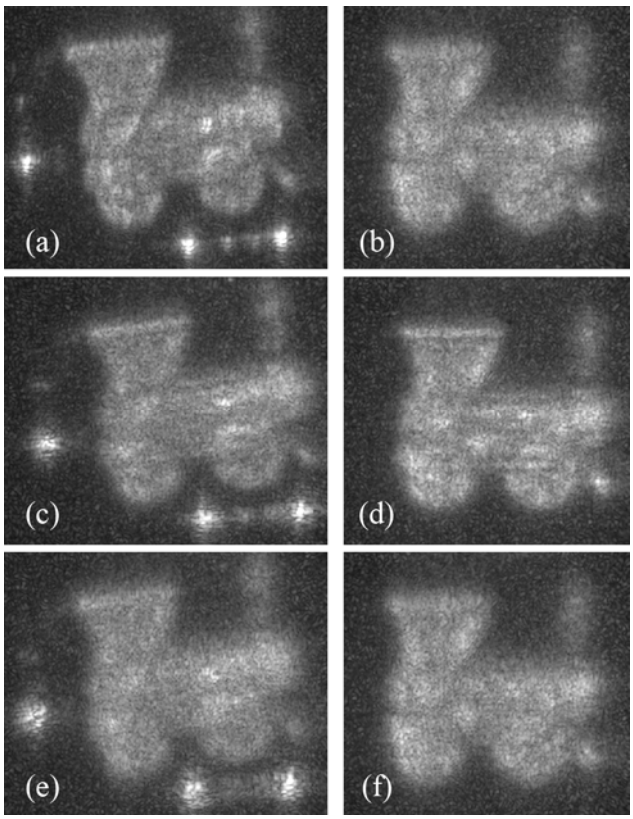

Figure 4-2. Reconstructed images, uncorrected for phase errors, of objects with (left) and without (right) ball bearings which act like point sources. (a, b) with Screen A, (c, d) with Screen B, and (e, f) with both screens present in the imaging path. Images shown here are scaled, saturated and cropped to show 530x650 pixels (left column, with ball bearings) and 535x575 pixels (right column, without ball bearings) of the entire 1024x1024 array.

two phase screens can be seen in the images of the ball bearings, which act like point sources and therefore are local point spread functions, below and to the left of the train. In both Figure 4-2(c) and Figure 4-2(e) they are all distinctly different from one another in their details. In contrast, with only Screen A present, Figure 4-2(a) shows that all three point sources have similar blur functions, i.e., an approximately isoplanatic case.

4.2. Reconstruction Methods

As described in Section 3.3, to quantify the quality of a given image we used the modified Muller-Buffington sharpness metric [2, 3]

$$S = \sum_{\xi,\eta} M(\xi,\eta) I^{\beta}(\xi,\eta) - \alpha \sum_{k=1}^{K} \sum_{f_\xi f_\eta} W_k(f_\xi, f_\eta) \left| \tilde{F}_k(f_\xi, f_\eta) \right|^2 , \qquad (4.2)$$

where $M(\xi,\eta)$ is an optional window function we included to allow one to select a sub-region of the image on which to base the phase error correction (equal to unity over the entire image unless otherwise stated), $I(\xi,\eta)$ is the incoherent sum of our K speckled images, α and β are constants (we used β = 1.01 [4]), $W_k(f_\xi, f_\eta)$ is a weighting function defined by the spatial frequency content of the k^{th} speckle realization of the object field sensed over the area of the digital hologram, and $\tilde{F}_k(f_\xi, f_\eta)$ is the Fourier transform of the k^{th} object field in the image plane. $W_k(f_\xi, f_\eta)$ was the same for all the speckle realizations. For the first case, with the

scene containing both the train and the ball bearings, we used only the first term of this sharpness metric in a nonlinear optimization algorithm [2] to reconstruct the two discrete planes of phase errors present in our optical system and a corrected image. We found the metric to perform well under this imaging condition, the solution for the estimated phase screens being driven in large part by the strong glints produced by the ball bearings in the scene. For the second case in which the ball bearings were removed, we found it necessary to use both terms in this metric to prevent oversharpening of the image. Estimating multiple phase screens in a sharpness-metric nonlinear optimization approach tends to drive the solution to a telescope-like pair of phase screens, demagnifying and warping the image, as described in Section 3.3. This effect makes the sharpness metric higher [2], but the image may be a poor reconstruction of the original object. To combat this specific form of oversharpening, the second term in Eq. (2) requires the spatial bandwidth of the field to be the same in the image plane as it is in the detector plane.

An analytic gradient for that sharpness metric allows for efficient computation in a conjugate gradient search [2]. Unlike the simulation described in Section 3.3, for these reconstructions we employed a bootstrapping approach using the method of sieves [5]. In this approach, we start by convolving a point-by-point version of the analytic gradient with a large Gaussian kernel so that only low-order phase corrections are made. Through successive iterations, we slowly reduce the size of the Gaussian kernel until we eventually solve for the point-by-point phase map reconstruction; this helps to avoid algorithm stagnation. For this work, we started

with a Gaussian kernel with a full width, half maximum of 100 pixels and reduced the Gaussian kernel size by half every five iterations. Point-by-point phases were used to better estimate the high frequency content present in the physical screens. The nonlinear optimization code took 130 minutes to run on an IBM x3755 server with four AMD Opteron 8224 SE processors. We believe that with more efficient programming and use of graphics processing unit (GPU) cards, this process would run many times faster.

4.3. Results

We also investigated single-plane correction in each of several planes; we found the best single plane correction to be in the plane of the phase screen A, the one closer to the detector. This near-isoplanatic image correction, shown in Figure 4-3(a) and Figure 4-3(b), are a slight improvement upon the uncorrected images shown in Figure 4-2(e) and Figure 4-2(f). We see strong evidence of anisoplanatism still present in the resulting images in Figure 4-3(a) and Figure 4-3(b), since one cannot correct anisoplanatic errors in a plane near the detector. Figure 4-3(c) and Figure 4-3(d) show images corrected, using the weighting function $M\left(\xi,\eta\right)$ in Eq. (4.2), over small, isoplanatic patches designated by the dashed regions. The features within this region of interest are sharpened while the rest of the image remains unimproved. In fact, areas far from the corrected region in Figure 4-3(c) are blurred even more than the uncorrected image, similar to what happens with adaptive optics correction for areas of an image outside of the isoplanatic patch surrounding a guide star. Figure

4-3(e) and Figure 4-3(f) show the images corrected in both of the planes of the pair of phase screens. In the space-variant correction shown in Figure 4-3(e), all three ball bearings have a uniformly tight focus. Furthermore, secondary reflections from the neighboring ball bearings, which are physically present, are clearly visible between the two lower ball bearings, although previously undetectable in the uncorrected case. The details of the train, including the spokes on the wheels and other fine features, are apparent only with this multiple-plane phase-screen correction.

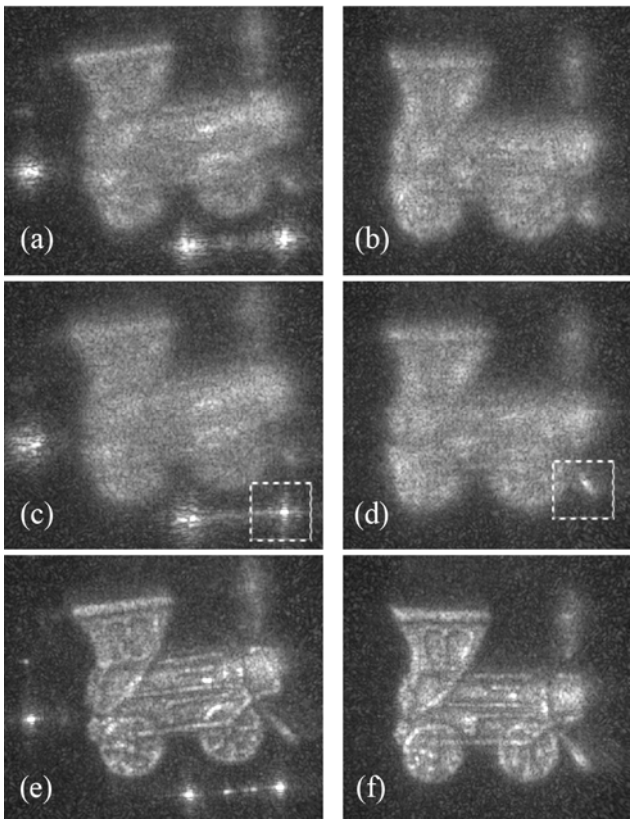

Figure 4-3. Comparison of (a, b) isoplanatic correction across the entire array, (c, d) isoplanatic correction over a smaller region of the image, indicated by dashed line and (e, f) anisoplanatic correction of phases in both the planes of Screens A and B. Figures are cropped to show 530x650 pixels (left column) and 535x575 pixels (right column) of the entire 1024x1024 array. Images are scaled and saturated to bring out details of the dim portions of the objects in addition to bright glints.

We repeated this experiment after removing the ball bearings, imaging only the toy train. The experimental setup remained the same for both imaging scenarios. The absence of bright, sharp glints in the object makes it more difficult for the image sharpening algorithm. As previously mentioned, we used the modified sharpness metric of Eq. (4.2). The algorithm was able to correct the anisoplanatic errors to produce a much sharper image, shown in Figure 4-3(f), despite having no strong point scatterers.

4.4. Conclusion

We have successfully demonstrated anisoplanatic correction of two static phase screens in a laboratory digital holography experiment using an image sharpening algorithm. The corrected images were much sharper than the best single-plane correction case, even when the object contained no prominent point scatterers. We found it was necessary to add a term to the sharpness metric to avoid oversharpening of the image by demagnification. The approach is applicable to correcting any number of phase screens and should be applicable to a continuous 3-D volume of turbulence, although its performance will undoubtedly suffer with an increasing number of unknown phase parameters. Further research will be needed to determine the number of, and complexity of, phase screens that can be successfully corrected for a given type of object (we expect it to depend on the object's space-bandwidth product, contrast and spatial structure, for example) and signal-to-noise ratio.

4.5. References

1. A. E. Siegman, *Lasers,* (University Science Books, Sausalito, 1986).

2. A. E. Tippie and J. R. Fienup, "Phase-error correction for multiple planes using a sharpness metric," Opt. Lett. **34**, 701-703 (2009).

3. R. A. Muller and A. Buffington, "Real-time correction of atmospherically degraded telescope images through image sharpening," J. Opt. Soc. Am. **64**, 1200-1210 (1974).

4. S. T. Thurman and J. R. Fienup, "Phase-error correction in digital holography," J. Opt. Soc. Am. A **25**, 983-994 (2008).

5. U. Grenander, *Abstract inference,* (Wiley, New York, 1981).

5. Synthetic-Aperture Imaging: Experiment

5.1. Introduction

For many imaging applications, one desires to achieve high resolution while maintaining a wide field-of-view. Typically, with conventional optics, resolution or field-of-view must be sacrificed to achieve the other without a significantly more complex system. This tradeoff is due primarily to the increase in aberrations as the lens diameter and field-of-view increase. For optical systems that have demanding specifications on both the resolution and field-of-view, the number of optical elements in the system increases to compensate and correct for these effects. Furthermore, for focal-plane imaging applications, the number of pixels in the detector array can limit the space-bandwidth product. In this chapter, we discuss the implementation of a synthetic-aperture digital holography laboratory experiment in which we were able to achieve both high resolution and a relatively wide field-of-view simultaneously, all without imaging lenses in the system by using a computational imaging approach.

Large synthetic apertures can be formed by combining together multiple longitudinally translated frames of digital holography data, thereby increasing the resolution and the space-bandwidth product of the system [1-3]. In our laboratory experiment, we assembled two large synthetic-aperture digital holograms: one 218 mega-pixels in size, the other 1 gigapixel. Our synthetic-aperture reconstruction represents a significant increase in space-bandwidth product compared to recent

synthetic apertures such as Ref. [3]. This demonstrates a non-trival advancement in synthetic-aperture digital holography, given the demands on the system tolerance and stability of the experiment.

5.2. Experimental Setup and Data Acquisition

The experimental setup was configured in an off-axis, lensless Fourier transform geometry, as illustrated in Figure 5-1. Light from an argon-ion laser with an output power of 450 mW, operating at a wavelength of 514 nm, was spilt into two arms, a reference beam and an object illumination beam. In the reference arm, neutral density filters reduced the intensity of the beam and a 5X microscope objective focused the light into the end of a 3.5 μm single-mode fiber. The output of the fiber was placed in the plane of the object and served as a diffraction-limited reference point source. A second beam was positioned to flood illuminate the object at an off-axis angle of 18°. The object used in this experiment was a USAF chrome-on-glass

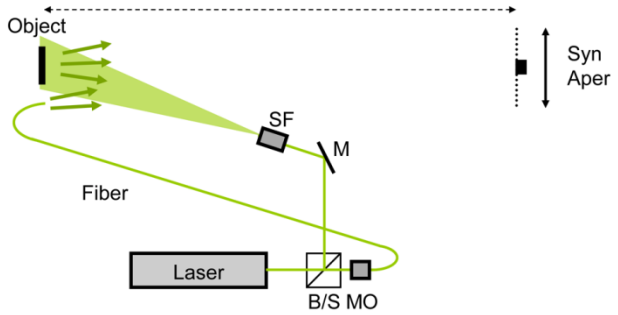

Figure 5-1. Experimental setup for off-axis, lensless Fourier transform digital holography synthetic-aperture aperture imaging. B/S, beamsplitter; M, mirror; SF, microscope objective plus pinhole spatial filter; MO, microscope objective and Syn Aper, width of synthetic aperture after raster scanning CCD.

bar target. Flat white paint was applied on the chrome side of the target as a means of providing diffuse reflection, and that side of the target faced away from the illumination beam and the camera, so the object was seen through the back of the glass plate. A portion of the USAF target was masked, such that the effective object area was 4.7 cm by 6.3 cm. The USAF target was positioned normal to the optical axis of the imaging system (i.e. free space propagation plus a detector array), making it parallel to the detector; mirror reflections from the glass substrate and the mirror-like chrome surface reflected away from the detector due to the off-axis illumination angle. The distance from the object to the detector was $z = 3.32$ m. The detector was a Retiga 2000R Q-Imaging CCD camera with a pixel pitch of 7.4 μm in both dimensions and an area of 1200 x 1600 pixels (8.88 mm x 11.84 mm). The CCD was mounted on two translation stages. The horizontal translation stage was mounted to the table, while the vertical stage was mounted to the horizontal stage, and it held the camera. Figure 5-2 shows the laboratory arrangement for all the components from two different viewing angles, highlighting both the laser output as well as the object-detector propagation path.

In order to acquire all the frames necessary for the full-aperture image, the camera was raster scanned, left to right, to gather a row of frames starting at the bottom left-hand corner of the aperture array, and then subsequent rows of frames were gathered bottom to top. We always acquired frames in the same direction to minimize hysteresis and mechanical backlash of the translation stages. The translation between frames was about 833 pixels horizontally and about 555 pixels

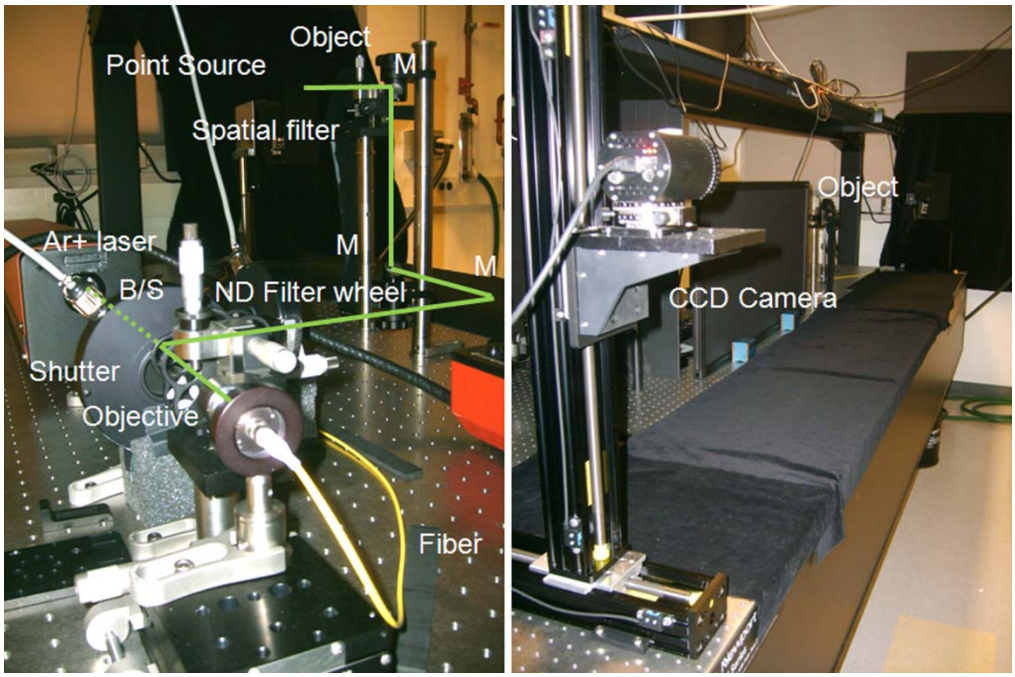

Figure 5-2. Photos of synthetic-aperture digital holography configuration.

vertically giving an approximately 50% overlap between frames. The redundant data from the overlapping areas served to help align and register frames since the accuracy and precision of the translation stages used in this experiment proved to be unacceptable for alignment requirements; the repeatability of the stages was 4 μm, and the accuracy across the entire travel distance was 76 μm [4], many times worse than the required accuracy described in Section 5.3.

The exposure time for each frame was 80 ms. In addition to a holographic frame for each position, a dark frame was taken for calibration purposes, and object-only and reference-only frames were taken for diagnostics. The total data acquisition time for all frames for a 21 x 21 frame exposure (over 800 Mpixels, of which ¾ were

redundant), including a two-second wait and settle time for the translation stages after moving to each location, was 5 hours and 58 minutes under automatic computer control. For a separate and independent acquisition of frames to form a gigapixel synthetic aperture, a total of 2835 (45 x 63) holography frames were acquired. Using the same procedure, but only collecting dark frames and holography frames (no additional frames for diagnostics), the total collection time was 11 hours and 37 minutes.

5.3. Registration and Mosaicking of a Large Synthetic Aperture

The hologram intensity in the detector plane is

$$\begin{aligned} H(x,y) &= \left|R(x,y)+F(x,y)\right|^2 \\ &= \left|R(x,y)\right|^2 + \left|F(x,y)\right|^2 + R(x,y)F^*(x,y) + F(x,y)R^*(x,y) \end{aligned} \tag{5.1}$$

where $R(x,y)$ is the reference field and $F(x,y)$ is the object field. A holographic image can be reconstructed by recovering the field in the detector plane by standard techniques (Fourier transform, zero out all but the desired term and inverse Fourier transform) as described in Section 1.2, and then digitally propagating the resulting field to the image plane. Figure 5-3(a) – (d) shows the image from a single CCD frame; Figure 5-3(a) shows the entire field of view of the image, while Figure 5-3(b) – (d) show zoomed-in regions of the image to emphasize the finer resolution elements of the USAF target. For a single frame, the finest resolved bars were (group, element) (1,1) for horizontal bars (vertical edges) and (1,3) for vertical bars

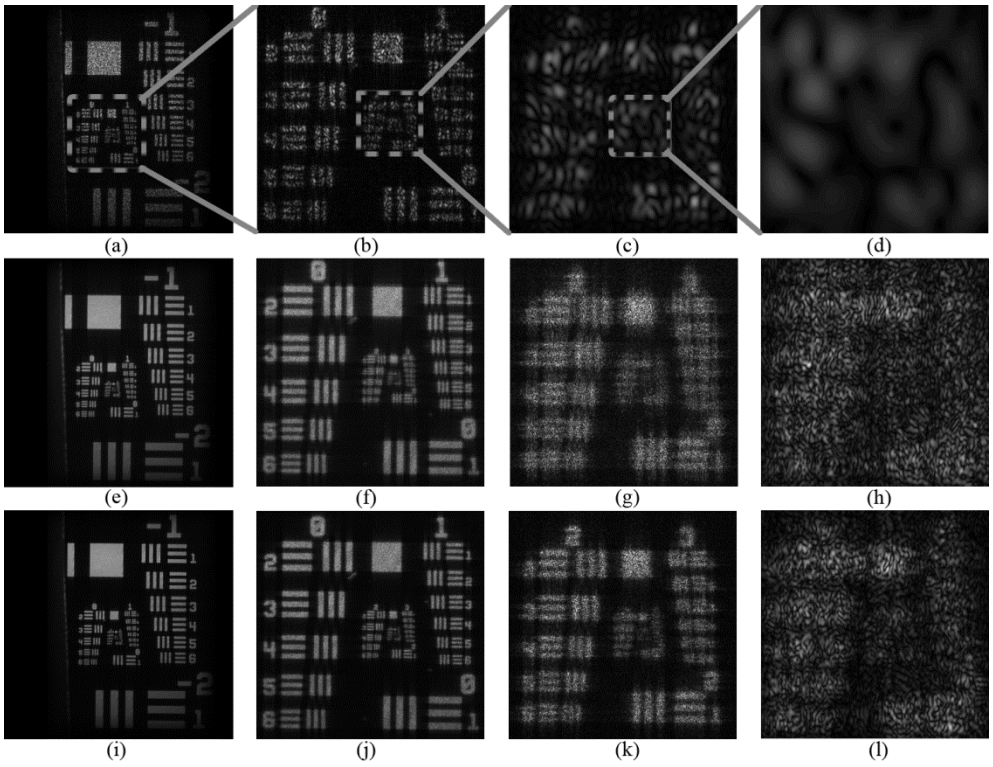

Figure 5-3. Holographic image reconstruction of (a) – (d) single frame; (e) – (h) initial mosaic; (i) – (l) optimized mosaic. Column 1 – 8700 x 6500 pixel area of entire image; Column 2 – 2550 x 2500 pixel subset of Col. 1; Column 3 – 650 x 650 pix subset of Col 2; Column 4 – 160 x 160 pixel subset of Col 3.

(horizontal edges), corresponding to 2.00 line-pairs (lp) per mm and 2.52 lp/mm, respectively. Note that an improvement by (n groups, m elements) is equivalent to a resolution improvement by a linear factor of $2^{n+m/6}$. In comparison, the theoretical diffraction-limited resolution is calculated as $\rho = (\lambda z)/D$, where D is the width of the aperture. The vertical aperture width of 8.89 mm gives a diffraction-limited resolution of 192 μm; for the horizontal aperture width of 11.8 mm, the resolution is 144 μm. Due to the speckled nature of coherent imaging, we expected to observe a resolution roughly ~3X worse than the incoherent diffraction-limited resolution

calculated [5]. Therefore, the theoretical resolvable bars of the USAF bar target are (group, element) (0,5) for horizontal bars (vertical edges) and (1,2) for vertical bars (horizontal edges), corresponding to 1.59 lp/mm and 2.24 line-pairs (lp) per mm, respectively as compared with 2.00 lp/mm and 2.52 lp/mm respectively observed experimentally. We see reasonably good agreement between the theoretical calculations and experimental measurements for a single frame.

Aperture synthesis was performed by first extracting the detector-plane complex field of each individual frame and then mosaicking together those fields. We found it important to register and mosaic the extracted fields rather than the hologram intensities because the latter's quasi-periodic fringe pattern, along with piston phase changes between frames, made frame-to-frame registration of holograms very challenging. Frame-to-frame registration must be done with great accuracy. To keep space-variant phase errors due to frame translation to 1/10 wave rms, one must register the frames accurately to within 1/7 pixel (about one micron for our CCD having 7.4 μm pixels) [6].

We found that the speckles in the object beam at the detector changed somewhat over the long data collection time, contributing to errors when registering each frame within the larger aperture. To minimize the accumulation of registration errors across the synthetic aperture in our initial mosaic, we registered each frame in the aperture with a single adjacent frame. This process was done by starting with the center frame of the entire aperture and registering adjacent frames in a

counterclockwise spiral pattern (even though the frames were gathered in a raster scan order), analogous to what is done with phase reconstructors [7]. Our early preliminary results showed that a spiral registration was more effective than starting in one corner of the array and registering in a raster scan order. Using the *a priori* knowledge that there is ~50% overlap between adjacent frames, the registrations were performed using an efficient subpixel cross-correlation [8] estimating the x and y translations between the frames to within a tenth of a pixel and also the relative piston phase was estimated [8].

To improve the uniformity and accuracy of the mosaic when averaging areas of overlap between frames, we performed a second cross-correlation. Now, instead of cross-correlating each subsequent individual frame with one adjacent neighbor, we performed a cross-correlation in the area of overlap between the single frame and the accumulated frames (the overlap from all neighboring frames), again in a spiral-like pattern. Further improvements in the registration approach may be possible.

The initial mosaic formed by averaging all overlapping frames, but only taking into account a single adjacent frame in the registration process, is shown in Figure 5-4. This full aperture takes into account the translation and phase information from the initial cross-correlations between adjacent frames. The overall mosaic had a blocky, patchwork-like appearance instead of the expected uniform speckle pattern. The darker regions indicate destructive interference between fields from different frames and reveal errors in the piston phase estimates and/or registration errors.

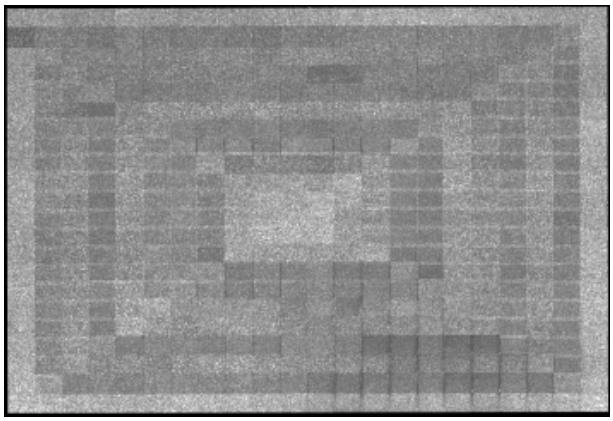

Figure 5-4. Amplitude of the mosaic of 21 x 21 (12,100 by 18,000 pixels) frames after initial cross-correlation of single adjacent frame and averaging overlap regions.

The set of images formed using these initial positions and phases for the mosaic are shown in Figure 5-3(e) – (h). The improvement over a single frame in resolved bars of the USAF target was from (1,1) to (2,4) horizontally and from (1,3) to (2,5) vertically, 5.66 lp/mm and 6.35 lp/mm, respectively.

Figure 5-5 shows the resulting full aperture after both the initial mosaicking and the refinement, clearly showing improved uniformity and demonstrating the need for this refinement. The image after this refined mosaicking is shown in Figure 5-3(i) – (l). We noted a further increase in resolution after this secondary alignment of frames: (3,2) is resolved for horizontal bars and (3,1) is resolved for vertical bars, 8.98 lp/mm and 8.00 lp/mm, respectively.

The mosaicking and registration procedure was repeated after the acquisition of a larger collection of frames for a second, yet independent, synthetic-aperture digital holography aperture. The amplitude for this 32,768 by 32,768 pixel aperture

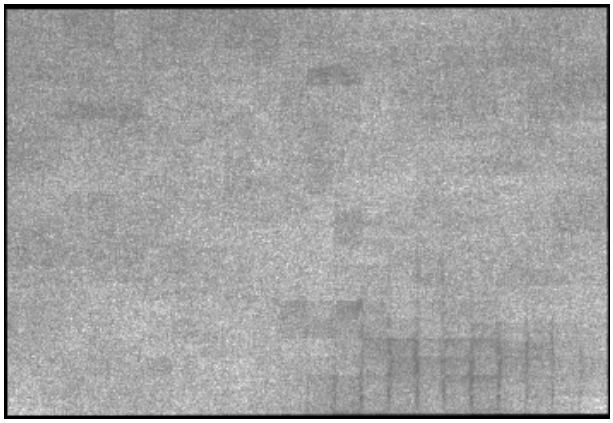

Figure 5-5. Amplitude of the entire 21 x 21 synthetic-aperture (12,100 by 18,000 pixels) after cross-correlation registration of overlapping frame areas.

with initial frame registration and with secondary frame registration is shown in Figure 5-6 and Figure 5-7, respectively. Image reconstruction results for the gigapixel synthetic aperture will be presented in Chapter 6 and 7.

5.4. Summary

We have performed a laboratory experiment to produce a large synthetic-aperture digital hologram. The accurate registration of individual frames within the larger aperture was critical for the desired high-resolution images. The cross-correlation procedures allow us to register individual frames to sub-pixel accuracy as well as correct for piston phase errors between adjacent frames. The results of these complex fields in the aperture plane will be used to reconstruct images using aberration correction techniques, as described in Chapter 6.

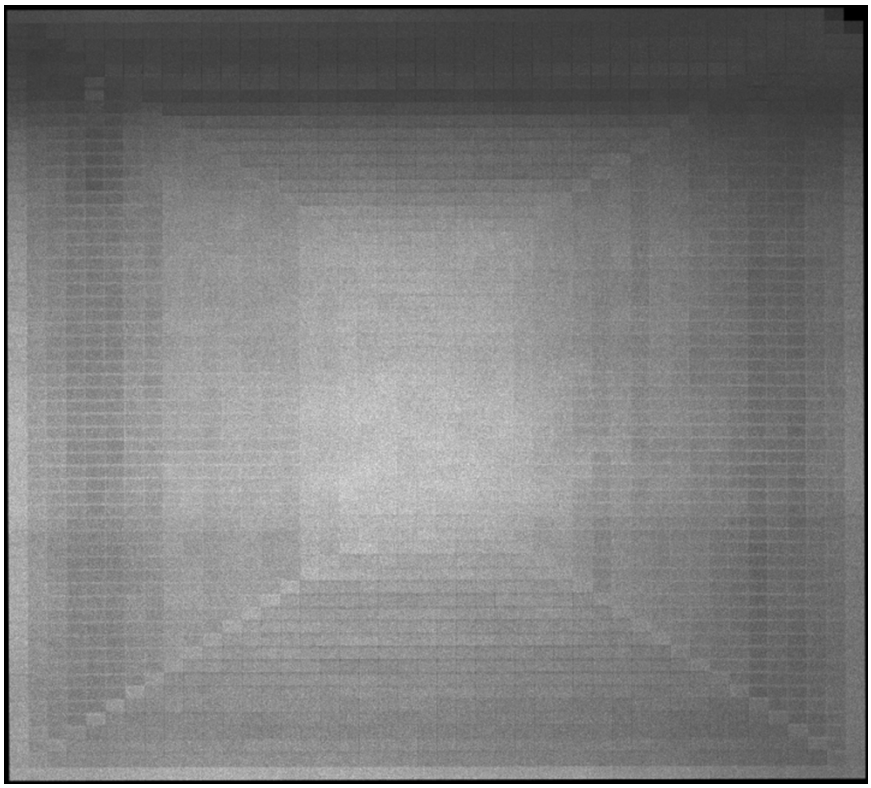

Figure 5-6. Amplitude of the mosaic of 32,768 by 32,768 pixels after initial cross-correlation of single adjacent frame and averaging overlap regions.

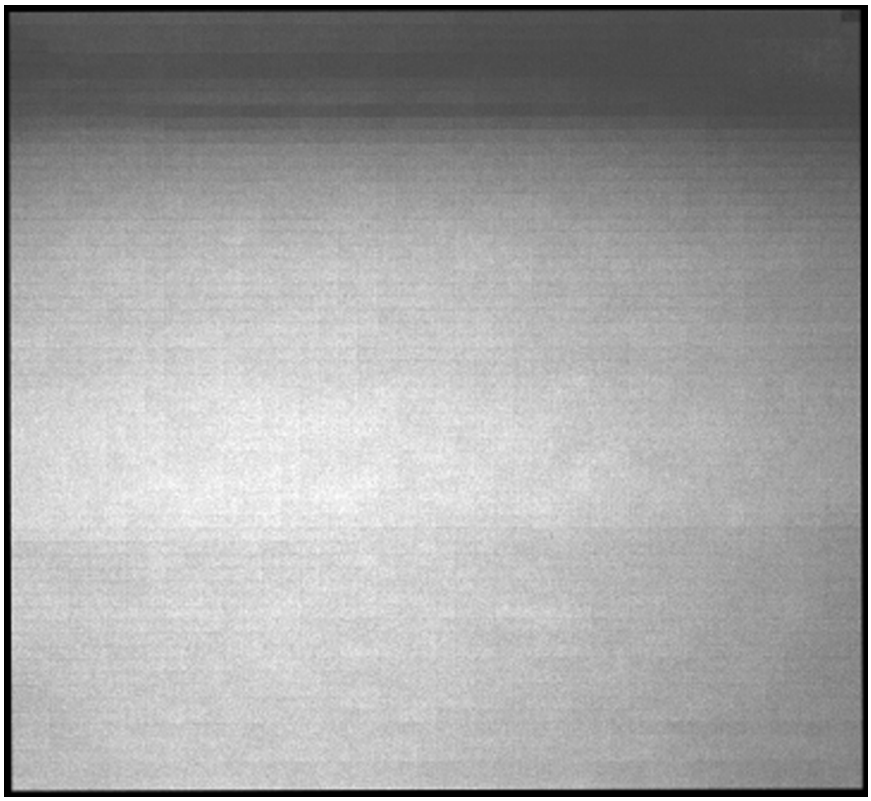

Figure 5-7. Amplitude of 32,768 by 32,768 pixel synthetic aperture after cross-correlation registration of overlapping frame areas.

5.5. References

1. R. Binet, J. Colineau, and J. C. Lehureau, "Short-range synthetic aperture imaging at 633 nm by digital holography," Appl. Opt. **41**, 4775-4782 (2002).

2. J. H. Massig, "Digital off-axis holography with a synthetic aperture," Opt. Lett. **27**, 2179-2181 (2002).

3. D. Claus, "High resolution digital holographic synthetic aperture applied to deformation measurement and extended depth of field method," Appl. Opt. **49**, 3187-3198 (2010).

4. BiSlide Model Specifications. *Velmex, Inc.* Retrieved Jan. 6, 2010, from http://www.velmex.com/bislide/motor_bislide_spec.html

5. A. Kozma and C. R. Christensen, "Effects of speckle on resolution," J. Opt. Soc. Am. **66**, 1257-1260 (1976).

6. A. E. Tippie, A. Kumar, and J. R. Fienup, "High-resolution synthetic-aperture digital holography with digital phase and pupil correction," Opt. Express **19**, 12027-12038 (2011).

7. P. Nisenson, "Speckle Imaging with the PAPA Detector and the Knox-Thompson Algorithm," in *Diffraction-limited imaging* Boston D. M. Alloin, and J.-M. Mariotti, eds. (Kluwer Academic Publishers, 1989), 157-169.

8. M. Guizar-Sicairos, S. T. Thurman, and J. R. Fienup, "Efficient subpixel image registration algorithms," Opt. Lett. **33**, 156-158 (2008).

6. Synthetic-Aperture Image Reconstruction Techniques

6.1. Overview

As the synthetic aperture becomes larger, the system tolerance requirements become more demanding. Without proper knowledge and alignment of frames within the synthetic aperture, residual wavefront errors will occur due to lateral and longitudinal pupil geometry mismatches [1]. Claus [2] used an iterative approach to estimate frame-to-frame phase offsets. To compensate piston aberrations due to a drift in the reference beam (local oscillator) phase relative to the object beam, phase-error correction algorithms are needed. To correct for the axial position of the plane of the object, which may vary in depth across its surface, dynamic focusing must be performed when the object depth exceeds the depth of field. Massig corrected for defocus [3]. Binet *et al.* [4] showed that optical aberrations such as defocus and astigmatism were present after forming an image from a synthetic aperture. Compensation for aberrations in [4] were found manually with user input.

In this chapter, we describe three different approaches to increase the resolution in synthetic-aperture digital holography (SADH). Two of the methods improve resolution by correction for phase aberrations. The third method improves resolution by reducing the speckle noise present in the coherent image reconstructions. Speckle reduction techniques should be used in combination with aberration correction techniques to make the reconstructed image look more like an incoherent image.

Our phase-error correction algorithms require no user intervention to correct frame-by-frame piston errors, reference beam location errors, local focusing errors, and other higher-order errors. We show quantitative results, demonstrating improved image quality upon implementing these techniques. These algorithms also correct for pupil mapping errors which would otherwise cause space-variant aberrations over the aperture for a wide field-of-view and alleviate the tight data collection requirements, making the synthesis of large apertures more practical and affordable.

The first phase-correction approach for improving the resolution of a SADH image borrows concepts found in the synthetic-aperture radar literature [5] and the extended-scene Shack-Hartmann (SH) wavefront sensor literature [6, 7], and applies them to this work in digital holography. To our knowledge, this is the first use of sub-aperture translation measurements in combination with a modal reconstructor algorithm to correct for phase aberrations in digital holography. The second method to correct for aberrations utilizes an image sharpening technique described in previous chapters. With this technique, we are able to correct for the experimental system aberrations allowing for diffraction-limited resolution. Diffraction-limited resolution images for digital holography synthetic apertures of this scale have not been previously reported, and we believe this is a significant contribution to on-going work in digital holography.

6.2. Sub-aperture Approach

6.2.1. Introduction to Sub-aperture Approach

Sub-aperture techniques for correcting phase errors involve dividing an aperture into a number of sub-apertures, forming an image from each, and cross-correlating the intensity images with one another to determine their relative shifts. Local linear phase errors are determined from the shifts and combined to estimate smooth phase errors across the entire aperture. In synthetic-aperture radar, this is known as the map-drift algorithm [6, 7], where the cross correlations are performed between lower-resolution speckled intensity images and the phase errors are one dimensional. In optical testing by extended-scene Shack-Hartmann wavefront sensors, the cross correlations are performed in two dimensions between low-resolution images of an incoherent object [5]. The use of a "virtual SH" has been applied in microscopy [6, 7] for point-like objects. We extend these techniques to digital holography of an extended object using a correlation-based method to calculate translations between speckled images from sub-apertures and estimate 2-D phase errors.

6.2.2. Algorithm Implementation

For digital holography phase-error correction using a sub-aperture implementation, we divided a 9,076 x 13,251 pixel full aperture into M x M sub-arrays, where $M = 7$. For this experiment, the sub-arrays were created by masking out a square region that was $N/M = 1296$ pixels, where N is the number of pixels in the shorter dimension of the array. We chose the center sub-array to produce the reference image frame for calculating the translations with respect to every other sub-array image. Each sub-

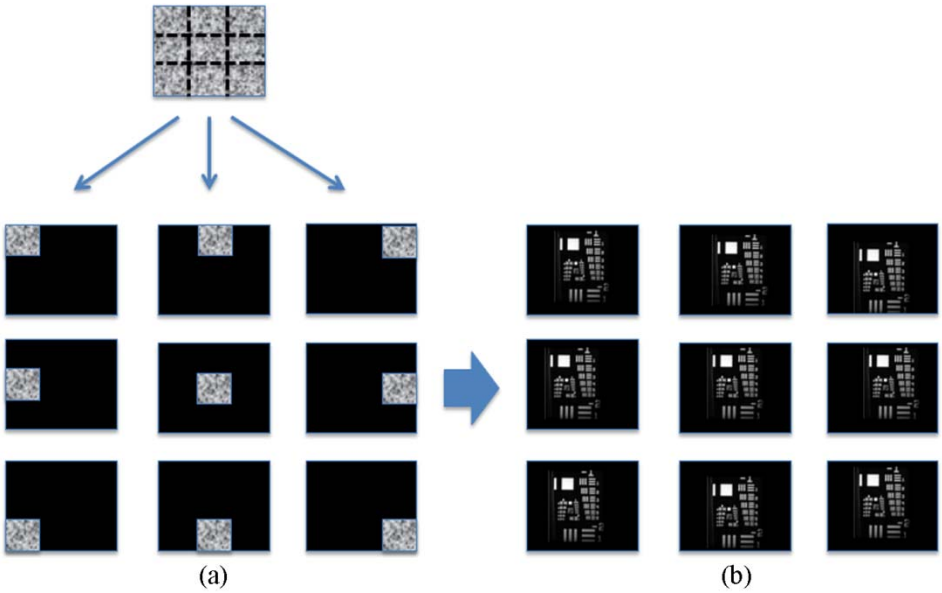

Figure 6-1. Schematic describing sub-aperture implementation. (a) Full aperture array is divided into sub-arrays, and (b) each sub-array is propagated to the image plane where they are cross-correlated.

array field will contain a different speckle realization of the image. To reduce errors in the registration due to speckles of differing images, we lowpass filtered the intensity image from each sub-array with a Gaussian filter with a standard deviation of 25 pixels.

Different methods exist to determine the translations between sub-aperture images, such as maximum-likelihood estimation and deconvolution [8], but the most widely used are cross-correlation techniques. Different implementations of cross-correlation algorithms have been developed such as an adaptive cross-correlation [6], minimization of a mean-squared-error [7], or periodic correlation [6]. For this work, we used an efficient sub-pixel cross correlation technique [9] where a 1.5 x 1.5 pixel region about the initial estimate of the peak is upsampled by a factor κ (κ = 10)

using a single discrete Fourier transform (DFT). The translations $t_{x,m}$ and $t_{y,m}$ (in pixels) may be converted to wavefront slope by [9]

$$s_{x,m} = k\frac{t_{x,m}\Delta x}{z} \quad \text{and} \quad s_{y,m} = k\frac{t_{y,m}\Delta x}{z} \tag{6.1}$$

where $k = 2\pi/\lambda$, Δx = 7.2 μm is the pixel pitch of the detector and z = 3.315 m is the distance between the object plane and detector.

We use a non-iterative modal reconstruction algorithm [10] to compute the expansion coefficients from the wavefront slope measurements. The polynomial expansion of the wavefront aberration $\phi(x,y)$ can be written as

$$\phi(x,y) = \sum_{j=1}^{J} c_j \psi_j(x,y) \tag{6.2}$$

where c_j are the expansion coefficients and $\psi_j(x,y)$ are the polynomial basis functions. We used Zernike-like basis functions orthonormalized over a rectangular aperture. The expansion coefficients of the wavefront can be computed from the wavefront slopes as a result of the orthogonality of the set of basis functions $\{\psi_j\}$ as

$$c_j = \sum_{m=1}^{M}\left[s_{x,m}\frac{\partial \psi_j(x_m,y_m)}{\partial x} + s_{y,m}\frac{\partial \psi_j(x_m,y_m)}{\partial y}\right]. \tag{6.3}$$

This formulation of the expansion coefficients gives the analytical solution based on the slopes and the partial derivatives of the basis functions. Using this approach, we corrected up to 7th order wavefront errors, 36 coefficient terms in 2-D.

Once the wavefront aberration was calculated from the slope measurements, the phase $\phi(x, y)$ was subtracted from the total complex speckle field $G(x, y)$ in the detector plane of the hologram and then propagated a distance z using angular spectrum to the image plane.

6.2.3. Experimental Results

The wavefront correction compensated for system phase errors such as reference beam location errors, focusing errors, and up to 7th order errors that may have resulted from the mosaicking of the synthetic aperture. The wavefront correction having a peak-to-valley of 2.3 waves and an rms of 0.44 waves after using a modal reconstructor on the wavefront slopes as shown in Figure 6-2. Global phase errors

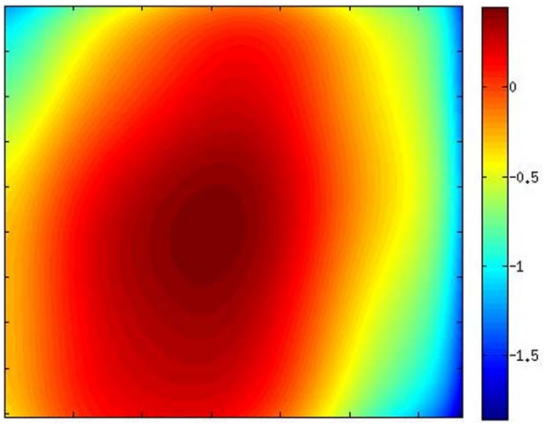

Figure 6-2. 7th order wavefront correction using wavefront slope measurements from virtual Shack Hartmann. Units are in waves. Width is 9,076 x 13,251 pixels.

across the array are corrected, but additional higher order terms would be needed to correct frame-by-frame errors. Figure 6-3 shows the reconstructed images from the synthetic aperture with and without phase correction provided by the sub-aperture technique. Without wavefront correction, the finest resolvable bars of the USAF bar target were (group, element) (2,3) for horizontal bars and (2,1) for vertical bars, 5.04 lp/mm and 4.00 lp/mm, respectively. After correcting for phase errors using this approach, horizontal bars up to (3,1) and vertical bars up to (3,3) could be resolved, 8.00 lp/mm and 10.10 lp/mm, respectively — about a factor of two in resolution.

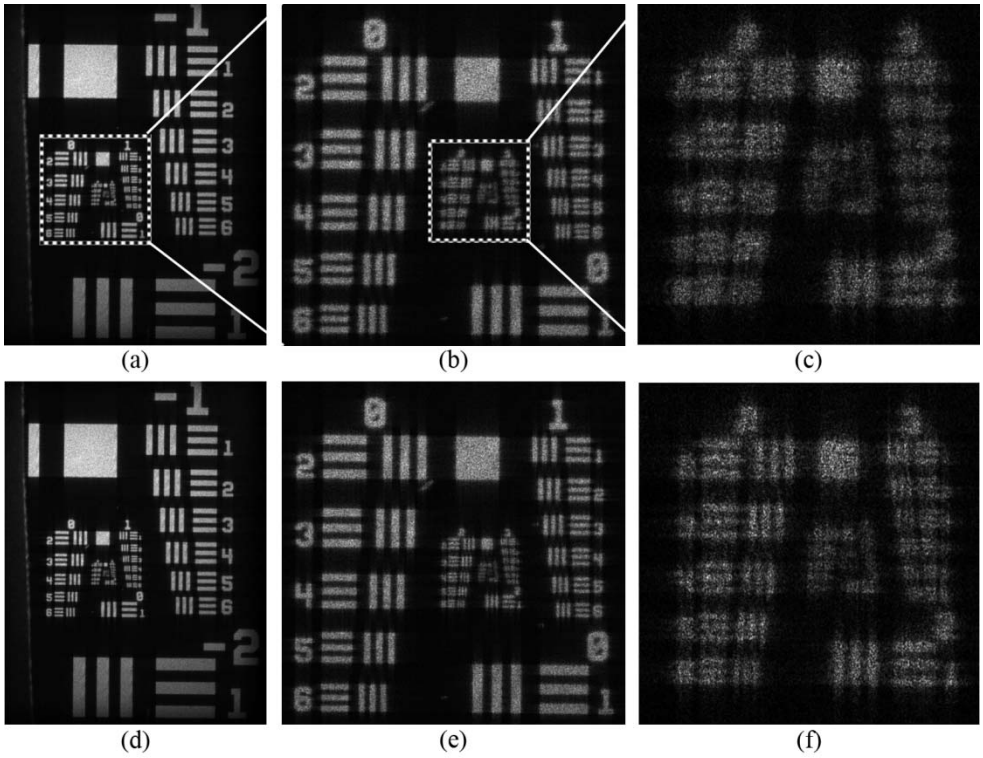

Figure 6-3. Reconstructed image (a) – (c) without wavefront correction and (d) – (f) with sub-aperture phase correction technique. Insets of images are shown to observe fine details; Column 1 - 8236 x 6320 pixels, Column 2 – 2540 x 2540 pixels, Column 3 – 720 x 720 pixels

These results show that this wavefront sensing technique can be applied to the correction of 2-D phase errors present in synthetic aperture digital holography with speckled images of extended objects with a single speckle realization

6.3. Sharpness Maximization Approach

The full-aperture complex field from the object in the detector plane was used to reconstruct the fine-resolution, wide-field-of-view image. We applied phase correction techniques to the field to compensate for residual phase errors that remain after the piston phase correction performed during mosaicking. Three phase correction algorithms we used were correcting (i) the location of the reference point source, (ii) residual higher-order phase errors, and (iii) local region phase errors due to variations in axial depth.

6.3.1. Reference Correction

The complex field retrieved in the detector plane after windowing out other hologram terms is $G(x,y) = F(x,y)R^*(x,y)$. We wish to divide out the complex conjugate of the reference field, $R^*(x,y) = \exp\left[-i\phi_r(x,y)\right] = \exp\left[-ikr(x,y)\right]$ (ignoring the reference amplitude), where $\phi_r(x,y) = kr(x,y)$ is the phase correction due to the reference source location applied at the detector plane,

$$r(x,y) = \sqrt{(x-\xi_r)^2 + (y-\eta_r)^2 + z_r{}^2}, \tag{6.4}$$

and (ξ_r, η_r, z_r) is the position of the reference point source and $k = 2\pi/\lambda$. Because a Fresnel transform is insufficiently accurate for this wide-aperture, wide field-of-view image, we used angular spectrum propagation of $G(x,y)$ to the image plane, given by

$$\begin{aligned} f(\xi,\eta) &= FT^{-1}\left\{ FT\left\{ G(x,y)\exp\left[ikr(x,y)\right]\right\}\exp\left(-i2\pi z\sqrt{1/\lambda^2 - f_x^2 - f_y^2}\right)\right\} \\ &\equiv \mathcal{A}\left\{-z; G(x,y)\exp\left[ikr(x,y)\right]\right\} \end{aligned} \tag{6.5}$$

where z is the distance from the image plane to the detector plane and $FT\{\bullet\}$ denotes a Fourier transform. We found that our measurement of the reference source location was insufficiently accurate, leading to residual aberrations. To determine and correct that error, we maximized the sharpness of the image [11]

$$S_1 = \sum_{\xi,\eta} I^{\beta}(\xi,\eta) = \sum_{\xi,\eta}\left(\left|f(\xi,\eta)\right|^2\right)^{\beta} \tag{6.6}$$

as a function of the reference source location, where $I(\xi,\eta)$ is the intensity of the image and β is a scalar quantity. (If $\beta < 1$, then we would maximize $-S_1$.) For this work, we used a value of $\beta = 0.6$ which is favorable for the case of a single speckle realization [12, 13]. We implemented this using a conjugate gradient nonlinear optimization routine using analytic gradients of S with respect to the three-dimensional coordinate position of the reference point source. Derivations of these analytic gradients can be found in Appendix 6.5. Figure 6-4(a) – (d) shows the

reconstructed image after optimizing and correcting for the reference point source location. The resolvable bars after the appropriate reference wavefront were (3,2) for horizontal bars and (3,3) for vertical bars. The increase in resolution can be observed by comparing Figure 6-4 with the same mosaic before correction, shown in Figure 5-3, for which the resolvable bars were (2,3) for the horizontal and (2,1) for the vertical bars.

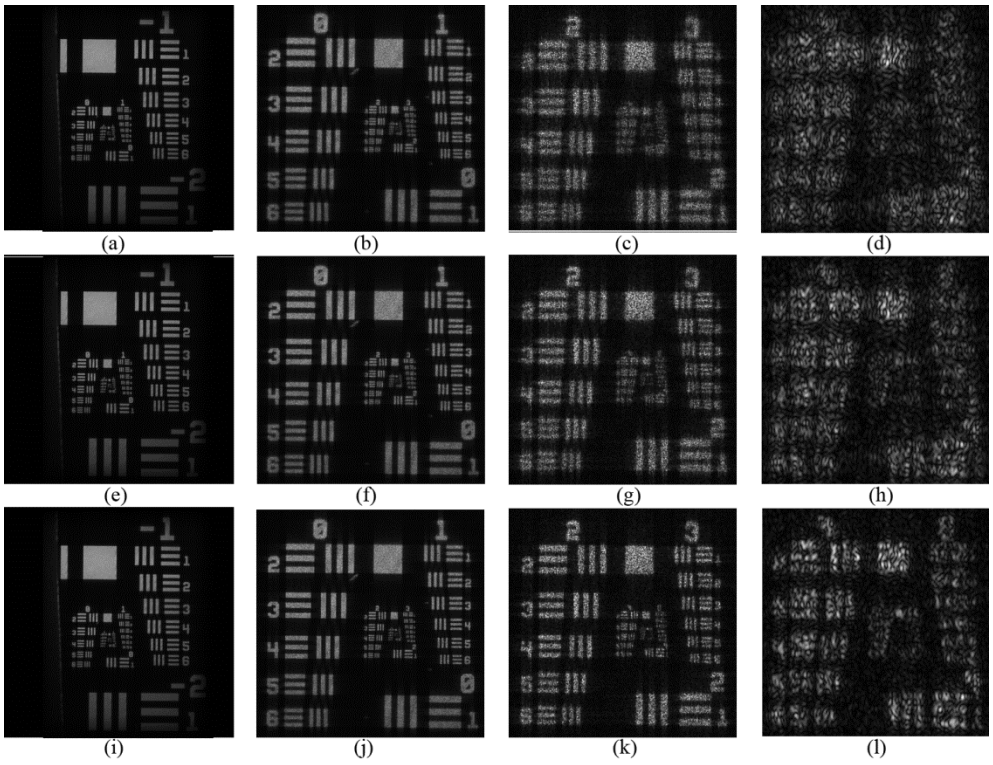

Figure 6-4. Image reconstruction of (a) – (d) reference phase correction; (e) – (h) higher order phase correction over entire FOV; (i) – (l) higher order phase correction over ROI using M_2. Column 1 – 8700 x 6500 pixel area of entire image; Column 2 – 2550 x 2500 pixel subset of Col. 1; Column 3 – 650 x 650 pix subset of Col 2; Column 4 – 160 x 160 pixel subset of Col 3.

6.3.2. Higher-order Phase-error Correction

In addition to applying a phase correction that specifically corrects for wavefront errors related to the reference source, we found it necessary to include an additional step to correct for other phase errors in the system. This may correct any residual errors from the mosaicking process, focus correction to locate the plane of best focus for the image, etc. We model the complex field in the detector plane after reference correction, as

$$G(x,y) = G_i(x,y)\exp\left[i\phi(x,y)\right] \tag{6.7}$$

where $G(x,y)$ is the complex field with phase errors, $G_i(x,y)$ is the ideal field and $\phi(x,y)$ is the residual phase error. We found the $\phi(x,y)$ that maximizes the sharpness of the image using a conjugate gradient search over $\phi(x,y)$ using the analytic gradient of $\partial S/\partial\phi$ [14].

For this residual phase correction, we used the method of sieves [15], in which we convolve the point-by-point version of the analytic gradient with a Gaussian kernel. Important for dealing with very large arrays, the method of sieves requires less computational time and memory storage than optimizing over coefficients of polynomial expansions of the phase estimates, which need storage of polynomial basis functions for efficiency. Using a bootstrapping method, we started with a kernel having a standard deviation of 2500 pixels and reduced the size of the Gaussian kernel every five iterations (i.e. 2500, 2000, 1500, 1000, 500, 250), ending

with a final kernel with a standard deviation of 250 pixels. This allows the algorithm to first optimize over larger, lower-frequency global phase errors and then eventually correct for phase errors that are more local on a frame-by-frame basis, allowing for only smooth phase maps and avoiding stagnation during the optimization process. Visible in Figure 6-5, which shows the phase error estimate after maximizing the sharpness of the image, are both low-order focus correction and individual-frame higher- order correction. An important thing to note is that the sieves method of sharpness optimization had no explicit knowledge of the acquisition or mosaicking procedures; by optimizing the sharpness in the image plane, the algorithm was able to estimate a phase error that shows characteristics that are consistent with the frame-by-frame nature of the data in the detector plane. Figure 6-4(e) – (h) shows the further improved image after this phase correction is applied; horizontal bars (3,5) were resolved, as were vertical bars (3,5).

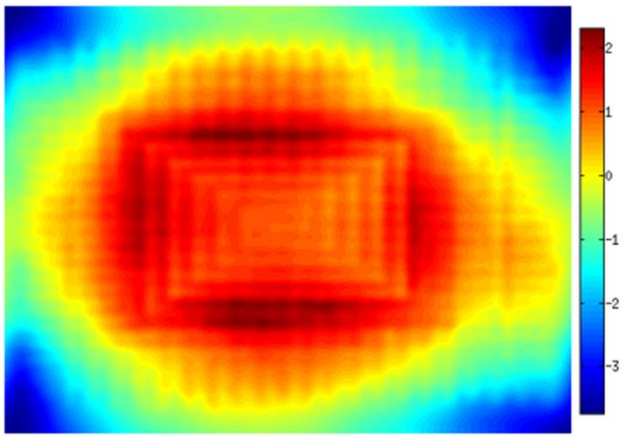

Figure 6-5. Higher order phase correction over the entire FOV. Colorbar units in radians.

6.3.3. Region-of-interest Phase Correction

A phase-error correction applied over the entire field of view sharpens the image to the plane of overall best focus correction. For the experimental case presented here, varied defocus over a wide field-of-view object is likely since the depth of field is $DOF = 2\lambda\left(z/D\right)^2 =$ 680 μm, so even a planar object having a small tilt can have appreciable depth. The depth of field would not be an issue for long-range imaging, but it was a problem in our laboratory experiment on account of the relatively large angle (2.3 degrees) subtended by the synthetic aperture. It is possible, however, to apply a phase correction that is optimized for a specific object depth by selecting a region of interest (ROI).

For ROI phase correction, the field in the detector plane was first numerically propagated to the nominal image plane. A mask was applied in the image plane to window out the specific ROI and the windowed field was then propagated back to the detector plane. This field, G_{ROI}, can be written in terms of the original field as

$$G_{ROI} = \mathcal{A}\left\{z; M_n\left(\xi,\eta\right)\mathcal{A}\left[-z; G\right]\right\} \tag{6.8}$$

where $\mathcal{A}\left[z; G\right]$ is the angular spectrum propagation of the field G by a distance z and M_n is a mask defining the n^{th} ROI. G_{ROI} was then used in the sharpness minimization routine described above. The ROI selected for this example was a 600 x 600 pixel region and the mask was a square with a weighted cosine tapering function of 24 pixels applied to the edge of the region. M_1 included two horizontal

bars from Group –1, Element 1, and M_2 encompassed Group 2 and higher as shown in Figure 6-6. After finding the phase that minimizes the sharpness of a ROI, we corrected the entire synthetic aperture for that phase error, and the corrected field was then propagated using angular spectrum to the image plane.

Figure 6-7 shows the phase-error maps for the two ROI sharpness optimizations. Compared with Figure 6-5, where the phase correction exhibited both global phase errors as well as frame-by-frame correction, the primary phase corrections seen by the ROI M_1 and M_2 phase estimate are smooth higher-order

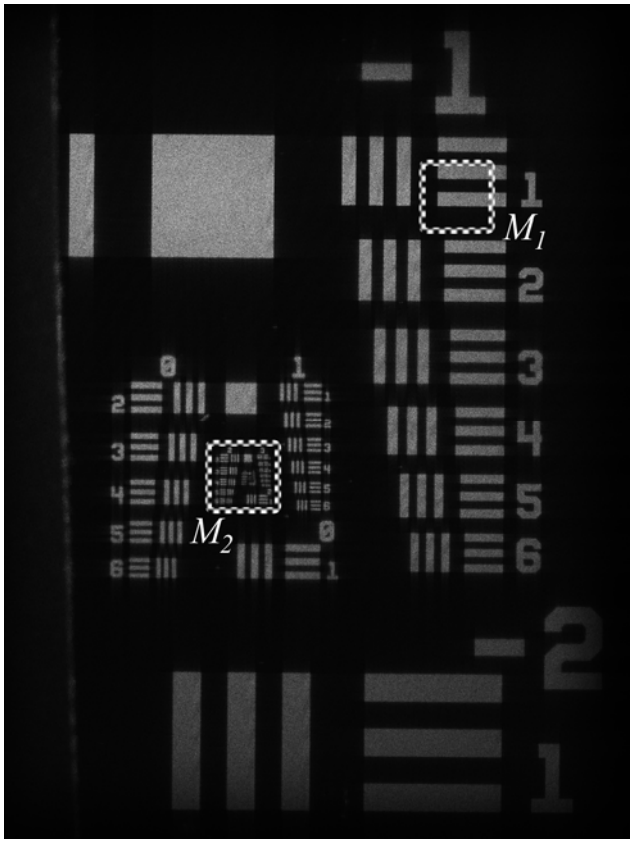

Figure 6-6. Entire FOV with 600 pixel masked regions, *M_1 and M_2*, shown in dashed squares.

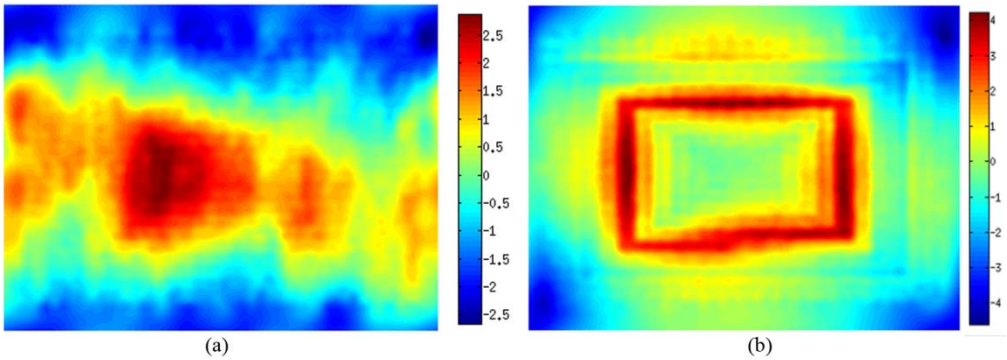

Figure 6-7. Higher order phase correction (a) using M_1 and (b) using M_2. Colorbar units in radians.

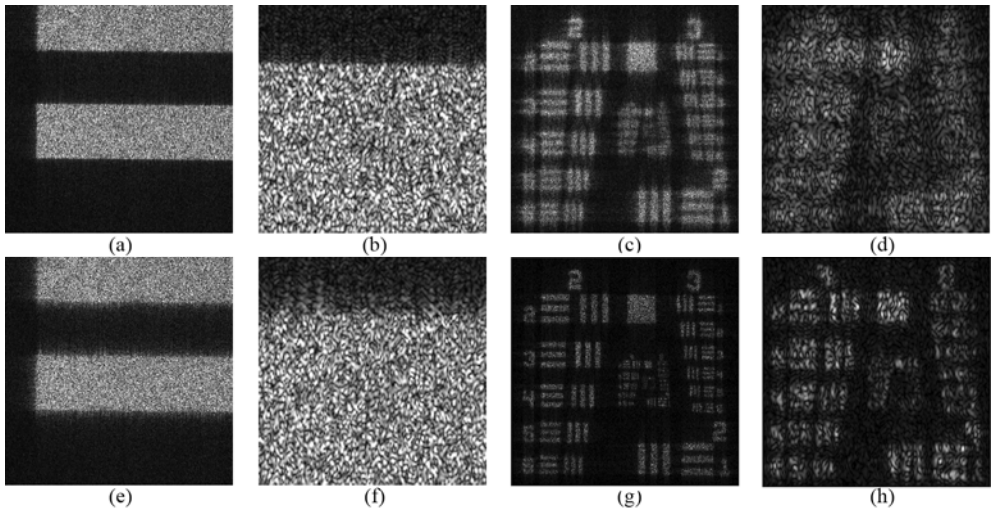

Figure 6-8. Image reconstruction with ROI higher-order phase correction (a) – (d) using mask M_1 and (e) – (h) using mask M_2. Subimages (b) and (f) are 160 pixel areas of (a) and (e), respectively and (d) and (h) are 160 pixel subsets of the central areas of (c) and (g).

errors. For the image reconstructions, this ROI phase estimate replaces the phase estimate found by utilizing the entire FOV. A comparison between the images resulting from these two different phase corrections is shown in Figure 6-8. From Figure 6-8(b) and (h), we see that the ROI phase estimates do improve and sharpen

the image within the masked region. From Figure 6-8(d) and (f), we also see that areas far from the ROI mask were blurred due to space-variant errors, presumably due to a tilted plane or residual errors in the reference location.

The image reconstruction using M_2 as a selective ROI is shown in Figure 6-4 (i) – (l). The resolution increase is substantial in comparison to our previous, intermediate images. For the reference-only phase correction, the finest resolved bars in Figure 6-4 (a) – (d) were (Group, Element) (3, 2) for horizontal bars. We saw a modest improvement to (3, 5) horizontally resolved bars after the entire higher order correction over the entire field-of-view. However, for the ROI phase correction, the resolution increased an entire group (by a factor of two), with the finest resolved horizontal bars now (4,2) and vertical bars (4, 5). This corresponds to 17.9 line-pairs (lp) per mm and 25.4 lp/mm, respectively, equivalent to a resolution of 56 μm and 39 μm, respectively.

The final size of this synthetic aperture was 12,100 by 18,000 pixels (89 mm by 133 mm), about 200 megapixels. The theoretical image resolution, given by $\lambda z/D$, where D is the synthetic aperture width, is 19.5 μm horizontally and 13.1 μm vertically. Since no speckle averaging has been performed, the expected resolution for a speckled image of a diffuse object will be reduced [16, 17]. For a USAF bar target, we found that the resolution of a speckled image of three-bar target degrades by about a factor of three. Therefore, the expected resolution of the synthetic aperture used in this experiment is 59 μm for horizontal bars and 39 μm for vertical bars,

consistent with our experimental results. Further experiments were performed to produce a gigapixel image using these techniques, as described in Chapter 7.

6.3.4. Computational Requirements

The computational requirements are quite demanding for mosaicking, phase-error correction and image formation for such a large synthetic aperture. An ordinary desktop computer having a few GB of RAM cannot handle everything in fast memory necessary for efficient computations for such large arrays of data. For the computations performed in this experiment, an IBM x3755 server with four AMD Opteron 8224 SE processors and 128 GB of memory was used. The computation time for calculating initial cross-correlations between adjacent frames was 17.9 minutes. The mosaicking of the synthetic aperture took 9 hours and 19 minutes and the phase-error estimation took roughly 3 days of computational processing. Parallel implementation using a distributed system for the propagation kernel [18] would be one way to reduce the computation time for the reconstruction process.

6.4. Speckle-Reduction Approach

Another approach to further pushing the achievable resolution is to apply speckle averaging. One of the drawbacks of coherent imaging is the effect of speckle, which reduces the effective spatial resolution of the image [19]. Baumbach ***et al.*** showed how laterally shifted holograms can be averaged to create speckle reduced images [20]. We divided a gigapixel aperture into four quadrants, performed image sharpening over a small region-of-interest (ROI) to achieve the highest possible

resolution in that ROI for each quarter-gigapixel dataset, and then formed a speckle-averaged image with the four independent speckle realizations. Figure 6-9 shows a single quarter-gigapixel image reconstruction before and after phase correction. The finest resolved bars horizontally were (4,2) and vertically (4,1).

Figure 6-10 shows the result of a phase-corrected, speckled-reduced image from a gigapixel-sized array of collected holography data. The resolution increased (4,4) in the horizontal direction and (4,5) in the vertical direction. We observed an approximately 1.33x increase in the resolution of the image compared to a single quarter-gigapixel image. By decreasing the effect of aberrations in the image using an image sharpening approach to correct higher order phase errors present in the image in combination with a reduction in the speckle noise inherent in coherent imaging systems, we have shown improved image resolution.

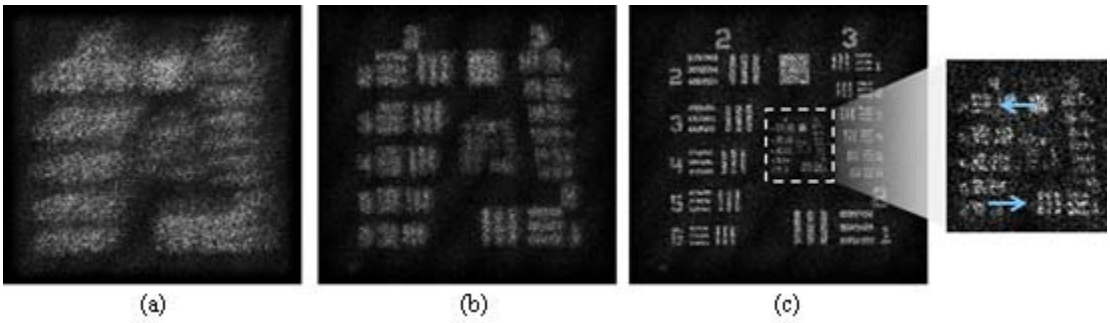

Figure 6-9. Portion of USAF bar target showing fine resolution bars reconstructed from a quarter-gigapixel synthetic aperture. (a) Image before phase correction, (b) image after focus correction and (c) image after higher-order phase correction.

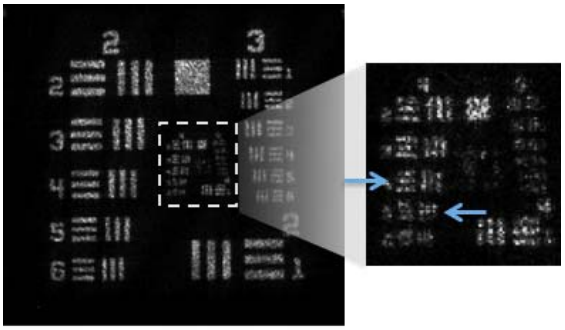

Figure 6-10. Portion of USAF image formed using gigapixel data (four quarter-gigapixel arrays) after phase correction and speckle averaging.

6.5. Appendix: Derivation of Analytic Gradient of S

The field obtained by angular spectrum propagation of $G(x,y)$ to the image plane is given by Eq. (6.5). The partial derivative of the sharpness metric *S* given in Eq. (6.6), with respect to the *x*-component of the reference point source location ξ_r, is given by

$$\begin{aligned}\frac{\partial S}{\partial \xi_r} &= -\sum_{\xi,\eta} \beta\left[I^{\beta-1}(\xi,\eta)\right]\frac{\partial I}{\partial \xi_r} \\ &= \sum_{\xi,\eta} \beta I^{\beta-1}(\xi,\eta)\frac{\partial f(\xi,\eta)\, f^*(\xi,\eta)}{\partial \xi_r} \\ &= \sum_{\xi,\eta} \beta I^{\beta-1}(\xi,\eta)\, 2\,\mathrm{Re}\left[f^*(\xi,\eta)\frac{\partial f(\xi,\eta)}{\partial \xi_r}\right].\end{aligned} \tag{6.9}$$

Additionally, $\partial f(\xi,\eta)/\partial \xi_r$ can be written as

$$\frac{\partial f(\xi,\eta)}{\partial \xi_r} = \mathcal{A}\left\{-z; G(x,y)\exp\left[ikr(x,y)\right]\frac{-ik(x-\xi_r)}{r(x,y)}\right\}. \tag{6.10}$$

Using Eq. (6.10) we can write Eq. (6.9) as

$$\frac{\partial S}{\partial \xi_r} = \sum \beta I^{\beta-1}(\xi,\eta)\, 2\,\mathrm{Re}\left[\mathcal{A}\left\{-z; G(x,y)\exp\left[ikr(x,y)\right]\right\}^{*} \times \mathcal{A}\left\{-z; G(x,y)\exp\left[i\phi(x,y)\right]\frac{-ik(x-\xi_r)}{r(x,y)}\right\}\right] \tag{6.11}$$

and similarly for $\partial S/\partial \eta_r$, replacing $(x-\xi_r)$ by $(y-\eta_r)$, and similarly for z_r, replacing $(x-\xi_r)$ by $-z_r$.

6.6. References

1. L. D. Weaver, J. S. Fender, and C. R. Dehainaut, "Design considerations for multiple telescope imaging arrays," Opt. Eng. **27**, 730-735 (1988).

2. D. Claus, "High resolution digital holographic synthetic aperture applied to deformation measurement and extended depth of field method," Appl. Opt. **49**, 3187-3198 (2010).

3. J. H. Massig, "Digital off-axis holography with a synthetic aperture," Opt. Lett. **27**, 2179-2181 (2002).

4. R. Binet, J. Colineau, and J. C. Lehureau, "Short-range synthetic aperture imaging at 633 nm by digital holography," Appl. Opt. **41**, 4775-4782 (2002).

5. W. G. Carrara, R. S. Goodman, and R. M. Majewski, *Spotlight synthetic aperture radar : signal processing algorithms,* (Artech House, Boston, 1995).

6. L. A. Poyneer, "Scene-based Shack-Hartmann wave-front sensing: analysis and simulation," Appl. Opt. **42**, 5807-5815 (2003).

7. E. Sidick, J. J. Green, R. M. Morgan, C. M. Ohara, and D. C. Redding, "Adaptive cross-correlation algorithm for extended scene Shack-Hartmann wavefront sensing," Opt. Lett. **33**, 213-215 (2008).

8. A. E. Tippie, A. Kumar, and J. R. Fienup, "High-resolution synthetic-aperture digital holography with digital phase and pupil correction," Opt. Express **19**, 12027-12038 (2011).

9. M. Guizar-Sicairos, S. T. Thurman, and J. R. Fienup, "Efficient subpixel image registration algorithms," Opt. Lett. **33**, 156-158 (2008).

10. M. C. Roggemann and B. Welsh, *Imaging through turbulence,* (CRC Press, Boca Raton, 1996).

11. E. Acosta, S. Bara, M. A. Rama, and S. Rios, "Determination of phase mode components in terms of local wave-front slopes – an analytical approach," Opt. Lett. **20**, 1083-1085 (1995).

12. R. A. Muller and A. Buffington, "Real-time correction of atmospherically degraded telescope images through image sharpening," J. Opt. Soc. Am. **64**, 1200-1210 (1974).

13. S. T. Thurman and J. R. Fienup, "Correction of anisoplanatic phase errors in digital holography," J. Opt. Soc. Am. A **25**, 995-999 (2008).

14. S. T. Thurman and J. R. Fienup, "Phase-error correction in digital holography," J. Opt. Soc. Am. A **25**, 983-994 (2008).

15. A. E. Tippie and J. R. Fienup, "Phase-error correction for multiple planes using a sharpness metric," Opt. Lett. **34**, 701-703 (2009).

16. U. Grenander, *Abstract inference,* (Wiley, New York, 1981).

17. A. E. Tippie and J. R. Fienup, "Multiple-plane anisoplanatic phase correction in a laboratory digital holography experiment," Opt. Lett. **35**, 3291-3293 (2010).

18. A. Kozma and C. R. Christensen, "Effects of speckle on resolution," J. Opt. Soc. Am. **66**, 1257-1260 (1976).

19. A. J. Page, L. Ahrenberg, and T. J. Naughton, "Low memory distributed reconstruction of large digital holograms," Opt. Express **16**, 1990-1995 (2008).

20. T. Baumbach, E. Kolenovic, V. Kebbel, and W. Juptner, "Improvement of accuracy in digital holography by use of multiple holograms," Appl. Opt. **45**, 6077-6085 (2006).

7. Synthetic Aperture Digital Holography: Alternative Propagation and Aberration Correction Algorithm

7.1. Introduction

In digital holography, one may sense an optical field in a plane (such as a pupil plane) other than an image plane, and then one must numerically propagate the field to a plane conjugate to the object plane to form an image. Numerical propagation techniques are important for digital holography and other areas such as wavefront sensing by phase retrieval and optical system modeling.

7.1.1. Propagation Methods

Various methods have been described for digital propagation including: single-Fourier transform Fresnel propagation [1], convolution-based Fresnel propagation by Fourier transforms [2], angular spectrum propagation [3], FFT-based integration of the Rayleigh-Sommerfeld diffraction equation [4], and direct integration of the Rayleigh-Sommerfeld integral [5]. Which of these approaches to propagation is best to use depends on the imaging scenario. Physical parameters such as pixel pitch, detector array size, object size, imaging distance, etc., and other factors such as desirability of equal pixel spacing in each plane, size of computational arrays, processing time, and required accuracy impact the choice of propagator. The angular spectrum (AS) method preserves pixel spacing in each plane whereas the Fresnel propagator does not. The use of fast Fourier transforms (FFTs) is very important for computational speed; Fresnel propagations require only one FFT, while AS requires

two FFTs. Direct evaluation of the Rayleigh-Sommerfeld diffraction integral (using no FFTs) is extremely slow compared with FFT-based methods. Fresnel propagation employs the paraxial approximation whereas AS propagation and direct integration of the Raleigh-Sommerfeld diffraction formulas are not limited to the paraxial regime, and are exact for scalar wave propagation except for sampling and possible aliasing effects.

7.1.2. Application to Synthetic-Aperture Digital Holography

The work described here is motivated by synthetic-aperture digital holography (SADH) [6-10]. A diagram for the experimental setup for a SADH is shown in Chapter 5, Figure 5-1. A number of laterally translated digital holograms are measured, and the collection of individual digital holographic frames are mosaicked together to form a larger aperture. A synthetic aperture allows for an increased numerical aperture, resulting in the collection of higher spatial frequencies and improved image resolution. The total space-bandwidth product of the image is increased proportionally.

Issues such as registering overlapping portions of adjacent frames [6] and handling experimental higher-order phase aberrations [10] have been addressed in the literature; our techniques to deal with these issues have been presented in Chapter 6. As a result of researchers working through some of these practical experimental considerations, the size of synthetic apertures has continued to increase from early work with synthetic apertures of 1.3 Mpix [6] to our current synthetic apertures that are gigapixel in size [11]. The increase in numerical aperture due to an increased

aperture size caused the paraxial approximations to be no longer applicable to the imaging conditions of our laboratory experiments [11]. We have developed new methods that simultaneously address both the numerical propagation and phase aberrations associated with these non-paraxial fields for gigapixel SADH.

7.1.3. Nonparaxial Propagation in SADH

Although a logical choice for non-paraxial numerical propagation would seemingly be the AS propagator, there are still sampling issues that may be encountered that necessitate the development of different numerical propagation approaches. As discussed in [3, 11], to avoid aliasing in the AS propagation for this SADH experiment, we argue that the condition for the maximum detector pixel pitch to be

$$\Delta x_{\max} = \frac{\lambda z}{D + w} \tag{7.1}$$

where λ is the wavelength, z is the propagation distance, D is the width of the synthetic aperture and w is the width of the object. Eq. (7.1) indicates that the sampling conditions depend on the extent of both the object field and the hologram field. The angular extent θ_w of the object, as seen by any one point on the detector, is equal to $\theta_w = w/z$ in the small-angle approximation and is about the same at $\xi = 0$ and $\xi = D/2$, as shown in Figure 7-1. However, for different points in the hologram, the angle of the center of the object changes. We note that the angle for the center of the object changes by $\theta_D = D/z$ (again for the small-angle approximation).

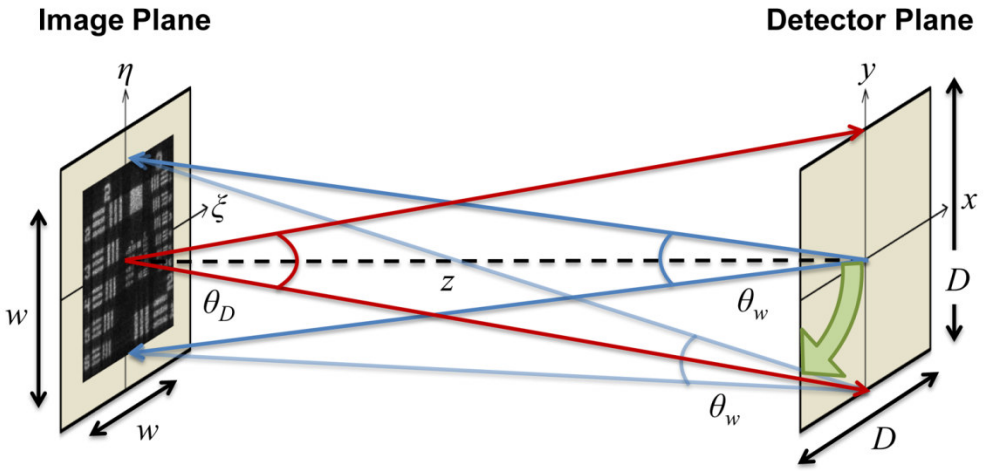

Figure 7-1. Angle subtended by image at different points on the detector plane. Width of object/image, *w;* width of detector, *D*.

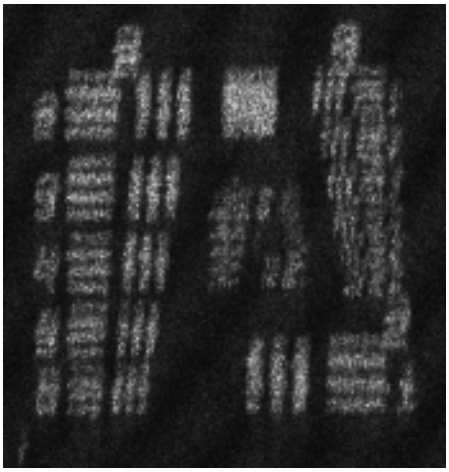

Figure 7-2. Example of ghosting artifacts in a small region of a gigapixel hologram image from undersampled hologram data.

Therefore, in order to capture the entire spatial frequency content of the image, both the angular extent of the object and the angular extent of the hologram must be considered. If not properly sampled, aliasing occurs, resulting in ghosting [11] upon propagation to the image plane, as shown in Figure 7-2. The sampling condition was

violated based on our gigapixel experimental parameters: D = 24.2, cm, w = 13.2 cm, z = 3.31 m, and λ = 514 nm, for which Eq. (7.1) gives the sampling of $\Delta x_{\max} = 4.5$ μm, compared to the actual detector pixel pitch of 7.4 μm.

We sought to avoid some of the limitations imposed by this sampling condition for use in large-aperture, high-spatial-bandwidth SADH and provide alternatives that would alleviate the tight sampling conditions noted here. The method that we propose for non-paraxial imaging is the commonly used Fresnel propagator, but correcting for anisoplanatic phase errors due to the Fresnel approximation as well as unknown experimental phase errors, allowing for high-resolution image reconstructions.

7.2. Image Aberrations: Theory

In this section we seek to describe two types of aberrations present in imaging with Fresnel propagators in a non-paraxial SADH experiment. The first source of aberrations is that resulting from the use of the Fresnel approximation; the second is due to uncertainties in the experiment itself.

7.2.1. Paraxial Imaging

Both we and previous authors in the SADH literature have chosen to implement their experimental setup using a lensless Fourier transform geometry as shown in Figure 5-1. We describe the effect of non-paraxial imaging conditions for this geometry. The reference beam for a lensless Fourier transform hologram consists of a diverging spherical wave located in the plane of the object. The unique properties of this

holographic case can be seen in the reconstruction process. After extracting the holographic field that contains the object term, the product $G(x,y) = F(x,y)R^{*}(x,y)$ is recovered in the detector plane, where $F(x,y)$ is the complex object field and $R^{*}(x,y)$ is the complex conjugate of the reference wave. In the paraxial regime, the field $F(x,y)$ in the detector plane is related to the object field $f(\xi,\eta)$ by a Fresnel propagation

$$\begin{aligned} F(x,y) &= \frac{e^{ikz}}{i\lambda z}\exp\left[\frac{ik}{2z}\left(x^2+y^2\right)\right]\int\int_{-\infty}^{\infty} f(\xi,\eta) \\ &\quad \times\exp\left[\frac{ik}{2z}\left(\xi^2+\eta^2\right)\right]\exp\left[\frac{-i2\pi}{\lambda z}(x\xi+y\eta)\right]dxdy \\ &= \frac{e^{ikz}}{i\lambda z}\exp\left[\frac{ik}{2z}\left(x^2+y^2\right)\right]FT\left\{f(\xi,\eta)\exp\left[\frac{ik}{2z}\left(\xi^2+\eta^2\right)\right]\right\} \end{aligned} \tag{7.2}$$

or, by rearranging this expression and taking an inverse Fourier transform of both sides,

$$\begin{aligned} f(\xi,\eta) &= i\lambda z e^{-ikz}\exp\left[\frac{-ik}{2z}\left(\xi^2+\eta^2\right)\right]\int\int_{-\infty}^{\infty} F(x,y) \\ &\quad \times\exp\left[\frac{-ik}{2z}\left(x^2+y^2\right)\right]\exp\left[\frac{i2\pi}{\lambda z}(x\xi+y\eta)\right]\left(\frac{dx}{\lambda z}\right)\left(\frac{dy}{\lambda z}\right) \\ &= i\lambda z e^{-ikz}\exp\left[\frac{-ik}{2z}\left(\xi^2+\eta^2\right)\right]FT^{-1}\left\{F(x,y)\exp\left[\frac{-ik}{2z}\left(x^2+y^2\right)\right]\right\}. \end{aligned} \tag{7.3}$$

When the spherical reference is located on the optical axis in the plane of the object, the reference takes on the paraxial form

$$R(x,y) = e^{ikz}\exp\left[\frac{ik}{2z}\left(x^2+y^2\right)\right]. \tag{7.4}$$

We can substitute $R(x,y)R^{*}(x,y)=1$ into Eq. (7.3) such that

$$\begin{aligned} f(\xi,\eta) &= i\lambda z e^{-ikz}\exp\left[\frac{-ik}{2z}\left(\xi^2+\eta^2\right)\right] \\ &\times FT^{-1}\left\{F(x,y)R(x,y)R^{*}(x,y)\exp\left[\frac{-ik}{2z}\left(x^2+y^2\right)\right]\right\} \end{aligned} \tag{7.5}$$

which simplifies to

$$\begin{aligned} f(\xi,\eta) &= i\lambda z\exp\left[\frac{-ik}{2z}\left(\xi^2+\eta^2\right)\right]FT^{-1}\left\{F(x,y)R^{*}(x,y)\right\} \\ &= i\lambda z\exp\left[\frac{-ik}{2z}\left(\xi^2+\eta^2\right)\right]FT^{-1}\left[G(x,y)\right] \end{aligned} \tag{7.6}$$

and

$$\begin{aligned} I(\xi,\eta) &= \left|f(\xi,\eta)\right|^2 = \left|FT^{-1}\left[F(x,y)R^{*}(x,y)\right]\right|^2 \\ &= (\lambda z)^2\left|FT^{-1}\left[G(x,y)\right]\right|^2. \end{aligned} \tag{7.7}$$

The extracted term in the detector plane, $G(x,y)$, is related to the object field by a Fourier transform and a phase factor, and the image intensity is proportional to the squared-magnitude of the Fourier transform of the extracted field.

7.2.2. Nonparaxial Propagation Integral

The unique condition of quadratic phase terms canceling in Eq. (7.5) due to a lensless Fourier Transform geometry no longer remains true if paraxial imaging conditions are no longer applicable. Instead, the non-paraxial relationship between the fields in an object plane and another arbitrary plane is given by the Rayleigh-Sommerfeld diffraction integral [3]

$$F(x,y)=\frac{1}{i\lambda}\iint f(\xi,\eta)\left(1-\frac{1}{ikr_{01}}\right)\frac{\exp(ikr_{01})}{r_{01}}\frac{z}{r_{01}}d\xi d\eta, \tag{7.8}$$

where $r_{01}=\left[z^2+(x-\xi)^2+(y-\eta)^2\right]^{1/2}$ and z/r_{01} is the obliquity factor. For a distance many wavelengths from the aperture, $kr_{01}\gg 1$ and we can approximate

$$F(x,y)=\frac{z}{i\lambda}\iint f(\xi,\eta)\frac{\exp(ikr_{01})}{r_{01}^2}d\xi d\eta. \tag{7.9}$$

A binomial expansion, given by $\sqrt{1+b}=1+\frac{1}{2}b-\frac{1}{8}b^2+...$, can be used to approximate the phase in the Rayleigh-Sommerfeld integral. The Fresnel approximation (truncating the expansion after the first two terms) holds true when the maximum phase change associated with the third term, $b^2/8$, is much less than 1 radian [3]:

$$1\text{ rad}\gg\frac{2\pi}{\lambda}\frac{b^2}{8}=\frac{\pi}{4\lambda z^3}\left[(\xi-x)^2+(\eta-y)^2\right]_{\max}^2=\frac{\pi}{16\lambda z^3}(w+D)^4, \tag{7.10}$$

where w is the width of the object and D is the width of the detector (the maximum condition occurs at the corners of the object and detector). As discussed in Goodman [3], while this requirement can often be ignored for the propagation of smooth wavefronts, it cannot be ignored for wavefronts having fine structure, which is the case for the speckled fields of interest here.

In order to model a more accurate representation of the Rayleigh-Sommerfeld integral for non-paraxial propagation, as is the case with gigapixel SADH, we

propose including the third terms from the binomial expansion in our propagation model. For this work, we have physically detected a field in the detector plane (x, y) and wish to digitally reconstruct an image in the image plane (ξ, η). Unlike the Fresnel paraxial propagation equation, the full Rayleigh-Sommerfeld integral is not easily invertible. However, we choose to approximate the Rayleigh-Sommerfeld integral using a higher-order bionomial expansion based on Eq. (7.5) as the starting expression such that a given field $F(x, y)$ can be numerically integrated to give the image field, $f(\xi, \eta)$:

$$f(\xi,\eta) = i\lambda z e^{-ikz} \exp\left[\frac{-ik}{2z}\left(\xi^2+\eta^2\right)\right]\int\int_{-\infty}^{\infty} F(x,y)\exp\left[\frac{-ik}{2z}\left(x^2+y^2\right)\right] \times\exp\left\{\frac{ik}{8z^3}\left[(x-\xi)^2+(y-\eta)^2\right]^2\right\}\exp\left[\frac{i2\pi}{\lambda z}(x\xi+y\eta)\right]\left(\frac{dx}{\lambda z}\right)\left(\frac{dy}{\lambda z}\right). \tag{7.11}$$

In the presence of non-paraxial imaging conditions, the use of the third term in the binomial expansion of r_{01} results in a space-variant phase term within the propagation kernel. For a small region of interest within the object plane centered at coordinates (ξ_0, η_0), we can estimate $f(\xi, \eta)$ using an inverse Fourier transform,

$$f(\xi,\eta) = i\lambda z \exp\left[\frac{-ik}{2z}\left(\xi^2+\eta^2\right)\right] \times FT^{-1}\left[F(x,y)\exp\left[\frac{-ik}{2z}\left(x^2+y^2\right)\right]\exp\left\{\frac{ik}{8z^3}\left[(x-\xi_0)^2+(y-\eta_0)^2\right]^2\right\}\right]. \tag{7.12}$$

7.2.3. Non-paraxial Spherical Reference

Ignoring the amplitude factor, the phase factor in the hologram plane of a spherical reference point originating from the coordinates (ξ_r, η_r, z_r) can be modeled as

$$R(x,y) = \exp\left[ikr(x,y)\right] = \exp\left[ik\sqrt{z_r^2 + (\xi_r - x)^2 + (\eta_r - y)^2}\right]. \tag{7.13}$$

Using the same third term in the binomial expansion as described above, we can expand the reference wavefront as

$$R(x,y) = \exp(ikz_r)\exp\left\{\frac{ik}{2z_r}\left[(\xi_r - x)^2 + (\eta_r - y)^2\right]\right\} \times \exp\left\{\frac{-ik}{8z_r^3}\left[(\xi_r - x)^2 + (\eta_r - y)^2\right]^2\right\}. \tag{7.14}$$

Using the same procedure to insert the identity $R(x,y)R^*(x,y) = 1$, we can describe the more complex relationship between the object and the extracted field in the hologram plane using Eq. (7.12),

$$\begin{aligned} f(\xi,\eta) = i\lambda z \exp\left[\frac{-ik}{2z}\left(\xi^2 + \eta^2\right)\right] \\ \times FT^{-1}\left[F(x,y)R^*(x,y)\right. \\ \times \exp\left\{\frac{ik}{2z_r}\left[(x-\xi_r)^2 + (y-\eta_r)^2\right]\right\}\exp\left[\frac{-ik}{2z}\left(x^2 + y^2\right)\right] \\ \left.\times \exp\left\{\frac{-ik}{8z_r^3}\left[(x-\xi_r)^2 + (y-\eta_r)^2\right]^2\right\}\exp\left\{\frac{ik}{8z^3}\left[(x-\xi_0)^2 + (y-\eta_0)^2\right]^2\right\}\right]. \end{aligned} \tag{7.15}$$

We see that the object term $F(x,y)R^*(x,y)$ is multiplied by two quadratic functions and a space-dependent phase term before the use of a Fourier transformation. If we

have an on-axis reference source at $(\xi_r, \eta_r, z_r) = (0, 0, z)$, which was true for the paraxial spherical reference in Eq. (7.4), we see cancellation of the quadratic terms, such that

$$\begin{aligned} f(\xi,\eta) &= i\lambda z \exp\left[\frac{-ik}{2z}\left(\xi^2+\eta^2\right)\right] \times FT^{-1}\left[F(x,y)R^*(x,y)\right. \\ &\qquad \left.\times \exp\left[\frac{-ik}{8z^3}\left(x^2+y^2\right)^2\right]\exp\left\{\frac{ik}{8z^3}\left[(x-\xi_0)^2+(y-\eta_0)^2\right]^2\right\}\right] \\ &= i\lambda z \exp\left[\frac{-ik}{2z}\left(\xi^2+\eta^2\right)\right] FT^{-1}\left[G(x,y)\right. \\ &\qquad \left.\times \exp\left[\frac{-ik}{8z^3}\left(x^2+y^2\right)^2\right]\exp\left\{\frac{ik}{8z^3}\left[(x-\xi_0)^2+(y-\eta_0)^2\right]^2\right\}\right]. \end{aligned} \tag{7.16}$$

However, if the axial position $(\xi_r, \eta_r, z_r) = (0, 0, z_r)$ of the on-axis reference source is not in the same plane as the object, then Eq. (7.15) becomes

$$\begin{aligned} f(\xi,\eta) &= i\lambda z \exp\left[\frac{-ik}{2z}\left(\xi^2+\eta^2\right)\right] \\ &\qquad \times FT^{-1}\left[F(x,y)R^*(x,y)\exp\left[\frac{ik}{2z_r}\left(x^2+y^2\right)\right]\exp\left[\frac{-ik}{2z}\left(x^2+y^2\right)\right]\right. \\ &\qquad \left.\times \exp\left[\frac{-ik}{8z_r^3}\left(x^2+y^2\right)^2\right]\exp\left\{\frac{ik}{8z^3}\left[(x-\xi_0)^2+(y-\eta_0)^2\right]^2\right\}\right] \end{aligned} \tag{7.17}$$

$$f(\xi,\eta) = i\lambda z \exp\left[\frac{-ik}{2z}\left(\xi^2+\eta^2\right)\right] FT^{-1}\left[F(x,y)R^*(x,y)\exp\left[\frac{ik}{2}\frac{z-z_r}{z_r z}\left(x^2+y^2\right)\right]\right.$$
$$\left.\times\exp\left[\frac{-ik}{8z_r^3}\left(x^2+y^2\right)^2\right]\exp\left\{\frac{ik}{8z^3}\left[\left(x-\xi_0\right)^2+\left(y-\eta_0\right)^2\right]^2\right\}\right]$$
$$= i\lambda z \exp\left[\frac{-ik}{2z}\left(\xi^2+\eta^2\right)\right] FT^{-1}\left[G(x,y)\exp\left[\frac{ik}{2}\frac{z-z_r}{z_r z}\left(x^2+y^2\right)\right]\right.$$
$$\left.\times\exp\left[\frac{-ik}{8z_r^3}\left(x^2+y^2\right)^2\right]\exp\left\{\frac{ik}{8z^3}\left[\left(x-\xi_0\right)^2+\left(y-\eta_0\right)^2\right]^2\right\}\right]. \tag{7.18}$$

The aberrations terms in Eq. (7.18) have the form of the usual Seidel aberrations (piston, defocus, spherical, astigmatism, coma and distortion). Expanding Eq. (7.18), the Seidel aberrations for the functional form of the phase errors can be represented as:

Piston: $$W_{200} = \frac{k}{8z^3}\left(\xi_0^4+\eta_0^4+2\eta_0^2\xi_0^2\right) \tag{7.19}$$

Defocus: $$W_{020} = \frac{k}{2}\frac{z-z_r}{z_r z}\left(x^2+y^2\right) \tag{7.20}$$

Coma: $$W_{131} = \frac{-k}{2z^3}\xi_0 x\left(x^2+y^2\right) - \frac{k}{2z^3}\eta_0 y\left(x^2+y^2\right) \tag{7.21}$$

Astigmatism: $$W_{222} = \frac{k}{2z^3}\xi_0^2 x^2 + \frac{k}{2z^3}\eta_0^2 y^2 + \frac{k}{z^3}\xi_0\eta_0 xy \tag{7.22}$$

Field Curvature: $$W_{220} = \frac{k}{4z^3}\xi_0^2\left(x^2+y^2\right) + \frac{k}{4z^3}\eta_0^2\left(x^2+y^2\right) \tag{7.23}$$

Distortion: $$W_{311} = \frac{-k}{2z^3}\xi_0^3 x - \frac{k}{2z^3}\eta_0^3 y. \tag{7.24}$$

When $z = z_r$, the spherical terms $\left(x^2 + y^2\right)^2$ cancel.

7.3. Aberrations due to Experimental Uncertainties

A space-dependent phase error has been introduced with the use of the binomial expansion for non-paraxial imaging. The use of a Fourier transform geometry, where a point source effectively canceled out the Fresnel kernel, resulted in a simplification of phase terms in the paraxial approximation that is no longer valid. In addition to the complex propagation integral described by Eq. (7.15), we now consider other sources of phase aberrations which may be the result of experimental uncertainties.

7.3.1. Position of Reference Source

Complications to this Fourier transform geometry result if the spherical point source is not located in the exact plane of the object, e.g., an on-axis reference source located at a different z-plane, $\left(\xi_r, \eta_r, z_r\right) = \left(0, 0, z_r\right)$ with $z_r \neq z$. As we see in Eq. (7.18), both terms in z^{-3} and z^{-1} are impacted if the reference is not located in the exact plane of the reference, however terms in z^{-1} are much larger than the terms in z^{-3} and hence are more important. Instead of the complex conjugate of the reference $R^*\left(x, y\right)$ canceling with the Fresnel kernel, one of the phase functions in z^{-1} takes the form of a quadratic chirp or defocus function

$$\exp\left[\frac{-ik}{2z_r}\left(x^2 + y^2\right)\right]\exp\left[\frac{ik}{2z}\left(x^2 + y^2\right)\right] = \exp\left[\frac{ik}{2}\frac{z_r - z}{z_r z}\left(x^2 + y^2\right)\right], \qquad (7.25)$$

where z_r is the distance from the reference source to the hologram plane. As Claus states in Ref. [8], this function will result in a very low frequency chirp (focus term) since z and z_r are approximately matched. For simplicity, we set

$$a = \frac{k}{2}\frac{z_r - z}{z_r z}. \tag{7.26}$$

Including this position mismatch into the propagation condition, Eq. (7.15) becomes

$$f(\xi,\eta) = i\lambda z FT^{-1}\left[G(x,y)\exp\left[ia\left(x^2+y^2\right)\right]\right. \\ \left.\times\exp\left[\frac{-ik}{8z_r^3}\left(x^2+y^2\right)^2\right]\exp\left\{\frac{ik}{8z^3}\left[\left(x-\xi_0\right)^2+\left(y-\eta_0\right)^2\right]^2\right\}\right]. \tag{7.27}$$

7.3.2. Coordinate System

To account for additional system ambiguities such as a hologram plane that is not centered on-axis to the object and reference (as was the case in our experimental conditions) and to take into account an appropriate lateral shift in the coordinate system, we further generalize the propagation condition to

$$f(\xi,\eta) = i\lambda z FT^{-1}\left[G(x,y)\exp\left\{ia\left[\left(x-b\right)^2+\left(y-c\right)^2\right]\right\}\right. \\ \left.\times\exp\left\{\frac{ik}{8z_r^3}\left[\left(x-b\right)^2+\left(y-c\right)^2\right]^2\right\}\exp\left\{\frac{-ik}{8z^3}\left[\left(x-b-\xi_0\right)^2+\left(y-c-\eta_0\right)^2\right]^2\right\}\right]. \tag{7.28}$$

This is a subtle, yet important addition to the propagation equation. Other previous work done with off-axis numerical propagation also recognized the need for a shifted coordinate system [12].

7.3.3. Additional Experimental Unknowns

Besides the phase errors already described, we believe that additional higher-order phase errors may be present in the experimental data. Sources of these aberrations may include errors from the mosaicking process as well as instability of the reference and object beam during the acquisition process (due to the long collection time). Although we do not have a direct analytical expression for these random errors, we can extend Eq. (7.28) to take into account these higher-order aberrations by describing the generalized field in the hologram plane as

$$f(\xi,\eta) = FT\left\{G(x,y)\exp\left\{ia\left[(x-b)^2+(y-c)^2\right]\right\}\exp\left[i\theta(x,y,\xi_0,\eta_0)\right]\right\} \quad (7.29)$$

where θ includes all the space-variant errors from the propagation integral, frame mosaicking and reference beam stability. In Eq. (7.29) we have grouped all the higher-order phase errors together – both the space-variant errors due to the non-paraxial nature of the propagation and the higher-order errors from experimental phase aberrations. This expression and the phase terms described here will become the basis of our aberration correction technique.

7.4. Aberration Correction using Sharpness Maximization for Non-paraxial Imaging

As we will describe in Section 7.4.1, one of the advantages of our approach to aberration correction is the ability to recover unknown higher-order aberrations using a generalized phase error model. This reduces requirements on the exact knowledge of system aberrations while at the same time allowing for fast image reconstruction

techniques. The model of the field upon propagation which we outlined in Section 7.2 describes the space-variant effects present in this generalized aberration approach and allows us to determine the size of the isoplanatic patch over which we can correct for these unknown aberrations, as we describe in Section 7.4.2.

7.4.1. Sharpness Maximization Approach to Phase Error Correction

We have identified both paraxial approximation propagation phase errors and experimental phase errors as sources of aberrations present upon propagating the field to the image plane. Regardless of the source of the error, we would like to be able to correct for these aberrations simultaneously with an efficient, post-detection correction technique. We have derived analytic expressions of how these various aberrations affect the relationship between the image and hologram planes. We will use these analytical expressions as a basis for forming appropriate optimization procedures to estimate phase errors present and thereby obtaining near-diffraction-limited image resolution.

Our method of phase-error correction is to utilize a sharpness maximization technique over regions of interest. An image sharpness metric, as defined by Muller and Buffington [13], has a lower value for images that are degraded by aberrations than that of the ideal image. Image sharpening algorithms have been shown to perform well both under coherent and incoherent imaging conditions [13-20]. Several sharpness metrics have been proposed [13] as well as additional "designer" sharpness metrics [17] based on the statistics of the image.

For this work, we use a standard sharpness metric,

$$S_1 = \sum_{\xi,\eta} I^{\beta}(\xi,\eta) \tag{7.30}$$

where $I(\xi,\eta)$ is the intensity of the image (the speckle-averaged image if one has multiple speckle realizations) and β is a scalar quantity. The use of an analytical gradient will allow for a highly efficient nonlinear optimization approach to estimating the phase errors using this sharpness maximization technique [17, 19, 20]. Eq. (7.29) contains four distinct quantities which we would like to optimize to sharpen the intensity in the image plane, namely, *a, b, c* and $\theta(x, y, \xi_0, \eta_0)$. The first three variables are scalar quantities, while $\theta(x, y, \xi_0, \eta_0)$ is a 2-dimensional, higher-order, space-dependent phase error.

This generalized approach to aberration correction for propagation-related phase errors allows us to estimate aberrations in the detector plane over an isoplanatic patch of the form

$$\varphi_{est}(x, y, \xi_0, \eta_0) = \exp\left\{ia\left[(x-b)^2 + (y-c)^2\right]\right\}\exp\left\{\frac{-ik}{8z_r^3}\left[(x-b)^2 + (y-c)^2\right]^2\right\} \times \exp\left\{\frac{ik}{8z^3}\left[(x-b-\xi_0)^2 + (y-c-\eta_0)^2\right]^2\right\}. \tag{7.31}$$

That estimated phase is multiplied by the extracted holographic image field in that plane, and then propagated to the image plane. By correcting for these phase aberrations in the detector plane, we are able to recover high-resolution images over an isoplanatic region.

7.4.2. Isoplanatic Phase Error Correction using a Region-of-Interest

As discussed in Section 7.2.1, the use of the binomial expansion of the spherical wave and the Rayleigh-Sommerfeld integral will introduce a space-variant phase error given by Eq. (7.11). In this analysis, we are strictly considering space-variant errors due to the propagation integral, not phase errors due to misregistration or other errors steaming from experimental conditions. Using the described sharpness maximization approach to phase correction, we wish to apply a higher-order, space-variant phase term of the form

$$\varphi_{SV}\left(x,y,\xi_0,\eta_0\right)=\exp\left[\frac{-ik}{8z_r^3}\left(x^2+y^2\right)^2\right]\exp\left\{\frac{ik}{8z^3}\left[\left(x-\xi_o\right)^2+\left(y-\eta_o\right)^2\right]^2\right\} \quad (7.32)$$

that will compensate for these phase errors over an isoplanatic patch (neglecting a shifted coordinate system for ease of explanation). In order to estimate the size of the isoplanatic region, we require that the maximum phase change between the phase error estimated by sharpness maximization and the actual phase error given in Eq. (7.32) is less than 1 radian. Therefore, we wish to determine the distance between two spatially separated points that maintains this criterion. Let the maximum width of the isoplanatic patch be *L* and the width of the detector be *D*. Figure 7-3 illustrates this isoplanatic geometry by way of path length differences between points for (a) an on-axis isoplanatic patch, and (b) an off-axis isoplanatic patch. We seek to derive the analytical expression that defines the size of the isoplanatic patch.

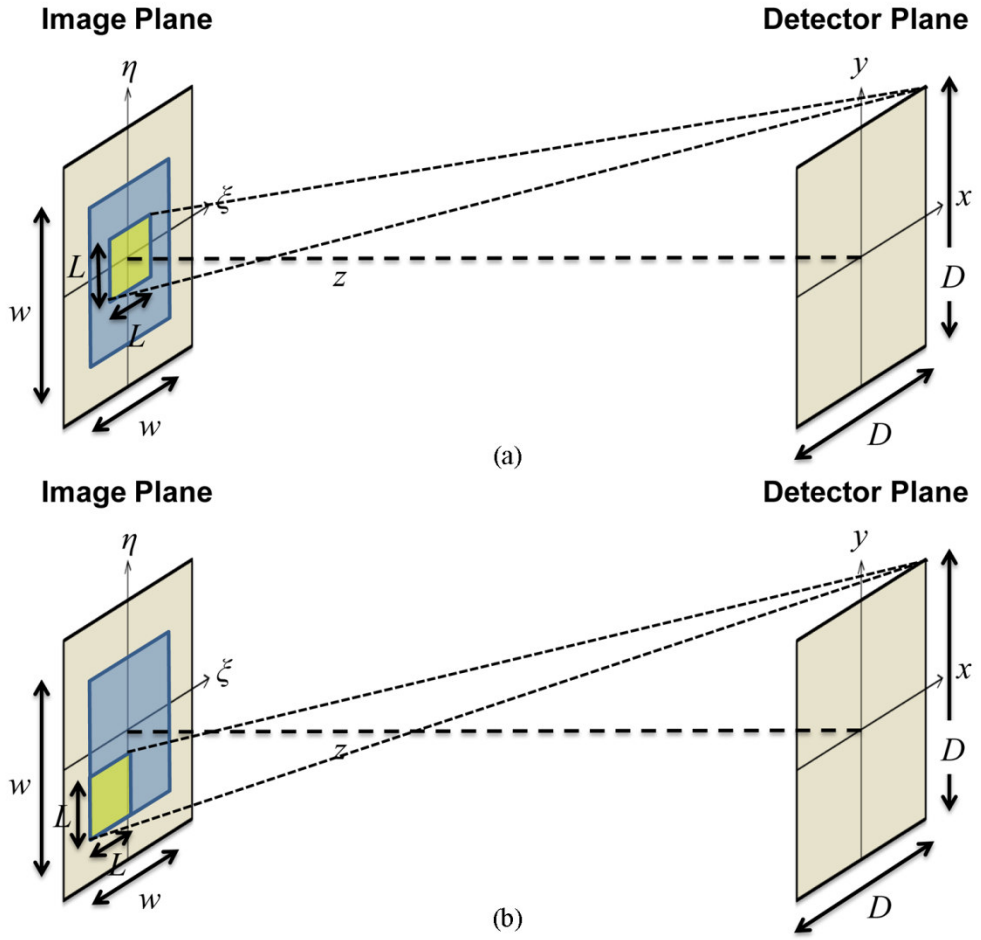

Figure 7-3. Yellow square represents an isoplanatic region of width *L* within the larger image (represented by a blue square of width *w*). The maximum path length differences between the isoplanatic region and the detector plane are illustrated by dashed lines for (a) an on-axis isoplanatic patch and (b) an off-axis patch.

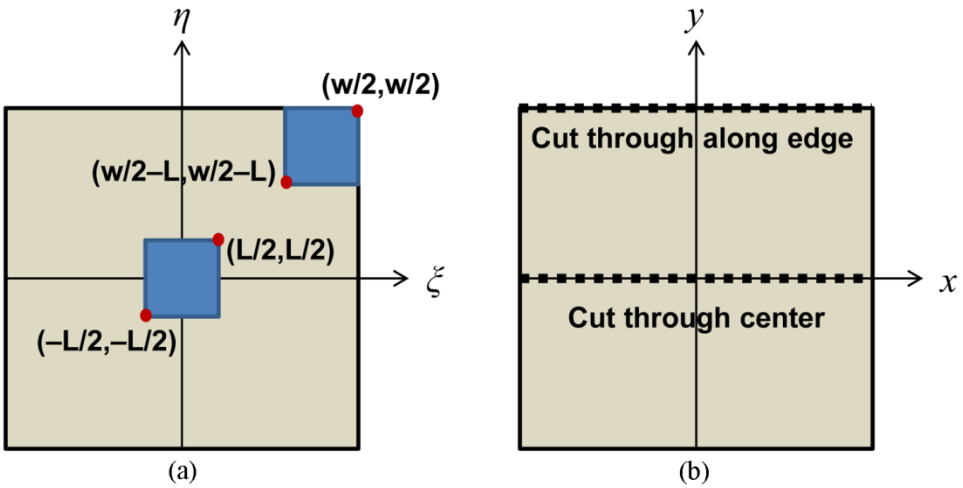

Figure 7-4. Diagrams describing the calculated isoplanatic patches. (a) Image plane with on-axis and off-axis isoplantic regions, (b) detector plane denoting phase cut-throughs shown in Figure 7-5.

Figure 7-4(a) depicts two different isoplanatic patches with width L in the image plane. We seek to measure the maximum phase difference which will be due to the path length difference between two diagonal corners, namely $(L/2, L/2)$ and $(-L/2, -L/2)$ for the on-axis isoplanatic patch and $(w/2, w/2)$ and $(w/2 - L, w/2 - L)$ for the off-axis isoplanatic patch. The corresponding phases will be measured in the detector plane. In Figure 7-5, we display cuts through the phase functions measured from $-D/2$ to $D/2$ at two different positions in the detector plane, one along the edge of the detector array, and the other through the center, as illustrated in Figure 7-4(b). We are interested in comparing the phase differences in the detector plane since this will determine the maximum isoplanatic patch size in the image plane.

For the on-axis isoplanatic patch, the quartic term of the phase has the form

$$\varphi_{L/2}(x,y)=\exp\left[\frac{-ik}{8z_r^3}\left(x^2+y^2\right)^2\right]\exp\left\{\frac{ik}{8z^3}\left[\left(x-\frac{L}{2}\right)^2+\left(y-\frac{L}{2}\right)^2\right]^2\right\} \quad (7.33)$$

for the upper right corner $(L/2, L/2)$ of the isoplanatic patch, while the lower left corner $(-L/2, -L/2)$ has the phase

$$\varphi_{-L/2}(x,y)=\exp\left[\frac{-ik}{8z_r^3}\left(x^2+y^2\right)^2\right]\exp\left[\frac{ik}{8z^3}\left\{\left[x-\left(-\frac{L}{2}\right)\right]^2+\left[y-\left(-\frac{L}{2}\right)\right]^2\right\}^2\right]. \quad (7.34)$$

Figure 7-5(a, b) shows horizontal cut throughs illustrating the difference between the $\varphi_{L/2}(x,y)$ and $\varphi_{-L/2}(x,y)$ phases for the on-axis isoplanatic region. The red line (– · –) denotes the phase from the $-L/2$ corner, the blue line (- - -) denotes the phase from the $L/2$ corner, and the black line (····) the average of $\varphi_{L/2}(x,y)$ and $\varphi_{-L/2}(x,y)$. The maximum phase change occurs at the edges and corners of the detector array, where the maximum phase change $\Delta\varphi_{\max}$ is defined by

$$1\,\text{rad} > \Delta\varphi_{\max} = \frac{1}{2}\left|\varphi_{L/2}(x,y)-\varphi_{-L/2}(x,y)\right|_{\max}. \quad (7.35)$$

For an array of 32,768 pixel and a pixel pitch of 7.4 μm, D = 24.2 cm. With an imaging distance of z = 3.31 m, z_r = 3.31 m and a wavelength of λ = 514 nm, the isoplanatic patch size for an on-axis patch is found to be L = 6.65 mm, or 899 pixels in order to satisfy the conditions of the central region. When determining the conditions of the central region, a cut through the center of the detector plane was

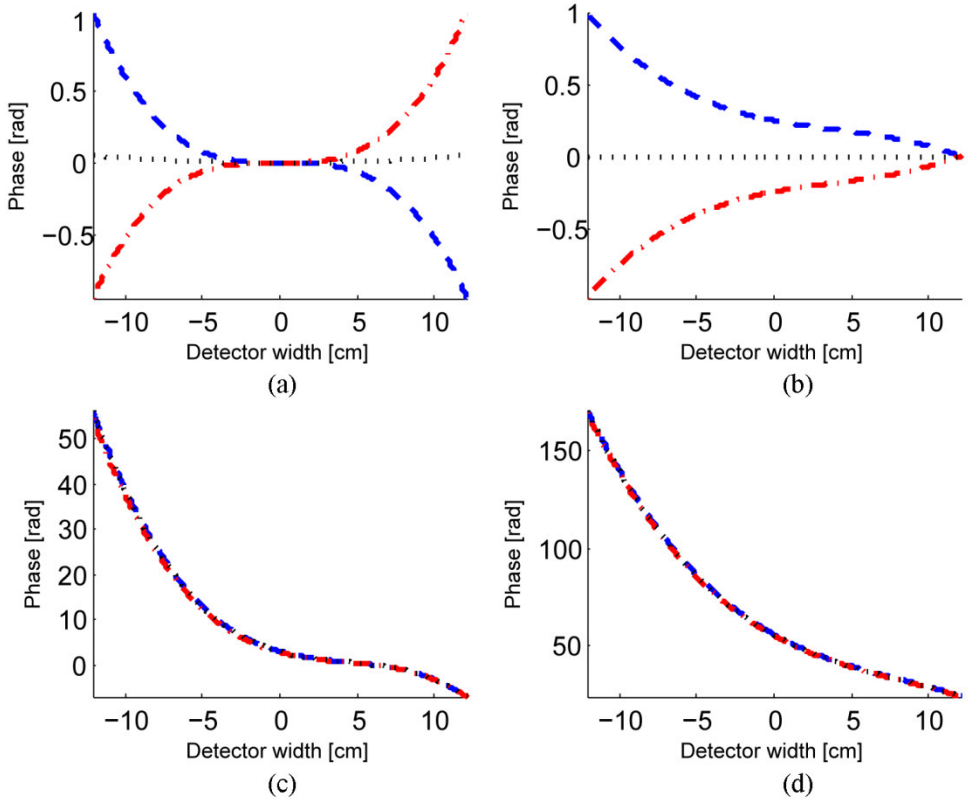

Figure 7-5. Plots show isoplanatic conditions when $\Delta\varphi_{\max} < 1$ rad. The red line (– · –) denotes the phase from the $-L/2$ corner, the blue line (- - -) denotes the phase from the $L/2$ corner, and the black line (····) the average of $\varphi_{L/2}(x,y)$ and $\varphi_{-L/2}(x,y)$. (a, b) Cut through phase error at two corners of the on-axis isoplanatic patch. (a) Phase through center when L = 6.65 mm and (b) phase along edge of array when L = 1.66 mm. (c, d) Cut through phase error at two corners for the off-axis isoplanatic patch. (c) Phase through center when L = 2.4 mm and (d) phase along edge of array when L = 0.45 mm.

used to determine the maximum phase change, as shown in Figure 7-4(b) and Figure 7-5(a), respectively. However, due to the quartic function of this phase error, the phase rapidly increases at the edges of the detector. For the most stringent corner-to-corner conditions, the isoplanatic patch size is reduced to L = 1.66 mm, or 224 pixels. A cut along the edge of the detector plane, as shown in Figure 7-4(b), necessitates a smaller isoplanatic patch in order to maintain a 1 radian maximum phase change, as

shown in Figure 7-5(b). Since the majority of the energy is located within an area within a circular diameter D, we believe that correcting over an isoplanatic patch size based on the edge-to-edge conditions encompasses the majority of the phase aberrations and is appropriate for the analysis and corresponding results presented in Section 7.5. Digitally windowing out a specific region-of-interest that is equal to or less than the isoplanatic patch size will mitigate against space-variant blurring effects.

We also consider the maximum off-axis isoplanatic patch, with the appropriate phase terms

$$\varphi_{w/2} = \exp\left[\frac{-ik}{8z_r^3}\left(x^2 + y^2\right)^2\right]\exp\left\{\frac{ik}{8z^3}\left[\left(x - \frac{w}{2}\right)^2 + \left(y - \frac{w}{2}\right)^2\right]^2\right\} \tag{7.36}$$

and

$$\varphi_{w/2-L} = \exp\left[\frac{-ik}{8z_r^3}\left(x^2 + y^2\right)^2\right]\exp\left[\frac{ik}{8z^3}\left\{\left[x - \left(\frac{w}{2} - L\right)\right]^2 + \left[y - \left(\frac{w}{2} - L\right)\right]^2\right\}^2\right]. \tag{7.37}$$

The phase difference for this off-axis condition is depicted in Figure 7-5(c, d) which shows its asymmetric nature, unlike the symmetric phase error that resulted in Figure 7-5(a, b). Considering a detector width of D = 24.2, cm, w = 13.2 cm, z = 3.31 m, z_r = 3.31 m, and λ = 514 nm, the isoplanatic patch size is found to be L = 2.4 mm or 324 pixels for the edge-to-edge condition and L = 0.45 mm or 61 pixels for the corner-to-corner condition. We see that the isoplanatic patch size decreases off-axis for both the edge-to-edge and corner-to-corner phase conditions.

The analysis here for the isoplanatic patch size is valid for a speckle-averaged image for which we can see bars at the diffraction limit. However, with single speckle realization images, as shown in this work, the speckle nature of the field reduces the resolution, effectively hiding aberrations. We will not notice the space-variant aberrations until they are much larger.

Region-of-interest imaging is particularly valuable for real-time applications. One could inspect the wide-field image at a coarse resolution to detect a region-of-interest, and then zoom in on a particular region of interest to reveal the finer details of that specific area. By applying a phase error correction over a specific region-of-interest, we are able to maximize the sharpness of the image in the viewing area that the user is interested in seeing within the larger image.

7.5. Experimental Procedure

7.5.1. Formation of Hologram

Holographic formation first begins by registering and mosaicking each individual frame accurately within the larger synthetic aperture. Each detected frame is the intensity of the interference between the object and reference fields. We start with the Fourier transform of the detected intensity which reveals the image, twin image and autocorrelation terms present from the holographic process. The image term is extracted using a flattop window with a raised-cosine edge (to minimize ringing artifacts) and shifted to the center of the array. An inverse Fourier transform is then applied to the array; this resultant term can be written as

$$G(x,y) = F(x,y)\,R^{*}(x,y) \tag{7.38}$$

where $F(x,y)$ is the complex field from the object in the detector plane and $R(x,y)$ is the reference field. By first extracting the complex object term, the high-order interference fringe is removed, but the object speckle field remains. We cross-correlate the overlapping portions of adjacent frames of this complex-valued field to determine their translations with sub-pixel accuracy and register each frame within the synthetic aperture [10].

From Eq. (7.29), we see that the field in the image plane (over an isoplanatic patch) can be described as a Fourier transform of the complex object field in the detector plane multiplied by several phase factors to account for the Fresnel kernel, non-paraxial conditions, misalignment and higher-order phase errors. As mentioned in Section 7.4.2, we are interested in limiting the region-of-interest of the image (ideally to an isoplanatic patch) to decrease the phase errors of non-paraxial imaging with Frensel/Fraunhofer propagators. To do so, we first Fourier transform the synthetic-aperture gigapixel array to the spatial frequency domain. One of the effects of the synthetic aperture was to increase the spatial frequency sampling rate compared to an individual array, since the frequency-domain sample spacing is

$$\Delta f = \frac{1}{N\Delta x} \tag{7.39}$$

for discrete arrays where N is the number of pixels and Δx is the detector pixel pitch.

In this work we are interested in not only reconstructing high-resolution

images, but also experimentally verifying the region-of-interest (ROI) isoplanatic patch size presented theoretically in Section 7.4.2. Therefore, we performed a series of reconstructions, varying the size of the selected region-of-interest. We examined ROIs with square dimensions of 450, 900, 1350 and 1800 pixels taken from the original gigapixel reconstructed image, shown in Figure 7-6. By looking at different sized ROIs, we sought to confirm the analytical isoplanatic patch size described in Section 7.4.2. We applied a mask to the gigapixel image using a flattop window with a raised-cosine edge of 23 pixels to the ROI before Fourier transforming arrays with these smaller sizes back to the spatial domain of the detector. This approach of selecting a ROI allows us to limit the field to the ROI while at the same time benefit from the finer spatial frequency sampling granted by the gigapixel synthetic aperture. A ROI approach also allows us to work with more manageable array sizes, concentrating our reconstruction to a specific area of the image for correction. We applied a phase correction to the complex field of the object in the detector plane to yield a corrected image upon Fourier transforming the field to the image plane. In the following section, we describe our method for phase correction using a sharpness metric.

7.5.2. Phase Error Estimation by Sharpness Maximization

We used a conjugate-gradient nonlinear optimization routine to maximize the sharpness of the image by estimating a phase in the detector plane described in Eq. (7.29). We took a two-step approach to the optimization of the phase aberrations

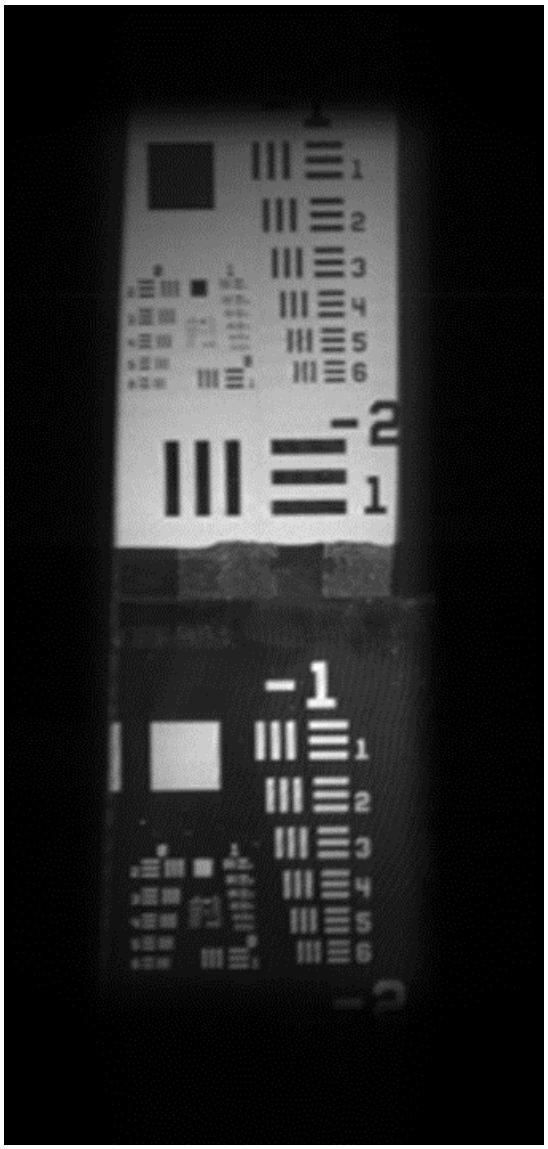

Figure 7-6. Two USAF bar targets reconstructed using the entire field-of-view (without phase-error correction).

present in this SADH experiment. First, the optimization employed analytic gradients of the sharpness metric with respect to the unknown variables *a*, *b*, and *c*, as described in Eq. (7.29). Second, we optimized for the space-variant errors in the system, holding the estimated quadratic phase correction (i.e. *a, b* and *c*) fixed. The method

of sieves was implemented, where the gradient of the point-by-point phase-error estimate was convolved with a Gaussian kernel. This convolution only permits smooth phase maps, helping to avoid stagnation at local minima. We start with a moderate-size Gaussian kernel and reduce the width of the Gaussian after a fixed number of iterations. Again, this allows us to first estimate lower-order phase errors and gradually introduce higher-order aberration estimates, thus avoiding stagnation problems, yet fully characterizing physically realizable higher-order phase errors [10].

7.6. Results and Analysis

7.6.1. Image Reconstruction Results

After estimating higher-order aberrations using image sharpening, we subtract the recovered phase errors from the phase of the field in the detector plane and propagate the corrected field to the image plane. Image reconstruction results for different sized ROIs are shown in Figure 7-7. Figure 7-7 (a – d) are the aberrated images before correction blurred by the non-paraxial propagation and other experimental errors, as described in Section 7.2. Note that the magnification of the different sub-figures changes based on the pixel count of the ROI. Figure 7-7 (e – h) show the improvement in the images after phase correction for the corresponding regions. We see a substantial improvement in the image quality across the entire field-of-view for all the ROIs.

To demonstrate the optical resolution improvement and quantitatively compare different ROIs, Figure 7-8 shows magnified Groups 4, 5 on the same scale

for these four images. The ROI of Figure 7-7 (c) was chosen to agree with the theoretical isoplanatic region-of-interest size based on the parameters of the experimental setup; Figure 7-7 (a) and Figure 7-7 (b) are larger than the theoretical isoplanatic region, while Figure 7-7 (d) is smaller than the theoretical isoplanatic patch. By visual assessment, we determined that the highest resolved vertical bar for

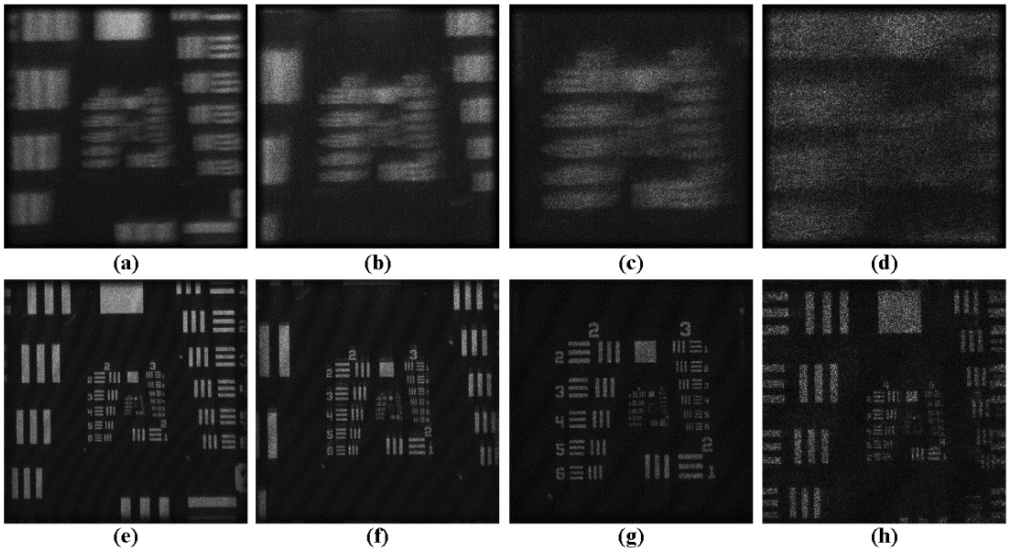

Figure 7-7. Region-of-interest image correction. (a – d) Regions before correction for different patch sizes and (e – h) same regions after applying phase correction; (a, e) 1800 pixels, (b, f) 1350 pixels, (c, g) 900 pixels, and (d, h) 450 pixels.

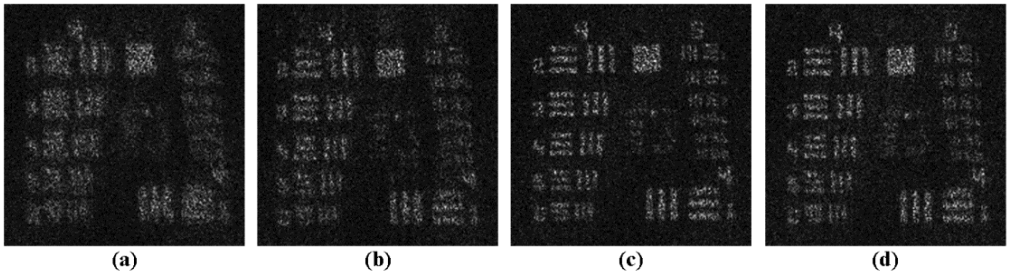

Figure 7-8. Comparison of groups 4, 5 for different patch size reconstructions, (a) 1800 pixels, (b) 1350 pixels, (c) 900 pixels, and (d) 450 pixels.
These are zoomed-in versions of Figure 7-7 (e–h).

each ROI was as follows: (4,2) for the ROI size 1800 pixels, (4,6) for the ROI size 1350 pixels, (5,2) for the ROI size 900 pixels and (5,2) for the ROI size 450 pixels. We can conclude that using a ROI size larger than the isoplanatic patch size degrades the image quality of the reconstruction since the sharpness maximization phase-error estimate cannot recover a phase estimate to model the anisoplanatic effects present. On the other hand, we see that a ROI smaller than the isoplanatic patch size did not result in an increase in image resolution, but instead limited the field-of-view of the image. These results confirm the isoplanatic patch size to be 900 pixels, as calculated in Section 7.4.2.

Additionally, we can compare our results with the theoretical resolution, based on the size of the aperture. The theoretical resolution (including a 3X reduction to account for the effect of speckle) is 22 μm both for horizontal and vertical bars due to a square synthetic aperture of 32,768 by 32,768 pixels. The theoretical finest resolvable bars correspond to (Group, Element) (5,4). Our experimental results show resolved bars for (5,2) which are in close agreement to the theoretical calculations.

A subtle effect to note with the ROI correction is the boundary edges of the reconstructed images. With the original field, we multiplied the data by a raised-cosine weighted mask at the edge of the ROI to provide a smooth roll-off. On the right edge in Figure 7-7(e), one can see the numbers of the bar target that came from the left side of Figure 7-7(a). One effect of the aberrated field is to bring in fields/light from outside the ROI; using an extra increase in array size, we can capture a slight increase in field-of-view beyond a selected ROI. However, Figure 7-7(h)

demonstrates the contrary example of poor edge-boundary reconstruction when the reconstructed array size is not large enough for this expanded field-of-view. Instead, on the right side of Figure 7-7(h), the edges of the image outside the original ROI is wrapped upon itself, causing poor edge reconstruction. These problems can be solved by ignoring pixels near the edge of the ROI and filling them in later with the results from an overlapping ROI for which those same pixels are not near the edge. The necessary size of mask weighting / zero-padding for the image reconstruction array is dependent on the strength of the aberrations in the system compared to the region-of-interest size.

7.7. Multiple Regions-of-Interest

We repeated our ROI image correction for different areas within the field-of-view of the object. Figure 7-9 shows the zoom-in of each region and its location within the larger image prior to phase correction. For our reconstruction technique, we maintained the same patch size (900 pixels) for each region, although as we discussed in Section 7.4.2, the effective isoplanatic patch size will be reduced off axis. Figure 7-10 shows those same regions after using the sharpness maximization approach to phase correction over an ROI. Each region is enhanced, correcting for aberrations present in Figure 7-9. From these results, we can conclude that it is possible to correct phase aberrations throughout the field-of-view for multiple areas. More research would need to be done to investigate the mosiacking of multiple corrected ROIs. However, it is possible to then mosaic together all phase-corrected regions to form a high-resolution gigapixel image for the entire field-of-view of the image.

7.8. Conclusion

In this work, we have corrected for phase aberrations in a synthetic-aperture digital holography experiment using a sharpness maximization technique. This method allowed for the use of Fresnel-like propagators in a non-paraxial imaging scenario by using estimates of higher-order phase errors over an isoplanatic region-of-interest. We derived a theoretical isoplanatic patch size to determine an appropriate region-of-interest size based on a binomial expansion of terms. Experimental tests confirmed that aberrations were best compensated with the use of a region-of-interest having a size no greater than the isoplanatic patch size. This computational imaging approach using sharpness metrics over a ROI estimates and corrects a variety of unknown phase aberrations in an intelligent manner based on a relevant numerical propagation and experimental phase errors.

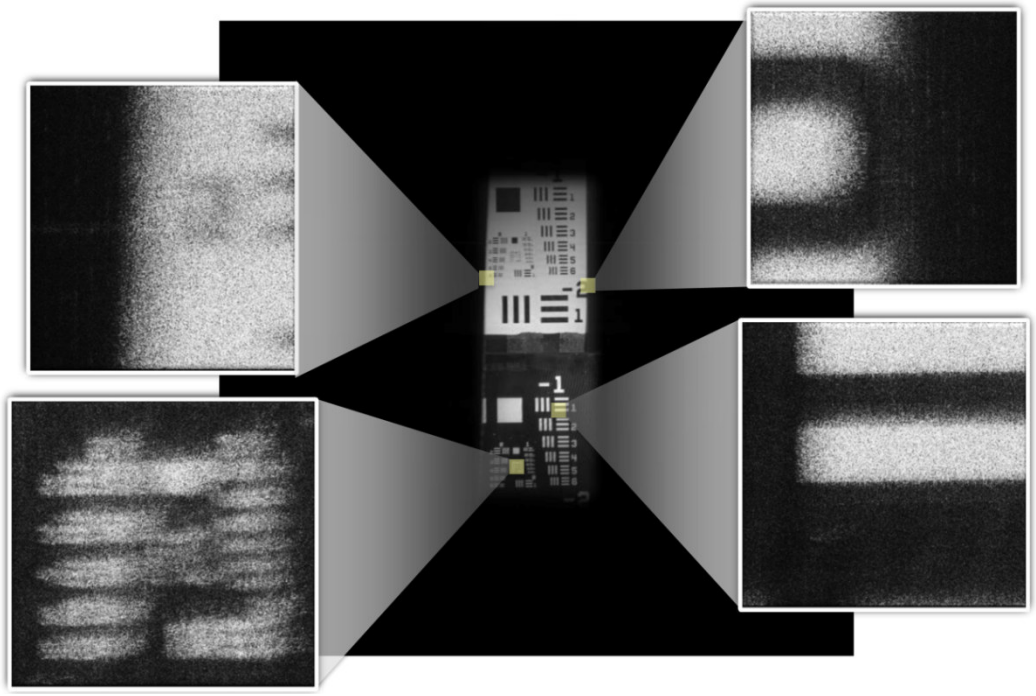

Figure 7-9. Full gigapixel image showing four regions-of-interest prior to phase correction.

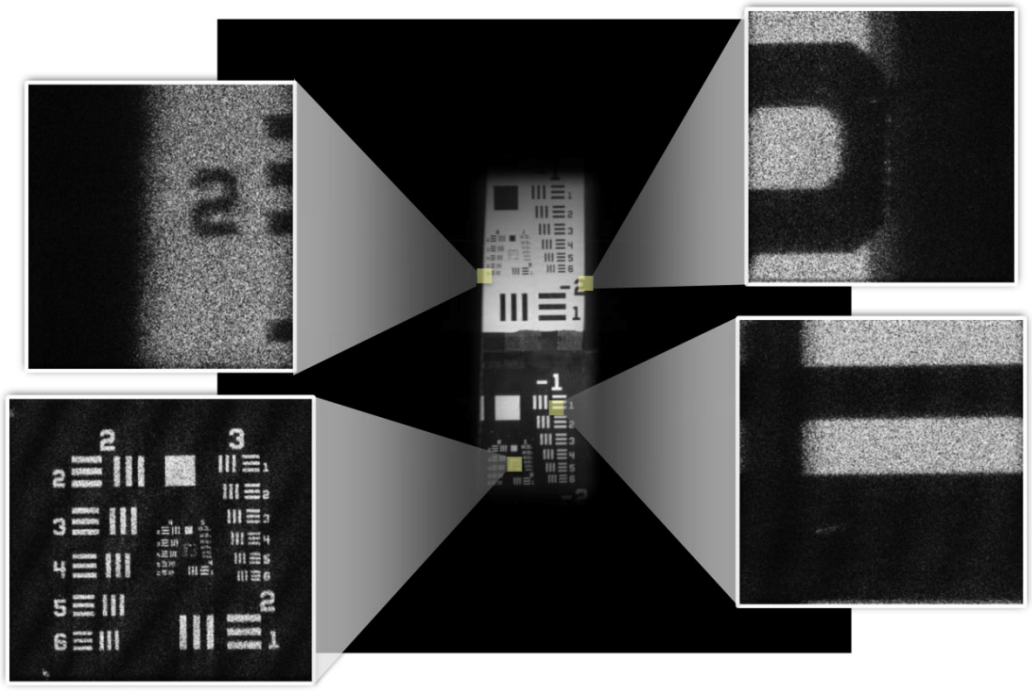

Figure 7-10. Full gigapixel image showing four regions-of-interest after using ROI in phase correction.

7.9. References

1. T.-C. Poon, *Digital holography and three-dimensional display : principles and applications,* (Springer, New York, 2006).

2. M. Sypek, "Light-propagation in the Fresnel region - new numerical approach," Opt. Comm. **116**, 43-48 (1995).

3. J. W. Goodman, *Fourier Optics,* 3rd Ed. (Roberts and Company, Englewood, CO, 2005).

4. F. B. Shen and A. B. Wang, "Fast-Fourier-transform based numerical integration method for the Rayleigh-Sommerfeld diffraction formula," Appl. Opt. **45**, 1102-1110 (2006).

5. J. A. C. Veerman, J. J. Rusch, and H. P. Urbach, "Calculation of the Rayleigh-Sommerfeld diffraction integral by exact integration of the fast oscillating factor," J. Opt. Soc. of Am. A **22**, 636-646 (2005).

6. J. H. Massig, "Digital off-axis holography with a synthetic aperture," Opt. Lett. **27**, 2179-2181 (2002).

7. J. L. Di, J. L. Zhao, H. Z. Jiang, P. Zhang, Q. Fan, and W. W. Sun, "High resolution digital holographic microscopy with a wide field of view based on a synthetic aperture technique and use of linear CCD scanning," Appl. Opt. **47**, 5654-5659 (2008).

8. D. Claus, "High resolution digital holographic synthetic aperture applied to deformation measurement and extended depth of field method," Appl. Opt. **49**, 3187-3198 (2010).

9. S. Lim, K. Choi, J. Hahn, D. L. Marks, and D. J. Brady, "Image-based registration for synthetic aperture holography," Opt. Express **19**, 11716-11731 (2011).

10. A. E. Tippie, A. Kumar, and J. R. Fienup, "High-resolution synthetic-aperture digital holography with digital phase and pupil correction," Opt. Express **19**, 12027-12038 (2011).

11. A. E. Tippie and J. R. Fienup, "Gigapixel synthetic-aperture digital holography: sampling and resolution considerations," in *Computational Optical Sensing and Imaging* OSA Technical Digest (CD) (Optical Society of America, 2011), paper CWB1.

12. K. Matsushima, "Shifted angular spectrum method for off-axis numerical propagation," Opt. Express **18**, 18453-18463 (2010).

13. R. A. Muller and A. Buffington, "Real-time correction of atmospherically degraded telescope images through image sharpening," J. Opt. Soc. Am. **64**, 1200-1210 (1974).

14. M. A. Vorontsov, G. W. Carhart, D. V. Pruidze, J. C. Ricklin, and D. G. Voelz, "Adaptive imaging system for phase-distorted extended source and multiple-distance objects," Appl. Opt. **36**, 3319-3328 (1997).

15. L. Nock, G. E. Trahey, and S. W. Smith, "Phase aberration correction in medical ultrasound using speckle brightness as a quality factor," J. Acoust. Soc. Am. **85**, 1819-1833 (1989).

16. T. J. Schulz, "Optimal sharpness function for SAR autofocus," IEEE Sig. Proc. Lett. **14**, 27-30 (2007).

17. J. R. Fienup and J. J. Miller, "Aberration correction by maximizing generalized sharpness metrics," J. Opt. Soc. Am. A **20**, 609-620 (2003).

18. K. D. Wulff, D. G. Cole, R. L. Clark, R. DiLeonardo, J. Leach, J. Cooper, G. Gibson, and M. J. Padgett, "Aberration correction in holographic optical tweezers," Opt. Express **14**, 4169-4174 (2006).

19. J. R. Fienup, "Synthetic-aperture radar autofocus by maximizing sharpness," Opt. Lett. **25**, 221-223 (2000).

20. S. T. Thurman and J. R. Fienup, "Phase-error correction in digital holography," J. Opt. Soc. Am. A **25**, 983-994 (2008).

8. Conclusion

8.1. Key Contributions and Accomplishments

The work presented in this thesis has a primary focus on aberration correction in digital holography. In addition, we have investigated issues of weak object signal digital holography, which is of general interest and can be applied to both application areas of our primary thrusts: imaging through multiple phase screens and synthetic-aperture digital holography. In this chapter, we summarize some of the key contributions and accomplishments of this thesis research which we believe to be significant and original.

We have confirmed through simulation and experiment the theoretical predictions that SNR depends solely on the compression gain and the object signal for the case of weak-signal digital holography. Single-shot, off-axis digital holography experiments (that did not require additional phase shifting techniques) were performed, demonstrating recognizable image reconstructions despite extremely low-light levels (small fraction of a photon per detector pixel).

By our work in digital holography through multiple phase screens simulating volume atmospheric turbulence, we have made several contributions to this field. First, we developed a modified sharpness metric which helps preserve the space-bandwidth product upon propagation to multiple planes and mitigates against telescopic oversharpening. This development was crucial to maintain correction magnification of the image by reconstructing accurate phase screen estimates in

multiple planes. Additionally, we derived non-trivial analytic gradients with respect to phases in intermediate planes for multi-plane nonlinear optimization. As a secondary issue, we developed an understanding that allowed us to avoid wrap-around aliasing for simulations with finite arrays. Using the modified sharpness metric and corresponding gradient calculations, we were able to achieve successful image reconstructions for two- and three-plane phase screens in simulation and for two-plane phase screens in experiment despite severe anisoplanatism (space-variant blurring). To our knowledge, this was the first time that multiple-plane phase correction was successfully performed for an extended object not having bright, isolated glints.

For our work in synthetic aperture digital holography (SADH), we explored two new approaches to image reconstruction. To our knowledge, we are the first in the digital holography community to use non-iterative modal reconstructors based on slope measurements between hologram sub-apertures for wavefront correction. This technique borrows principles originally used in the map-drift algorithm in synthetic-aperture radar and in extended-scene Shack-Hartmann wavefront sensing. We showed experimentally that this approach is most relevant to the correction of global, lower-order phase errors across a DH synthetic aperture.

For the correction of both low-order global phase errors and higher-order phase errors that occurred in SADH as a result of frame-by-frame mosaicking errors and experimental aberrations, we found that aberration correction using sharpness maximization to be highly successful. We have demonstrated diffraction-limited

resolution for a 12,000 by 18,000 synthetic aperture after phase correction. One effect we experienced for the large aperture resulting from SADH was non-paraxial imaging; we have shown both by mathematical analysis and experimentally that anisoplantic aberrations are present over the aperture. By correcting over a small region-of-interest in the image, we show that these anisoplanatic aberrations can be compensated. To our knowledge, we are the first to observe “ghost images”, the effect of image replication from wrap-around aliasing for undersampled data propagated using angular spectrum methods. We have developed techniques to use non-exact propagators, in combination with phase correction techniques over a limited field-of-view, for high-resolution imaging under non-paraxial conditions. We have mosaicked together and recovered images from the largest digital holographic aperture ever constructed, 32,786 x 32,786 pixels – one gigapixel!

These results – low light holography, multiple-phase screen reconstruction techniques, and high-resolution from large synthetic apertures – represent significant progress in the field of digital holography, particularly for applications in horizontal path imaging and long-distance imaging although they can be used for microscopic imaging as well.

8.2. Future Work

Although this thesis represents significant progress to the topics described above, this is a very rich area of research, with several possible areas open to further exploration. The future research topics described in this section are not extensive by

any means, but hopefully represent some of the more pressing questions that are currently unanswered as the result of the research presented in this thesis.

For low-light digital holography, further work can be performed to study compression gain and its direct relationship to image quality. For a given object signal detected in the hologram plane, the resulting SNR and hence image visibility will differ based on the object being imaged (i.e. point source-like objects vs. fully extended objects) as well as the SNR of the collected data. These imaging conditions will directly affect how weak the object signal can be, yet still recover a recognizable image in the presence of noise and speckle. Furthermore, we recommend constructing an outdoor digital holography experiment in a weak object signal regime to further extend the simulation and laboratory experiments presented in this thesis. Recovering weak object signals has applications in imaging long distances, through turbulent media, for diffuse scattering objects, or where the coherent laser power is limited. Further experimental verification of our results for each of these imaging scenarios would be valuable to researchers in those specific fields of study.

Our work with multiple-phase-screen digital holography lays important and foundational developments for imaging through extended horizontal path atmospheric turbulence. One of the future goals of this work would be to apply these algorithms and techniques to extended volume atmospheric turbulence correction. In order to make this a reality, we envision several intermediate research questions to address. First, our current nonlinear optimization only optimizes with respect to phase parameters. A next step would be to incorporate additional parameters into the

optimization, such as optimizing with respect to the phase screen position (which is currently a fixed, known parameter). Besides parameters with which we would like to estimate, we may also be able to include additional constraints, such as a support constraint for the object or prior knowledge of Kolmogorov statistics (C_n^2 and r_0), for the specific imaging scenario which may be valuable in the optimization process. Additionally, we may wish to extend this work to 3-D by imaging with not only one wavelength as described in this research, but imaging with multiple wavelengths.

Although our work strongly demonstrates the need of multiple phase screens for anisoplantic phase correction, further study should be done to look at the number and placement of the phase screens to most closely represent extended volume turbulence. Very likely, the number and placement of phase screens will be highly dependent on the specific imaging conditions, including the terrain conditions and how well the atmosphere can be represented as constant volume turbulence for the specific scenario under test. However, we suggest further study to understand the accuracy needed between the input model (exact phase screens) and the reconstructed, estimated phase screens. Depending on the placement of the screens, two screens located in close proximity may be modeled as a single phase screen, and the reconstructed phase estimates may "share" aberrations between the two screens. Furthermore, we recommend further study to explore the number of phase screen necessary to most accurately represent extended turbulence. Some work has been done in this area to by Paxman *et al.* [1] to simulate volume turbulence with phase screens, and this could be used as a starting point. For the reconstruction model, we

believe there may exist a trade-off between using additional phase screens to more closely represent extended turbulence, and a smaller parameter / less complex model. With the addition of more phase screens and the number of parameters included in the multi-dimensional problem, the complexity of the optimization increases and will result in substantial optimization runtime and possible stagnation before reaching the solution.

Prior to our construction of our intermediate 200-megapixel synthetic aperture and subsequent gigapixel synthetic aperture, previous authors had reported work for SADH that was several megapixels in size [2-6]. The increase in aperture size makes the work very demanding and the need to use appropriate mosaicking, propagation and aberration correction techniques increasingly important. Although we have used cross-correlation techniques to mosaic adjacent frames together within the larger aperture and correcting for relative piston offsets between these adjacent frames, improved and alternative methods to mosaicking and piston phase correction may be possible. We recommend optimizing the translations and piston phases by jointly optimizing all adjacent frames by minimizing the sum of the mean-square error between all available relative phases. With respect to wide-angle propagation techniques, we have only barely scratched the surface with regards to appropriate models; a more in-depth analysis of wide-angle sampling conditions is suggested. Also, for our approach to nonparaxial image reconstruction described in Chapter 7, we recommend optimization to include the object plane coordinates of the ROI to explicitly include the ξ_0, η_0 dependence analytically. The literature on wide-field

propagation methods topic spans several fields, but we believe that a more extensive survey of wide-angle propagation techniques coming from the optical microscopy community may hold promise to this work in SADH. The use of various non-paraxial propagators in combination with aberration correction techniques will be valuable to both scientific communities.

8.3. References

1. R. G. Paxman, B. J. Thelen, and J. J. Miller, "Optimal simulation of volume turbulence with phase screens," Proc. SPIE **3763**, (1999).

2. F. Le Clerc, M. Gross, and L. Collot, "Synthetic-aperture experiment in the visible with on-axis digital heterodyne holography," Opt. Lett. **26**, 1550-1552 (2001).

3. R. Binet, J. Colineau, and J. C. Lehureau, "Short-range synthetic aperture imaging at 633 nm by digital holography," Appl. Opt. **41**, 4775-4782 (2002).

4. J. H. Massig, "Digital off-axis holography with a synthetic aperture," Opt. Lett. **27**, 2179-2181 (2002).

5. J. L. Di, J. L. Zhao, H. Z. Jiang, P. Zhang, Q. Fan, and W. W. Sun, "High resolution digital holographic microscopy with a wide field of view based on a synthetic aperture technique and use of linear CCD scanning," Appl. Opt. **47**, 5654-5659 (2008).

6. D. Claus, "High resolution digital holographic synthetic aperture applied to deformation measurement and extended depth of field method," Appl. Opt. **49**, 3187-3198 (2010).